

Locally Tunable InAs Nanowire Quantum Dots for Cooper Pair Splitting

Inauguraldissertation

zur
Erlangung der Würde eines Doktors der Philosophie
vorgelegt der
Philosophisch-Naturwissenschaftlichen Fakultät
der Universität Basel

von

Samuel André d'Hollosy
aus Val d'Illiez VS



Basel, 2014

Genehmigt von der Philosophisch-Naturwissenschaftlichen Fakultät
auf Antrag von
Prof. Dr. C. Schönenberger
Prof. Dr. V. Pellegrini
Dr. R. Leturcq

Basel, 16.9.2014

Prof. Dr. Jörg Schibler
Dekan

Preface and Acknowledgement

Contents

Preface and Acknowledgement	iii
1. Introduction	1
2. Indium Arsenide Nanowires	3
2.1. Versatility of Nanowires	3
2.2. Growth & Crystal Structure	3
2.3. Electron conduction	6
2.4. Metallic Contacts to InAs	8
2.5. Properties	10
3. Theoretical background	13
3.1. Quantum Dots	13
3.1.1. Coulomb blockade and single electron tunneling	14
3.1.2. Coulomb peak line shape	16
3.1.3. Coulomb Diamonds	17
3.1.4. Quantum Dot States in Magnetic Field	18
3.2. Kondo Correlations in Quantum Dots	19
3.3. Superconductivity	22
3.3.1. Cooper Pairs	22
3.3.2. The BCS ground state	24
3.3.3. Andreev Reflection	26
3.4. Cooper pair splitter devices	29
3.4.1. Crossed Andreev Reflection	29
3.4.2. Cooper pair splitter with quantum dots	29
4. Fabrication and Measurement Techniques	35
4.1. Fabrication Overview	35
4.2. Basic e-beam lithography	37
4.3. Bottom gate fabrication	39
4.4. Nanowire placement	40
4.5. Experimental Setup	42
5. Tunnel Barrier Formation in InAs Nanowire Quantum Dots	45
5.0.1. Quantum Dots induced by global gates	46
5.0.2. Etched Nanowire Quantum Dots	48
5.0.3. Bottom gate induced quantum dots	55

5.1. Summary	60
6. g-factor Anisotropy in InAs Nanowires	61
6.1. g -factor Anisotropy	61
6.2. Anomalies of Kondo effect in magnetic field	65
6.3. Summary	66
7. Tunable Cooper Pair Splitters	67
7.1. Sample fabrication and characterization	67
7.2. Tuning of a drain tunnel barrier	69
7.3. Tuning of a source tunnel barrier	72
7.4. Tuning of the inter-dot coupling	73
7.5. Simple model	74
7.6. Summary	77
8. High-Bias Cooper Pair splitting	81
8.1. Device and Measurement Set-up	81
8.2. Non-local signals at large bias voltages	84
8.3. Gate and Bias dependence of the non-local signals	85
8.4. Discussion	87
8.5. Summary	88
9. Summary and Outlook	91
Bibliography	93
A. Fabrication recipes	103
A.1. Wafer characteristics	103
A.2. Wafer cleaning	103
A.3. EBL process for PMMA	103
A.4. EBL process for bottom gates	103
A.5. O ₂ plasma cleaning	104
A.6. Reactive ion etching (RIE) of SiN _x	104
A.7. Argon ion beam milling	104
B. Electrostatic discharges	105
C. Appendix to chapter 7	107
C.1. Gate voltages to form the QDs	107
D. Additional data to chapter 8	109
D.1. Gate characterization and doping effects	109
Curriculum Vitae	111
Publications	113

1. Introduction

Quantum mechanics is probably one of the most successful theories in physics because it keeps predicting measurement results and material properties with surprising precision until today [1]. Quantum mechanics (QM) is also disturbing as it questions everyday commonsense notions of a physical reality where objects always have a defined state and qualities by introducing e.g. the concepts of quantum superposition or wave-particle duality. Probably the most bizarre aspect of quantum mechanics was presented by famous Albert Einstein together with his co-workers Boris Podolsky and Nathan Rosen in 1935 and is now commonly known as EPR paradox [2]. They considered two identical particles in a special quantum superposition state. According to the Copenhagen interpretation of QM the wave function describing the two particles collapses upon measurement of a property of one particle, thus determining the same property of the second particle instantaneously no matter how far apart they are. However, the measurement outcome is still random but follows a statistical distribution given by the mathematical framework of QM. The publication of the EPR paper gave rise to quite some commotion in the community [3] and soon the term entanglement was coined to describe two particles.

In 1964 John S. Bell took the EPR paradox one step further formulating an inequality out of correlation between measurements outcomes. If inequality is violated in the experiment it rules out the whole class of local hidden variable theories which could generate an apparent entanglement [4]. It took nearly another 20 years until Alain Aspect and co-workers violated the inequality in an experiment with polarized photons and left little doubt on the validity of entanglement. Throughout the years other Bell-test experiments followed for example with massive Beryllium ions [5] and in a solid state system with superconducting phase qubits [6]. Quantum entanglement has even found its way to potential applications in quantum cryptography [7], quantum teleportation [8] and quantum computing [9] where entanglement is the key ingredient that speeds up quantum algorithms over classical ones.

The electron spin is the promising candidate to represent quantum information as a qubit in a quantum computer [10]. An implementation into a solid state system would make the qubits scalable comparable to the classical transistors. On demand generation of spin entangled electrons is therefore highly desirable. A possible route is to extract electron pairs from a superconductor [11] where the pairwise entanglement naturally occurs in form of Cooper pairs. In influential work, Recher *et al.* proposed to use two quantum dots to enhance the extraction process of the Cooper pairs. Quantum dots are man-made artificial atoms that can only take up or release one electron at the time. The beauty of these 'atoms' is that they can be tuned by electrical gate voltages and connected to electrodes. Once the electrons are extracted

to the quantum dots, they can be investigated with the spin manipulation toolkit [12] or put into a stream of entangled electrons that could be probed with ferromagnetic contacts [13, 14, 15]. The tunability of the quantum dots helps to boost the efficiency to the high values needed for the detection of the entanglement.

Unfortunately, it is not easy to connect quantum dots and superconductors together. Nevertheless, fabrication succeeded with InAs nanowires and carbon nanotubes and current correlation in two different leads of such Cooper pair splitting devices have been shown [16, 17, 18]. Even though high efficiency were achieved [19] the devices have been largely lacking the usual control and tunability of sophisticated quantum dot systems. Hence, this thesis aimed predominantly at integrating advanced local gate structures that have already been used to control QDs in two-dimensional electron gases [20], nanowires [21] and carbon nanotubes [22] or for the detection of Majorana Fermions [23] into Cooper pair splitting devices. At the same time we hoped for a better understanding of the involved transport processes in such devices.

The thesis is organized the following way. The second and the third chapter introduce some background and physical concepts related to the later experiments. In particular chapter 2 presents the used material system, InAs nanowires, more closely and review some its important properties. Chapter 3 discusses the more general concepts of QDs connected to normal and superconducting leads. In chapter 4 details on the device fabrication are given and the measurement set-ups are introduced. The fifth chapter discusses to the different approaches to make tunable quantum dots in InAs nanowires and contains first results of the thesis. The main results are then presented in chapters 6, 7 and 8 which are structured in way that they can be read independently. We investigate the g -factor in the InAs nanowire QD and map its anisotropy in chapter 6. The control and tunability of the g value is key concept of quantum computation and possibly useful for entanglement detection [81]. The next two chapter are dedicated to Cooper Pair Splitting devices and present ways to improve the splitting efficiency by using the tunable QDs from chapter 5. The results in chapter 8 are preliminary but provide indications that the efficiency could indeed be improved in InAs nanowire systems to values above 95% and needed for the detection of entanglement.

[g-factor?]

2. Indium Arsenide Nanowires

At the nanometer scale novel or modified material properties come into play because the particle size starts to be similar to the wave length. It opens up opportunities for new physics or modified device functionality. This is also the case for the investigated InAs nanowires with a diameter below 100 nm. In this chapter the material indium arsenide (InAs) is discussed with its bulk and mesoscopic properties and advantages for nanoelectronic devices.

2.1. Versatility of Nanowires

Nanowires are single crystalline highly anisotropic whiskers. They can be made of metallic, semiconducting or insulating material. The properties of the nanowires can be largely controlled to a large degree in their synthesis (see sec. 2.2). Apart from being interesting building blocks for quantum electronic devices, nanowires have gained much attention in various other fields. A standard review of nanowires is given by Lieber *et al.* [24] or more recently by Hyun *et al.* [25]. Starting out as platform for sensors [26] because of their high surface to volume ratio, nanowires were integrated in optical applications like solar cells [27], LEDs [28], photo detectors [29] and even nano lasers [30]. They were also proposed as building blocks for novel computer architecture, e.g. as high mobility field effect transistors (FETs) [31] or wrapgate FETs [32].

The InAs nanowire system presents us a few advantages compared to traditional lithography defined mesoscopic devices. The main advantage is the nearly free choice of contact material which is rather limited in the 2-dimensional electron gas (2DEG) systems. The reason lies in the low-ohmic contact formation due to special band structure and surface states of InAs as discussed in more detail in sections 2.3 and 2.4. In particular, direct electrical contact to ferromagnetic and superconducting materials are possible which allows to observe novel physical effects from the interaction with these materials. In addition, the nanowires can be transferred from the growth substrate to substrate best suitable for device fabrication. Since the electronic properties are linked to the crystal structure and geometry, they can be engineered during the growth process as discussed in more the detail in the next section.

2.2. Growth & Crystal Structure

Already in the 1960ies the growth of InAs nanowires was reported [33]. The growth mechanism was discussed intensely, and concluded to be of the vapour-liquid-solid

(VLS) type. In this process, atomic or metal-organic precursors from the gas phase accumulate inside a metallic catalyst particle, usually made of gold. When the precursor concentration in the gold gets supersaturated growth of a nanopillar starts with the catalyst staying at the top of the pillar (see fig. 2.1a). Different methods for catalyst deposition on the substrate exist. Particles are either deposited from a colloidal suspension or by aerosol techniques or they are formed directly on the substrate by metal evaporation and subsequent thermal annealing. These techniques all lead to random distribution of the nanowires on the substrate. Ordered arrays can be obtained by patterning the substrate, e.g. by lithography. Growth of all common group IV, III-V, and II-VI semiconductors was demonstrated [34]

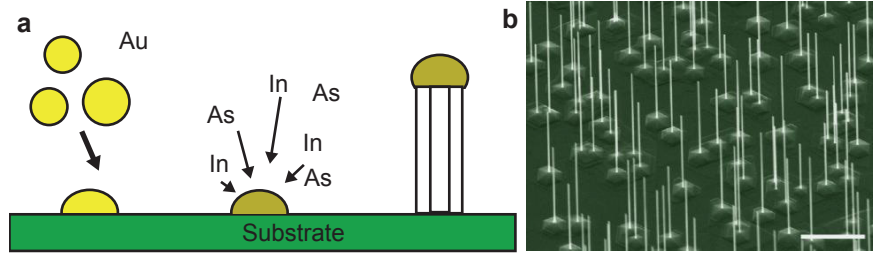


Figure 2.1.: **a** - Illustration of the vapor-liquid-solid (VLS) growth mechanism for nanowires. Gold catalyst particles are spread to a substrate. Precursor in the gas phase incorporate into the catalyst particle and crystallize below the particle giving rise to nanowire growth. **b** - FE-SEM image of InAs nanowires grown by the VLS technique on InAs(111)B substrate. The scale bar is $2\ \mu\text{m}$. Credit: UC San Diego

Feeding the semiconductor to the catalyst particle can be achieved by various methods. Nanowire growth has been shown using laser ablation, chemical vapour deposition (CVD), metal-organic vapour phase epitaxy (MOVPE), chemical beam epitaxy (CBE) and molecular beam epitaxy (MBE). The group of Jesper Nygård¹ employed the latter method for the synthesis of nanowires and kindly provided them to our group. The advantage of the MBE method is the minimization of carbon incorporation into the nanowires compared to methods with metal-organic precursor like MOVPE or CBE. In MBE the semiconductor constituents are sublimated from the elements and, together with a ultra high vacuum (UHV), most pure chemical compounds can be grown. The growth temperature which is 400°C . More details on the growth method can be found in references [35, 36]. We will turn the discussion to the size and crystal structure of the InAs nanowires and the linked electronic properties.

Control over the diameter is given by catalyst particle size which can be adjusted by the chosen deposition method. The length of the nanowire is primarily determined by the growth time, which can be substantial using the MBE method and wanting lengths of a few micrometers. Controlling the growth direction and the crystal structure is more difficult. The bulk crystal structure of InAs is zb , however the hexagonal wurzite crystal structure (wz) is observed in InAs nanowires under the right growth conditions.

¹Nils Bohr Institute, University of Copenhagen.

InAs nanowires in the zinc blende (*zb*) crystal structure will preferentially grow in the $\langle 111 \rangle$ direction with a hexagonal cross-section.

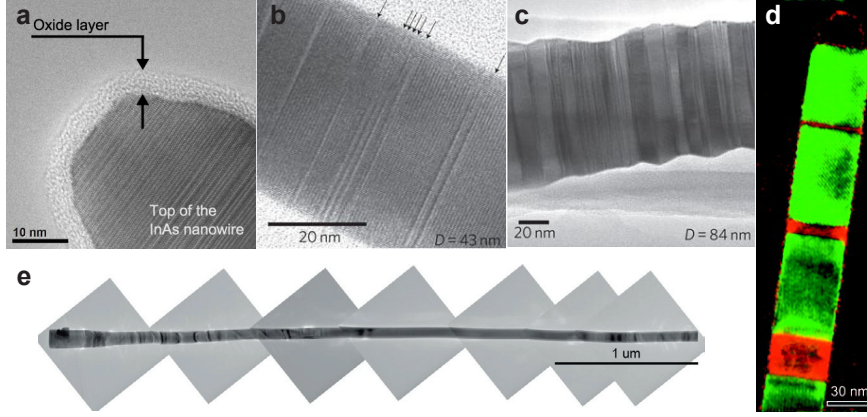
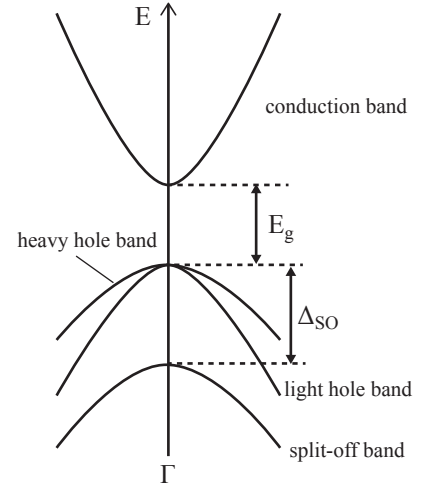


Figure 2.2.: **a** | Surface oxide on a InAs nanowire (NW) in a transmission electron microscopy (TEM) image [37]. **b** | TEM image of a nanowire with low lattice defect density. The arrows mark stacking faults in the *wz* crystal structure [38]. **c** | Nanowire with mixed *zb/wz* crystal structure [38]. **d** | Example of an axial heterostructure. The red colored areas are InP sections in the InAs NW [39]. **e** | Multiple TEM images of a typical nanowire used in the thesis. No stacking faults are found in the central part of it. Black regions can stem from strain.

Fig. 2.2b shows a transmission electron micrograph of smaller diameter nanowire (40nm) in the *wz* structure with planar lattice defects known as stacking faults. Different types of these can occur in both crystal phases and are nicely summarized in reference [40]. In the extreme case polytypic wires are observed with both crystal phases present. (fig. 2.2c). It was found that in these polytypic nanowires the electron mobility is largely reduced due bandgap mismatch (see sec. 2.5), however stacking faults do not have significant influence on the mobility[41]. A diameter dependence of the crystal phase is found [38, 42]. Thin wires grow preferentially in the *wz* phase, while thick ones grow in the *zb* phase. The nanowires used in this work are of the pure *wz* type. A combination of multiple transmission electron microscope (TEM) images of one is shown in fig. 2.2e. The wires are grown as thin pillar in the *wz* phase with an additional radial overgrowth making them slightly tapered. The diameters are in the range of 60 nm to 90 nm. The TEM investigation (fig. 2.2e) by our collaborators show that the central part of the nanowire is defect free and that stacking faults mainly occur at the ends of the nanowire. An important point for device fabrication is that the amorphous oxide ($\lesssim 5$ nm) forms as soon as the nanowires are exposed to air which makes a surface treatment necessary to achieve electrical contacts (see fig. 2.2a).

Other reasons for the generally low mobilities in InAs are sometimes discussed, in particular inhomogeneities during growth like the incorporation of Au from the catalyst particle or C from the metal organic precursors. While the latter can be

Figure 2.3.: Bandsructure sketch around the Γ -point of InAs, with E_g being the band gap, Δ_{SO} the energy of the spin-orbit split-off band below the conduction band edge.



minimised by the use of MBE as mentioned, the former is circumvented by using a self catalysed process was introduced recently [43, 44].

Finally, it is worth mentioning that nanowire heterostructures were realized early on. In nanowires new material combinations can be realized, forbidden in bulk systems, because the strain due to lattice mismatch can relax to the surface. If precursor material is varied during the nanowire growth an axial heterostructure is obtained. An example is shown in fig. 2.2d, where InP (coloured red) is switched with InAs (coloured green) [39]. Most commonly, another semiconductor is radially overgrown (core-shell nanowires) [45, 46]. This is an important development for quantum devices since most of the electron density is largest at the surface as discussed next.

2.3. Electron conduction

Regarding electron conduction in InAs nanowires we not only have to discuss the crystal arrangement as in the previous section but as well the electronic band structure. InAs is a III-V semiconductor with quite considerable covalent bonding character between the indium and the arsenic atoms. It not so obviously follows that InAs has small direct band gap at the Γ -point. Since electron transport happens only near the Fermi energy. Only consider the band structure around the Γ -point as depicted in fig. 2.3. As we will, see only the conduction is important which is parabolic to good approximation parabolic with an effective electron mass of $m^* = 0.023m_e$ and m_e being the mass of the free electron. Due to the 2-dimensional confinement in radial direction the electron states are quantized normal to the wire axis x forming so called transverse modes. We assume that the bulk energy dispersion relation stays parabolic around the Γ -point in the nanowire and find the subband dispersion

$$E_n(k_x) = E_n + \frac{\hbar^2 k_x^2}{2m^*} \quad (2.1)$$

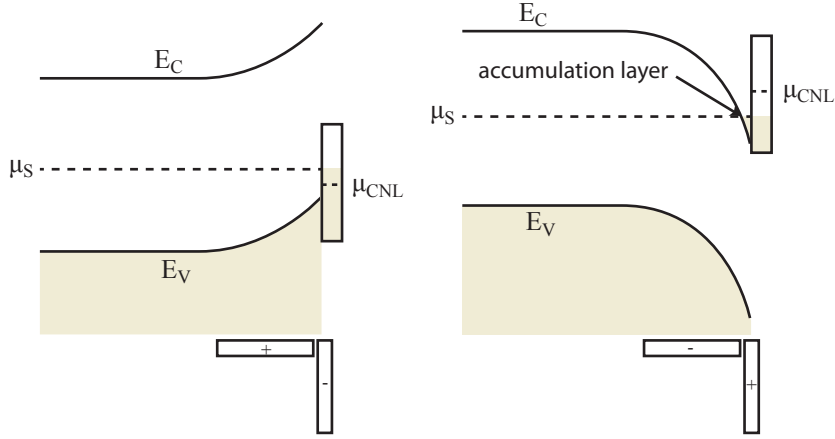


Figure 2.4.: **a** | Band edges of typical semiconductors like GaAs as function of space. The bands are bent upwards in energy towards the surface (right side) due to acceptor-like surface states forming a negative surface charge depicted below the band diagram. **b** | The same diagram as in (a) but for case of InAs. Donor-like surface states create a downward band bending leading to an electron accumulation layer below the surface.

where E_n denotes the energy minimum of the subband due to mode quantization. Calculation of the current through such a channel connected to reservoirs leads to the remarkable result that the current I only depends on the number of occupied modes N

$$I = \frac{2e^2}{h} N V_{sd} \quad (2.2)$$

at zero temperature [47]. By either varying the bias voltage V_{sd} or the electron density via a gate voltage quantized conductance steps arise whenever a new subband becomes occupied. Indications of steps were observed in early measurements [48] while only lately clear conductance quantization in InAs NWs could be confirmed [49, 50]. The simple model has a few assumptions necessary to observe conductance quantization. Obviously, the temperature should be smaller than the subband spacing which is determined mainly by the nanowire diameter. Eq. 2.2 requires also that the transport is ballistic over the length of the wire. If scattering is present the conductance is reduced by a factor T denoted as transmission. It is believed that the surface scattering is the main cause for the reduced transmission in InAs nanowires. Surface passivation [51] has been shown to reduce interface traps and the surface scattering.

The discussion about the surface scattering in InAs nanowires becomes even more important when the surface chemistry of InAs is considered. At the boundary of a crystal some atoms are without a partner. These dangling bonds can sometimes mutually saturate each other reducing thereby reducing the energy (surface recon-

struction). These surface states can overlap and form surface bands with a Fermi level which we denote here as charge neutrality level μ_{CNL} . Its value is generally not the same as the bulk Fermi level μ_B . The two electrochemical potentials align by exchanging between bulk and surface giving rise to an electrical surface dipole. The direction of the charge flow is determined by the properties of the surface states which can either be donor- or acceptor-like. In the case of acceptor-like surface states, a negative surface charge builds up leading to upward band bending in the bulk (fig. 2.4a). The resulting depletion region can span several Fermi wavelengths due the small density of states in the bulk. In contrast the density of states of the surface band is large and the chemical potential changes only very little. This situation is often called Fermi level pinning by the surface states.

Usually, one finds the acceptor like picture in textbooks as it is the case for GaAs and other semiconductors. In contrast the case of InAs is quite unique as the surface states are donor-like and the bands bend to lower energies at the surface (fig. 2.4b). Electrons accumulate in a layer beneath the surface. The energy at which the Fermi level is pinned above the conduction band minimum E_C is between 130 meV and 300 meV [52] and depends on the surface orientation and on the chemical composition. For sulphur passivated surfaces it can be as large as 600 meV [53]. With these energies the depth of the surface accumulation layer can be estimated. Estévez Hernández and coworkers [54] found the maximum electron density 8 nm below the surface but extending up to 50 nm into the crystal in the case of InAs nanowires. The size of the accumulation layer is of the order of the Fermi wavelength. Therefore quantization effects and the formation of a surface 2DEG is expected which has been confirmed by STM investigation [55]. We conclude that the electron transport in the nanowires takes place mainly at surface in particular for the nanowires with a diameter of 60 nm or more used throughout the experiments in this thesis.

2.4. Metallic Contacts to InAs

Two different kinds of metallic contacts to a semiconductor can be distinguished. In Schottky barriers the current flow is hindered by an induced tunnel barrier while ohmic contacts behave resistive according to Ohm's law. In a simple picture the tunnel barrier height is given by the Schottky-Mott rule $\Phi_S = \Phi_m - \chi_e$ where Φ_m is the metal work function and χ_e is the electron affinity of the semiconductor, i.e. the energy difference of the bottom of the conduction band E_C and the vacuum level. Negative barrier heights result for some of the low work function metals like Al ($\Phi_{Al} \approx 4.28$ eV) or Ti ($\Phi_{Ti} = 4.33$ eV) [56], because the electron affinity of InAs is relatively large with a value of $\chi_e^{InAs} \approx 4.9$ eV [57]. On the other hand, noble metals with large work function like Au ($\Phi_m^{Au} = 5.1$ eV) should induce a barrier. This is clearly not the case. Measuring the barrier height with a voltage bias at the junction, gives only a weak dependence on the metallic material for most semiconductors. Moreover InAs, is found to make ohmic contact to basically any metal. One can argue that the work function is only a theoretical quantity, which depends on surface orientation and

recombination, but it is better to consider the metal-semiconductor interface more closely.

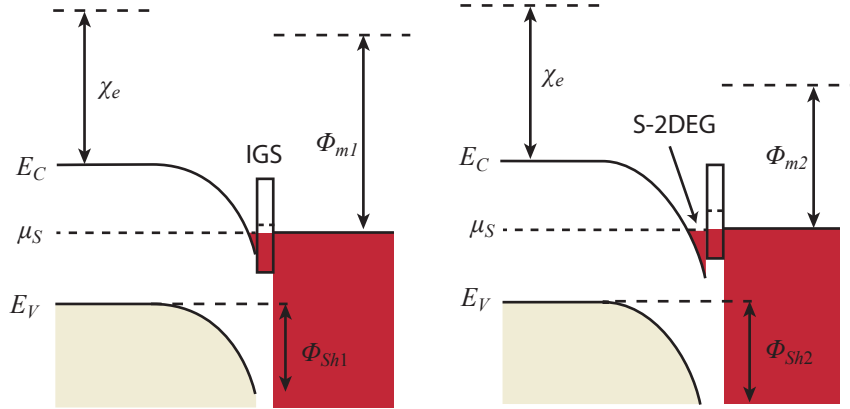


Figure 2.5.: **a** | Band edges of InAs when brought into contact with a noble metal with $\Phi_m > \chi_e$. Due to the similar quality of the induced gap states (IGS) to surface states, the bands are bent downwards in the InAs and an electron accumulation layer forms. **b** | Same diagram as in **a** for a metal with a lower work function than the electron affinity. Differences of the IGS can lead to a increased band bending.

When a metal is brought into contact with a semiconductor the local lattice structure at the interface is changed forming induced gap states (IGS). They arise because the wave function matching induces them usually inside the band gap of the semiconductor. The density of states of the metal remains basically unchanged and the IGS are found in the first atomic layers of the semiconductor. As in the free surface case, the Fermi levels of the bulk semiconductor μ_S , the IGS μ_{CNL} and of the metal μ_m will align as charges flow across the interface. The IGS have usually similar quality as the surface states, thus are donor-like in InAs. Their density of states is large enough to equilibrate the Fermi energies of metal and semiconductor without a big energy shift. Only in the semiconductor the bands are bent downwards and the charges accumulate in the conduction band. As long as the quality of the IGS states does not change by the different metals, the band bending will be similar and ohmic contacts are formed with low work function metals (fig. 2.5b) as well as with noble metals (fig. 2.5a). For example, Bhargava *et al.* find that the Fermi level is pinned at $E_{pin} = 130$ meV above the conduction band edge for Au on InAs [58].

So far we only discussed electron but not hole transport. The simple reason that only n-type behaviour in the nanowires is observed in spite of, that the p-type regime is in principle reachable by tuning the Fermi level into the valence band with the help of capacitively coupled electrodes, i.e. the gate voltages needed are still smaller than the breakdown field of the insulator. Hole conduction was to our knowledge never observed in InAs nanowires. Fig. 2.5 shows that for holes at the valence band edge E_V a considerable tunnel barrier to the metal $\phi_{Sh} = E_{pin} + E_g/2$ forms at the interface.

The barrier can only be overcome by large bias voltages. These two experimental conditions, large bias and p-type regime are rarely met at the same time.

Effects of different interface properties could be observed by Sourribes and coworkers [37]. They investigated two different surface treatment for removal of the native oxide for contact fabrication and found that the Ar plasma bombardment gives lower ohmic contacts compared to the wide spread sulphur passivation technique (see chapter 4 for details). However, this result is surprising as the band bending for sulphur terminated surfaces is known to be increased [53] which should lead to lower resistance contacts.

2.5. Properties

This section summarizes material properties of InAs and InAs nanowires.

Bandgap As most III-V semiconductors, bulk InAs crystallizes in the zinc-blende (*zb*) crystal structure. Measurements as well as calculations give a small direct bandgap of size $E_g = 0.36$ eV at 300 K. The zero temperature value is only accessible by calculation ($E_g = 0.42$ eV) [59, 60]. The *wz* crystal phase has been only observed in nanowires so far and much less is known about this phase. Whereas some photoluminescence measurements on *wz* nanowires find no significant difference [61] to the bulk *zb* gap, Möller et al. [62] could reproduce the theoretical predictions [63, 64, 65]. Thus, the bandgap of the wurzite crystal structure is generally believed to be 55 meV larger than the *zb* bandgap. Further increase is expected from quantum confinement effects. .

Fermi wavelength The effects are already visible in nanowires with diameter smaller than 60 nm [61]. This scale is also in agreement with the estimated Fermi wavelength between 15 nm and 33 nm [66]. It is obtained via the electron density. Different studies either counted the electrons in a SET device [67] or estimated the gate capacitance [66]. Recently, Hall measurements could be performed on InAs nanowires yielding 4 times lower densities [68, 69]. The discrepancy is attributed to the large density of surface states, which trap the major part of the charge induced by a gate voltage and is not probed in the Hall measurements.

Mobility Because of the small effective mass $m^* = 0.023m_e$, the electron mobility is expected to be large and bulk values of up to $40'000 \text{ cm}^2/(\text{Vs})$ were found [70]. However much smaller values are obtained for InAs nanowires ranging from $200 \text{ cm}^2/(\text{Vs})$ to $6600 \text{ cm}^2/(\text{Vs})$ [31]. The extracted mobilities are field effect mobilities where the gate capacitance which has to be estimated independently as well. Simulation in finite element Poisson solvers are considered to be quite accurate, however, charge traps of surface states cannot easily be included.

A dependence of the mobility on clear wire diameter is found [71, 72]. The small mobility in small diameter nanowires can be explained by surface scattering. The effective scattering potential should then be correlated to the surface

roughness recently confirmed in a AFM study [73]. Another effect reducing the mobility can stem from the polytypism in InAs nanowires. Band bending of the at the wz to zb interfaces can induce barriers of several meV [41]. Hence, mobility can be enhanced by reducing polytypism, e.g by incorporation of Sb [40] or by growth pure crystal phase wires [41]. The surface scattering is well reduced by radial shell growth. Latest core-shell InAs nanowires exhibit mobilities up to $15'000 \text{ cm}^2/(\text{Vs})$ [45, 74].

Mean free path The elastic mean free path can be obtained from the mobility and the Fermi wavelength in the Drude formalism. Values are in the range of 10 nm to 100 nm.

Phase coherence length The electronic phase coherence is usually extracted from universal conductance fluctuation (UCF) measurements. Upon lowering the temperature the root-mean-square (rms) amplitude saturates for a given device length. At the saturation the phase coherence length becomes larger than the channel length and thus can be determined by varying the channel length. The reported values of $l_\phi \approx 300 \text{ nm}$ agree quite well [75, 76, 54].

Spin-orbit interaction The spin-orbit interaction (SOI) in bulk InAs is quite large due to high nuclear charge of the involved elements. The main manifestation in the band structure is the spin-orbit split-off band which is lowered by $\Delta_{SO} = 0.38 \text{ eV}$ from the conduction band edge. Further, the inversion symmetry is broken in InAs which leads in principle to a Dresselhaus contribution to the SOI. However, the Dresselhaus coupling strength β_D is much smaller than the Rashba coupling α_R .

Landé g-factor The spin-orbit interaction also affects the energy splitting in a external field B . The g-factor is renormalized from the free electron value $g = 2$ to an effective value $g^* = -14.9$ [70] in InAs. It depends inversively on the energy gap E_g and the split-off band energy Δ_{SO} [47]

Spin relaxation length Spin relaxation in InAs nanowires is usually assumed to occur via the Elliot-Yafet mechanism [75]. The corresponding spin-orbit length l_{SO} can be extracted in weak anti-localization measurements [75, 77, 54]. Other works extract l_{SO} from Pauli spin blockade measurements [78] or by direct measurement of the spin-orbit interaction energy [79]. The different studies all report on the order of $l_{SO} \approx 200 \text{ nm}$ which is surprisingly small. When spin-orbit interaction is the only mechanism to relax the spin, large fields across the wires are needed. As seen in section 2.3, the surface dipole could provide such large fields. We use average electric field value of $E = 7.3 \cdot 10^6 \text{ Vm}^{-1}$ from Estévez Hernández *et al.* and Rashba spin-orbit coupling constant of $\alpha_0 = 117 \text{ Å}$ in the 1D equation [75]

$$l_{SO,R} = \frac{\hbar^2}{m^* e E \alpha_0} \quad (2.3)$$

to estimate the value of $l_{SO,R} = 388 \text{ nm}$ which is of the order of the measured values.

The spin-orbit interaction is an important property of InAs nanowires, e.g. it is required for the formation of Majorana bound states [23, 80] and for to possible detection of entanglement [81]. We emphasize again that most of the physics treated throughout the thesis is happening at the surface of the InAs nanowire. Therefore electron conduction is very susceptible to surface roughness and defects.

3. Theoretical background

Quantum dots are basic building blocks quantum electronics. In this chapter an introduction to their basic physics is given.

3.1. Quantum Dots

A quantum dot (QD) is a small volume of matter in which quantum mechanics allows only certain standing wave solutions for the electron wave function. Therefore, a quantum dot will possess discrete energy levels, similar to atoms and molecules, hence the term artificial atoms is also used. QDs were realized in various material systems including two-dimensional electron gases (2DEGs) in semiconductor heterostructures (lateral and vertical geometries), carbon nanotubes (CNTs), metallic particles, self-assembled semiconductor islands and nanowires. A common property shared among QDs is the charging energy e^2/C . Due to the small size and the related small capacitance of the island adding an electron requires a considerable amount of energy. The discrete energy levels of a QD have a characteristic shell-filling and level spacing δE that depend on the material and the geometry of the small volume of matter. The great advantage of QDs over single atoms is that they can be rather easily connected to electrodes and their properties can be investigated by electron transport spectroscopy. The electrodes, also referred to as leads or contacts, can consist of different normal metals or semiconductors yet even superconductors or ferromagnets. The latter we call *exotic* as well as all other materials with different electron correlation and spin ordering rendering their interaction with quantum dots particularly interesting. Vice versa such bulk correlations are interesting to investigate with a highly tunable single electron system. The electron wave function of a QD adopts the properties of the *exotic* lead as electrons are exchanged through the tunnel barrier. The hybridization strength is determined by the strength of the tunnel barrier between the lead material and the QD. Hence, by tuning the tunnel barrier we can change the properties of the quantum dot. When the barrier is low, the wavefunction of QD and the lead will overlap more and the electrons in the QD will correlate similar to the 'exotic' lead.

Different material systems have different advantages for the investigation of these *exotic* couplings. For example, the tunnel barrier can be well tuned and controlled in a lateral 2DEG. However, in these systems, the tunnelling is usually to the surrounding 2DEG what can hardly be replaced into an exotic. In contrast, quantum dots formed in CNTs or nanowires are readily connected to superconducting and ferromagnetic materials, but the barrier is more difficult to control. This thesis is focused on the InAs nanowires. Finding ways to achieve tunable tunnel barriers was one of the

primary goal of the thesis. Thus, this chapter is organised as follows. In a first part quantum dots shall be introduced along with the tools to estimate the coupling parameter, i.e. the tunnel barrier strength to the leads. The second part is then devoted to the specific ways of tunnel barrier formation in InAs nanowires.

In the ideal QD, the electron wave function is confined in all three spatial direction which is why QDs are also called zero-dimensional (0D) objects. The wave function amplitude depends on the exact confinement potential but also on the number of electrons on the QD. Because of the small size of the island the electron-electron interaction cannot be neglected or treated perturbatively. The Coulomb interaction becomes even the dominant energy scale when temperature and the coupling strength is small. Only a single electron at the time will be able to tunnel on and off the island. The following section treats the basics of this single electron tunneling transport.

3.1.1. Coulomb blockade and single electron tunneling

The effects of Coulomb interactions in QD are usually treated within the constant interaction model (CIM) [82, 83]. The model makes two major assumptions. First, it assumes that the energy spectrum of the quantum dot is independent of the charge state, i.e. the number of electrons on the dot. Second it assigns a single total capacitance C to the island also independent of the charge state. Despite this conceptual simplicity, the CIM describes the physics quite well for quantum dots with larger electron numbers $N \gtrsim 20$. The total capacitance's C major contribution are due to the source, drain and gate electrodes, but C also contains also capacitances from further gates or surrounding dielectrics: $C = C_S + C_D + C_G + C_R$. The capacitor model is schematically depicted in fig. 3.1.

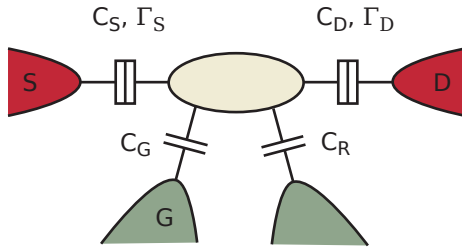


Figure 3.1.: Capacitor model of a quantum dot. Different electrodes surrounding the QD have different capacitances. In contrast to the gate (G), source (S) and drain (D) leads are modelled by an additional a tunnel coupling $\Gamma_{S/D}$ in parallel to C_S and C_D .

The total internal energy of a quantum dot with N electrons can be written as

$$U(N) = \frac{Q_{tot}^2}{2C} + \sum_{n=1}^N E_n, \quad (3.1)$$

with $Q_{tot} = -|e|(N - N_0) + \sum_i C_i V_i$ being the total charge on the QD. The first term in eq. 3.1 is the electrostatic energy, N_0 is the number of electrons when the quantum dot uncharged, i.e. all gate voltages are zero. The second term sums up the quantum mechanical level energies E_n often called orbital energy of the n -th

electron in analogy to the atomic orbital. The electrochemical potential is defined as $\mu_n = U(N) - U(N-1)$, i.e. energy for adding the N th electron to the dot and calculates to

$$\mu_N = E_N + \frac{e^2}{C} \left(N - N_0 - \frac{1}{2} \right) - \frac{|e|}{C} \sum_i C_i V_i. \quad (3.2)$$

Evaluating all chemical potentials for the electrons on the dot describes a 'ladder' as drawn in fig. 3.2 which can be moved up and down in energy by a gate voltage V_i . The difference between the chemical potentials does not change by doing so and

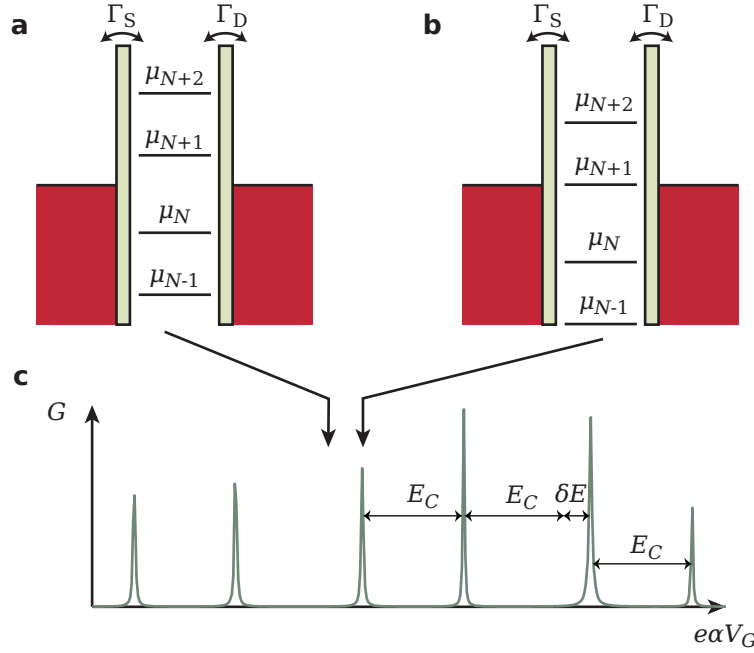


Figure 3.2.: **a** | Energy diagram with the electrochemical potentials of the QD (μ_{N-1} to μ_{N+2}) and of the source (μ_S) and the drain (μ_D) lead. The pale bars stand for potential barriers characterized by the tunnel rates $\Gamma_{S/D}$. μ_N and μ_{N+1} are away from $\mu_{S/D}$, thus the electron number is fixed and transport is not possible. **b** | μ_{N+1} is aligned to $\mu_{S/D}$ by a gate potential. Single electrons can tunnel on and off the QD making transport possible. **c** | Exemplary conductance G as function of a gate voltage in units of energy (eaV_G).

depends on the level energy E_n and the charging energy $E_C = e^2/C$. In the situation in fig. 3.2a, the μ_N is below the electrochemical potential μ_S and μ_D of the metal leads, respectively. The electron cannot tunnel out of the dot because all the states in the leads are filled up to the Fermi energy. Similarly, electrons in the leads have not enough energy to excite the μ_{N+1} level. This situation is called *Coulomb blockade* and the electron number on the QD is fixed. The electrochemical potentials (ladder) can be moved in energy by a gate voltage V_i by amount $ea\Delta V_i$ according to the gate's lever arm $\alpha = C_i/C$. In fig. 3.2b the μ_{N+1} level is aligned with the lead's electrochemical potentials $\mu_{N+1} = \mu_S = \mu_D$. If there is a small thermal broadening

in the leads, there will be electrons with enough energy to fill quantum dot as well as empty states to take up an electron from the QD. Thus, the QD will fluctuate between the N -electron ground states $U(N)$ and $U(N + 1)$.

If a small bias voltage $V_{SD} = V_S - V_D$ is applied to the source, the electric field across the QD will direct the charge fluctuations into a measurable current whenever a level μ_n is inside the opened bias window $\mu_S - \mu_D = -|e|V_{SD}$, i.e. $\mu_S \geq \mu_n \geq \mu_D$. Thus, when the conductance G is plotted as function of the gate voltage V_i one observes *Coulomb resonances* spaced by the addition energy

$$E_{add} = \mu_{N+1} - \mu_N = E_C + \delta E. \quad (3.3)$$

δE is the quantum mechanical level spacing and depends on the electron number on the dot. It can be zero when two consecutive electrons are added to the same spin-degenerate orbital, or when there are orbital degeneracies as often observed in CNT QDs. In InAs QDs a 2-fold pattern of the conductance peaks is expected due to spin-degeneracy, as schematically drawn in fig. 3.2c. The exact size of δE depends on the precise shape of the confinement potential.

3.1.2. Coulomb peak line shape

The magnitude of the conductance peaks is given by the tunnel barriers which are characterized by the tunnel rates Γ_S and Γ_D indicated in fig. 3.2a. Using a Landauer-Büttiker theory, the transmission through such a the double barrier structure can be calculated. The energy dependence of the transmission is approximated by a Lorentzian [47] and the conductance given by

$$G(V_i) = \frac{2e^2}{h} \frac{\Gamma_S \Gamma_D}{\Gamma_S + \Gamma_D} \frac{\Gamma}{(e\alpha V_i)^2 + (\Gamma/2)^2}, \quad (3.4)$$

where $\Gamma = \Gamma_S + \Gamma_D$ in units of energy. This level broadening Γ can be understood by the uncertainty relation for energy $\Delta E \Delta t \gtrsim \hbar$. For a transport process through a quantum dot this means that the classical energy conservation may be violated up to $\Delta E \sim \hbar/\tau$ when the electron is residing on the dot only for the short time τ . This allows electrons to tunnel through the structure even if the level is not fully aligned with the leads. The transmission is one at zero energy when the source and the drain coupling are equal, i.e. $\Gamma_S = \Gamma_D$. One says that the QD is *in resonance* in analogy to a Fabry-Pérot resonator. The lifetime broadening has the characteristic energy Γ corresponding width of the resonance at half maximum (FWHM). This regime is called strong coupling or lifetime broadened regime .

Above we assumed that the thermal broadening of the leads is small, i.e. $k_B T \ll \hbar \Gamma$. For larger temperatures ($k_B T \gtrsim \hbar \Gamma$) the width of the Fermi distribution of the electrons in the contact metal results in thermal broadening of the Coulomb peaks. The theoretical treatment involves Hamiltonian with the tunnelling as perturbation but includes the electron-electron interaction. Beenakker gives for the line shape [84]

$$G(V_i) = \frac{e^2}{h} \frac{1}{4k_B T} \frac{\Gamma_S \Gamma_D}{\Gamma_S + \Gamma_D} \cosh^{-2} \left(\frac{e\alpha V_i}{2k_B T} \right). \quad (3.5)$$

With increasing temperature the peak height scales with $1/T$ whereas the peak width (FWHM) is proportional to temperature with a factor 3.5: $e\alpha\Delta V_i^{FWHM} \approx 3.5k_B T$. The analysis of the peak shape(s) allows us to determine the transport regime and the peak height allows the extraction of the ratio Γ_S/Γ_D . Eq. 3.5 describes the thermal-broadened / weak coupling regime. Both presented equation in this section allow to extract two absolute values for Γ_S and Γ_D but they cannot be assigned to the respective leads.

3.1.3. Coulomb Diamonds

So far, the linear response limit was assumed ($V_{sd} \ll k_B T$) and Coulomb blockade was only lifted by gate tuning. However, when larger bias voltages are applied CB can also be overcome as sketched in fig. 3.3. In situation I the QD is in blockade at $V_{sd} = 0$. By increasing the bias a level enters the bias window and the current is increased step-like. Because the differential conductance is measured this leads to a peak marked by a color change. The whole plot of conductance versus gate voltage and bias voltage is known as *charge stability diagram* of the QD. The measured pattern in one of our device is enhanced and completed by dashed lines. They form diamond shaped areas in which current is suppressed and are often referred as Coulomb diamonds. Inside the diamonds the number of electrons on the QD is fixed whereas outside it is fluctuating because at least one level lies within the opened bias window. The diamond shape in particular can be understood by inspecting the situations I-III in fig. 3.3 and considering the source and drain capacitances C_S and C_D ¹.

Starting from a resonant position at $V_{sd} = 0$ and increasing bias voltage at the source contact, the level μ_N will be pulled along due to the capacitance of the source contact and is shifted by an amount of $\Delta\mu_N = -|e|V_{sd}\frac{C_S}{C}$. In order to keep the resonance aligned with the drain lead the shift can be compensated with the gate voltage by $|e|\Delta V_G\frac{C_G}{C}$ corresponding to situation I in fig. 3.3. Along this negative slope the level μ_N stays aligned with the drain chemical potential μ_D . The value of the slope is obtained by evaluating $\frac{\Delta V_{sd}}{\Delta V_G} = m_- = -\frac{C_G}{C_S}$. By similar considerations the positive slope $m_+ = \frac{C_G}{C - C_S}$ is calculated along which the level μ_N is in resonance with the source. The slopes m_+ and m_- are quite useful for obtaining the gate lever arm. A little bit of math gives $\alpha_G = \frac{|m_+||m_-|}{|m_+|+|m_-|}$. With knowledge of the gate lever arm α_G the charging energy and the addition energy are determined from the spacing the Coulomb peaks in gate voltage. Another possibility is to apply such a large bias voltage that an additional level μ_{N+1} is just inside the bias window as shown in the energy diagram II in fig.3.3. In this specific case not the charging energy is read off but the addition energy (eq. 3.3) which includes the level spacing. The estimation of the lever arm via the slopes is usually more precise since the diamond tips (sit. II) are often smeared out. The stability diagram contains more information. For example, it allows to determine of the level spacing δE . An electron on the quantum dot can

¹We treat the case of asymmetric biasing, i.e. the voltage is only applied to the source contact, while the drain side stays at the ground potential. It is the relevant case for all the measurements performed throughout the thesis

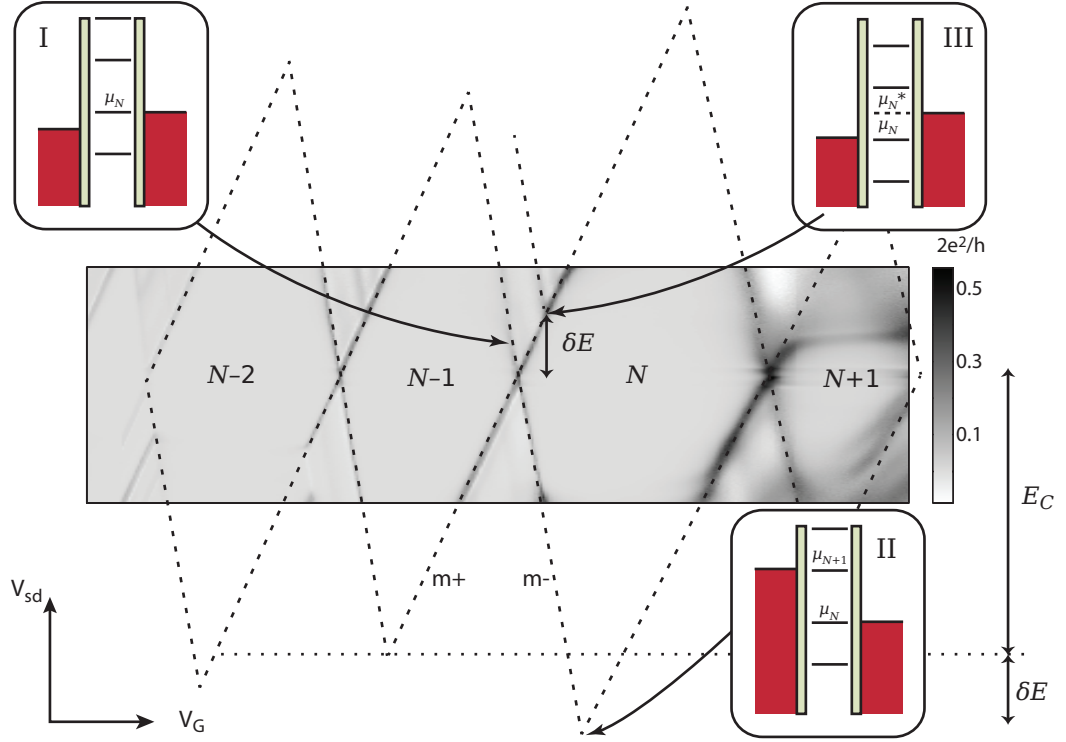


Figure 3.3.: Schematic illustrations of Coulomb diamonds with a underlay of a real measurement performed on one of the quantum dots. Inside the diamond the electron number is fixed and labelled according to fig. 3.2. The different biasing situations I-III are presented in small energy diagrams.

also occupy an excited state instead of the ground state. The excited state is just the next orbital δE away in energy. In situation III in fig. 3.3 the bias voltage is just large enough that the excited level μ_N^* is accessible by the electrons from the leads. In the Landauer-Büttiker picture this corresponds to an additional conductance channel, thus the current will increase. Other transport processes can occur. Higher order tunnelling processes allow transport and lift the Coulomb blockade.

3.1.4. Quantum Dot States in Magnetic Field

The spins in quantum dot will align parallel or anti-parallel to an external magnetic field. The spin degeneracy is lifted and the corresponding resonances will separate linearly in energy with field according to $\Delta E_Z, N = g_N^* \mu_B B$, where g_n^* is the effective g -factor of n th quantum level and μ_B is the Bohr magneton. This is known from atomic physics as the Zeeman effect [85]. The large electron g -factor of InAs nanowires is inherited from bulk InAs and leads to energetically separated spin states already in relatively small magnetic fields.

The g -factor of a quantum dot level can deviate from the bulk value $g^* = -14.9$

[86, 87]. It depends on the electron wave function in the confinement potential and has been shown to be reduced towards the free electron value 2 in very small QDs [88], sometimes called quenching of the orbital angular momentum.[89]. In a distorted confinement potential, the orbital angular momentum is direction dependent what also renders the g -factor anisotropic (into a g tensor).

In addition to the linear Zeeman splitting, the energy of a quantum dot state with spin $s = \pm 1/2$ [47]

$$\epsilon_N, s = \gamma B^2 + sg_N^* \mu_B B, \quad (3.6)$$

will have a quadratic dependence on the magnetic field. An effect known as diamagnetic shift which has an experimentally determined proportionality constant γ , reflecting the diamagnetism of the QD where an induced magnetic moment couples to the external field.

In the measurement of the linear conductance as function of gate voltage and magnetic field, the Coulomb peak position shifts according to eq. 3.6 until the Zeeman energy ΔE_Z is as large as the level spacing δE . At this field a ground state transition happens and the electrochemical potential of the Nth electron will evolve according to another quantum state. If the level spacing is too small the Zeeman splitting is obscured. Here we only discuss the case $\delta E \gg h\Gamma, k_B T$.

Also the peak height depends on B . In larger chaotic quantum dots mesoscopic fluctuations lead to different wave function overlaps of the QD states with the source and drain electrodes. In random matrix theory (RMT) it was found that the peak height modification by the magnetic field is universal and happens on the characteristic scale [82]

$$B_C \sim \frac{\varphi_0}{A_{dot}} (\delta E / \kappa E_T)^{1/2}$$

where φ_0 is the magnetic flux quantum, A_{dot} the dot area, E_T the Thouless energy and κ a geometrical factor of order 1. This leaves us with a characteristic scale of ~ 250 mT assuming a dot size of 80 nm.

The large g -factor of InAs advantageous for our investigation. A Zeeman splitting larger than the common level broadening of $\Gamma = 200 \mu\text{eV}$ (sec. 5.0.2 & 5.0.3) is readily achieved with fields smaller than 230 mT. This leaves the influence of the diamagnetic shift and the varying amplitude small.

3.2. Kondo Correlations in Quantum Dots

For the investigation of the g factor a peculiar electron correlation mechanism called Kondo effect is useful. Therefore a short introduction is given in the following. More complete ones can be found in references [90, 91].

Already in the 1930ies an anomalous increase in the low temperature resistivity of certain metals was observed. At the time the it was understood that the scattering on lattice vibration gives temperature dependence $\propto T^5$ along with a saturation at low temperture due to lattice defects and impurities. Only by 1964 Jun Kondo could

explain the effect satisfactory, after it became evident from experiments that the magnetic impurities play the crucial role [92]. By summing up higher order spin-flip processes at a magnetic impurity he obtained a logarithmic increase for the scattering probability, in agreement with the experiments.

A nice insight into the Kondo effect can be gained when it is regarded from Anderson impurity model. An impurity site is embedded into a metallic host and occupied by a single spin. Its energy is ϵ_n below the Fermi energy. Further, double occupancy is forbidden by the Coulomb interaction energy E_C . The full Hamiltonian and mathematical treatment is given elsewhere [93]. Additional interaction terms in the Hamiltonian allow now the electron to hop to exchange with electrons at the Fermi energy. Afterwards an electron with opposite spin from the Fermi level can occupy the impurity site. Figure 3.4a-c summarizes the lowest order spin flip process. Many

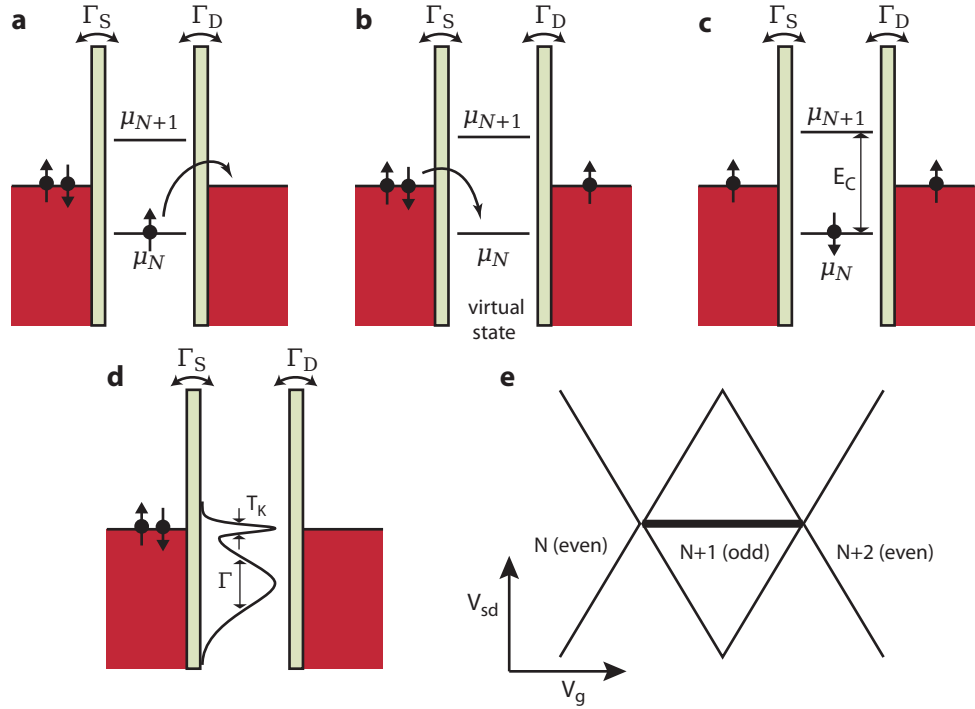


Figure 3.4.: **a** | A quantum dot containing an odd number of electrons being Coulomb blockade (CB). A single electron can hop to the Fermi edge of a lead leaving the QD in energetically forbidden (virtual) state as in (b). **b** and **c** | An electron with opposite spin may tunnel from the leads into the QD. **d** | Successive of these co-tunnelling events generate a additional tunnel density of states at the Fermi level of the leads. **e** | Schematic stability diagram. The Kondo ridge is visible as black bar at zero bias in the odd Coulomb diamonds.

of these processes effectively screen the localized impurity spin. The electrons taking part in its vicinity form the so called Kondo cloud. Crucial for energy gain of this effect is the exchange interaction mediating a spin singlet formation between the localized impurity spin and the electrons spins at the Fermi edge.

In order to form this correlated many-particle state, the electrons in the Fermi sea will have to localize around the impurity. A process which costs energy. Therefore a competition between energy gain of the delocalization of the impurity spin and the energy loss of the localization of the free electron spins is on. At low temperature the delocalization dominates. The transition temperature is known as the Kondo temperature T_K and given by [94]

$$k_B T_K = \frac{1}{2} \sqrt{\Gamma E_C} e^{\pi \epsilon_N (\epsilon + E_C) / \Gamma E_C}. \quad (3.7)$$

Here, $\epsilon_N = \mu_{S/D} - \mu_N$ is the energy separation between the Fermi level in the leads and electrochemical potential of the Nth electron and E_C and $\Gamma = \Gamma_S + \Gamma_D$ are the charging energy and tunnel couplings of the impurity site, respectively. The Kondo temperature can be seen as the binding energy of the new many-body ground state.

The Kondo effect in quantum dots is insofar different as transmitted electrons instead of scattered electrons are considered. The basic physics is unchanged and in the above argument 'impurity site' can be replaced by 'quantum dot'. Galzman Raikh, predicted 1988 that a fully transmissive channel develops ($G = 2e^2/h$) when the temperature is lowered towards zero [95]. Often, this is depicted with an additional density of states (DOS) pinned at the Fermi level of the leads (fig. 3.4d) Obviously, the Kondo effect occurs only if a spin-degenerate QD state is occupied by a single unpaired electron. Hence, it should be observed at zero bias anomaly in the odd electron number diamonds as it was indeed ten years later [96, 97]. Figure 3.4e shows a schematic representation of such a Kondo ridge in a InAs nanowire QD. The width of the resonance in energy is proportional to $k_B T_K$.

From eq. 3.7 it is evident that the strength of the Kondo effect is varied by the QD parameters charging energy E_C , level broadening Γ and level position ϵ_N . The amplitude of the Kondo peak decreases dramatically with increasing temperature. In order to still observe the Kondo effect at accessible temperatures, the coupling Γ needs to be large with the condition to be still smaller than mean level spacing δE as found in small quantum dots in the strong coupling regime.

For our purpose the magnetic field evolution of the Kondo resonance is important since we want to observe the Zeeman splitting. Figure 3.5a shows such a situation where the spin degeneracy is lifted and the spin down level has become an excited state (marked by a dashed line). The QD is still in Coulomb blockade and only co-tunneling events are possible. A spin flip can still occur, but will leave the QD in an excited state (fig. 3.5b). This is an inelastic co-tunneling process with the energy provided from the bias. Thus, the source drain bias voltage must be equal to the Zeeman energy $eV_{sd} = g^* \mu_B B$ and the Kondo resonance splits by

$$\delta = 2E_Z = 2g^* \mu_B B \quad (3.8)$$

Meir *et al.* calculated the tunneling DOS for such a non-equilibrium situation with a finite magnetic field [98]. They found the Kondo effect still present with decreasing strength at large bias voltages V_{sd} . The schematic stability diagram in fig. 3.5c depicts the expected measurement. The two thick bars correspond to an increased conductance pinned at the bias voltages $V_{sd} = \pm E_Z/e$.

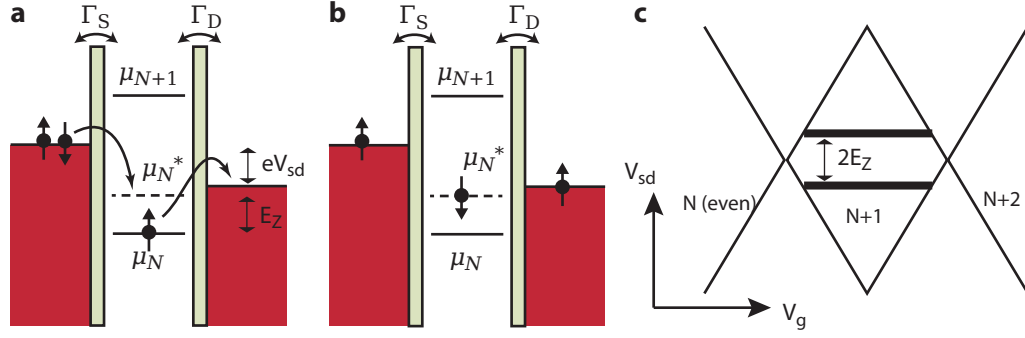


Figure 3.5.: **a** | Energy diagram for a spin flip process at finite magnetic field through a QD. The QD is in Coulomb blockade and occupied by a single spin in the ground state. The excited state μ_N^* is higher in energy by $E_Z = g^* \mu_B B$ higher in energy. The electron in the ground state tunnels out to the drain lead, while an electron with opposite spin tunnels from the source lead into the QD. **b** | After this process the QD is in an excited state. **c** | Schematic stability diagram displaying two horizontal Kondo resonances split by $2E_Z$.

3.3. Superconductivity

Here we provide a short introduction of the BCS theory of superconductivity and then focus on processes occurring at interface between a QD and superconductor. For an extended introduction the reader is referred to the two books [99, 100].

Two basic phenomena define superconductivity. The first is known since 1911 when Kamerlingh Onnes found that the electrical resistance of mercury drops to an unmeasurable, small value at a critical temperature T_C [101]. Soon, many other elements were discovered that showed the same effect with T_C in the range from a few mK to 10K.

The second phenomenon is the Meissner-Ochsenfeld effect named after its discoverers [102]. A magnetic field is completely expelled from superconductor state. A feature called as well perfect diamagnetism. From thermodynamic considerations follows the existence of a critical field B_C above which the superconductivity breaks down. A short reasoning for the two phenomena will be given as soon as the microscopic explanation of superconductivity has been presented.

3.3.1. Cooper Pairs

Only 46 years later after the the discovery of Onnes, 1957, Bardeen, Cooper and Schrieffer presented a satisfying theory explaining the phenomena of superconductivity. At the heart of the theory lies a fundamental theorem worked out earlier by Leon Cooper [103].

In the presence of a weak attractive interaction, two electrons in a Fermi sea can bind together forming a so called Cooper pair. The weak attraction has to overcome the Coulomb repulsion of the two electrons. In a simple picture the attractive interaction is mediated by lattice deformations caused by a passing electron. The ion cores

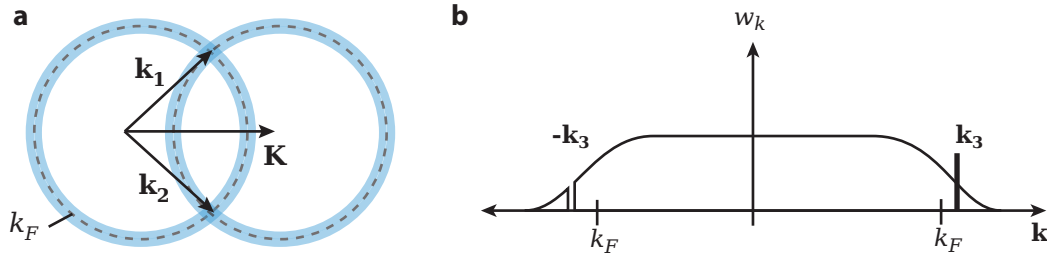


Figure 3.6.: **a** | Illustration of an electron pair scattering event in the momentum space. The blue circles show the allowed initial and final states around the magnitude of the Fermi wavevector k_F . Upon the exchange of a virtual phonon the total momentum is conserved ($\mathbf{K} = \text{const.}$). Only states in the intersection of the two circles fulfill this condition. The number of possible scattering events is maximized for $\mathbf{K} = 0$ and with it the energy gain of the Cooper pair formation. **b** | The need for the empty states for the scattering events leads to an occupation of states higher than k_F even at zero temperature similar to the Fermi distribution. A single electron state at \mathbf{k}_1 is excited into quasi-particle having mainly electron but also hole character due to the diminished occupation at $-\mathbf{k}_1$. Adapted from ref. [100]

get an impulse by the electric field of the passing electron and start to move towards each other polarizing the volume. This lattice polarisation attracts the second electron. The motion of the ion cores lags behind the passing electron. Comparing the Fermi velocity with the phonon oscillation period yields that the electron has travelled about 100 nm before the ion cores reach the maximal displacement. At this distance the Coulomb repulsion is effectively screened by other electrons and the attraction is present.

In a quantum mechanical derivation the attractive interaction is ascribed to the exchange of virtual phonons² between the electrons. For the argument only two electrons with wave vectors $\mathbf{k}_1, \mathbf{k}_2$ and total momentum $\mathbf{K} = \mathbf{k}_1 + \mathbf{k}_2$ are considered to experience the attractive interaction. After the exchange of a virtual phonon with vector \mathbf{q} , the electrons will have the new wave vectors $\mathbf{k}'_1 = \mathbf{k}_1 + \mathbf{q}$ and $\mathbf{k}'_2 = \mathbf{k}_2 - \mathbf{q}$. The available phonon energies limit the energy transfer of the scattering event and are cut off at the Debye frequency ω_D . At low temperature the Fermi distribution has very small width around the Fermi energy E_F , so that all the interactions happen in a small energy range around the Fermi energy $E_F \pm \hbar\omega_D$. In reciprocal space this corresponds to a narrow shell around the Fermi sphere. Figure 3.6 illustrates the possible events for a total momentum $\mathbf{K} \neq 0$ which are restricted to the small area where both shells overlap. The probability of a phonon exchange is maximised when the two shells are congruent, i.e. $\mathbf{K} = 0$. It is the number of all these scattering events in the shell around E_F that giving the energy gain of the Cooper pair formation. The scattering probability has strong dependence on \mathbf{K} and drops drastically for small

²Due to energy conservation the emitted phonon of one electron is only allowed to exist with a timescale given by the uncertainty relation before it is 'captured' again by another electron. Hence the term virtual phonon is often used [100]. We emphasize that the a real phonon state has to exist.

increases in \mathbf{K} . This means that the two electrons of the Cooper pair will have a opposite momenta $\mathbf{k}_1 = -\mathbf{k}_2 = \mathbf{k}$. Hence, the orbital wave function of a Cooper pair can be written as product state of two plane waves [100]

$$\Psi(\mathbf{r}_1, \mathbf{r}_2) = \sum_{\mathbf{k}} g_{\mathbf{k}} e^{i\mathbf{k} \cdot \mathbf{r}_1} e^{-i\mathbf{k} \cdot \mathbf{r}_2} \quad (3.9)$$

where $|g_{\mathbf{k}}|^2$ gives the occupation probability of the state $(\mathbf{k}, -\mathbf{k})$. Because we only consider electrons with opposite momenta, $g_{\mathbf{k}}$ is symmetric with respect to \mathbf{k} . Thus the orbital wave function Ψ is symmetric with respect to the exchange of the electrons. In order to restore the antisymmetry requested by the Pauli exclusion principle the electrons are in a singlet state

$$|\Psi\rangle = \frac{1}{\sqrt{2}} (|\uparrow\downarrow\rangle - |\downarrow\uparrow\rangle) \quad (3.10)$$

in which the spins of the two electrons form a maximally entangled state. This insight is of great importance for our motivation of the experiments performed in chapter 7.

3.3.2. The BCS ground state

The argument by Cooper also implies that Fermi sea becomes unstable due to the presence of the attractive interaction. In the above reasoning, we only considered a single pair of electrons gaining energy on the background of the Fermi sea, but more Cooper pairs can form until an equilibrium state is reached and further Cooper pairs provides no energy gain. The new ground state will differ qualitatively from the Fermi sea. The one year later published BCS theory takes into account all the electrons in the original Fermi sea. The derivation of the ground state is mathematically lengthy. Hence, we will only motivate the basic physics and present the most important results relevant for our experiments.

Since the total spin of a Cooper pair is zero they obey bosonic statistics. Thus, Cooper pairs can condense to a coherent ground state. Usually a superconducting order parameter $\Delta(\mathbf{r})$ is assigned, whose amplitude corresponds to the Cooper pair density, but also has a macroscopic phase.

The scattering process with a virtual phonon from state $(\mathbf{k}, -\mathbf{k})$ to a state $(\mathbf{k}', -\mathbf{k}')$ requires the latter state to be empty. Therefore, electrons will be excited into states above E_F in order to make the some scattering possible. This means an increase in kinetic energy which is weighed against the energy gain due the all the scattering processes. The formation of new Cooper pairs therefore stops at the point where the kinetic energy exceeds the potential energy gain from Cooper pair formation. Figure 3.6b shows the probability ω_k that the state $(\mathbf{k}, -\mathbf{k})$ is occupied by a Cooper pair. Thus, the Fermi surface is smeared out in the state of minimal energy and even at zero temperature.

One of the most important results from BCS theory is the excitation spectrum of a superconductor. An energy gap appears around E_F for excited single electron states.

The energy of these states can be described by

$$E(k) = \sqrt{\varepsilon(k)^2 + \Delta^2} \quad (3.11)$$

where $\varepsilon(k) = \frac{\hbar^2 k^2}{2m} - E_F$ is the energy of a single free electron with respect to the Fermi energy E_F . Δ is superconducting gap parameter. An excitation in a superconductor means that a Cooper pair in the state $(\mathbf{k}, -\mathbf{k})$ has ceased to exist, e.g the state $-\mathbf{k}$ is empty while \mathbf{k} is still occupied. In fig. 3.6b this situation is drawn for a wave vector $|\mathbf{k}_3| > k_F$. The pair occupation probability ω_k is increased for \mathbf{k}_3 and diminished for $-\mathbf{k}_3$. In this case about a major amount of electronic character is added to the system but also some hole part due to the missing electron at $-\mathbf{k}_3$. In a similar manner, excitations can have predominantly hole character. This is the reason why excitations are called as quasi-particles; in general they do not have the full charge. The excitation energy to break up a Cooper pair is 2Δ . The spectrum is illustrated in fig. 3.7. The dashed lines indicate the free electron dispersion relation in the normal

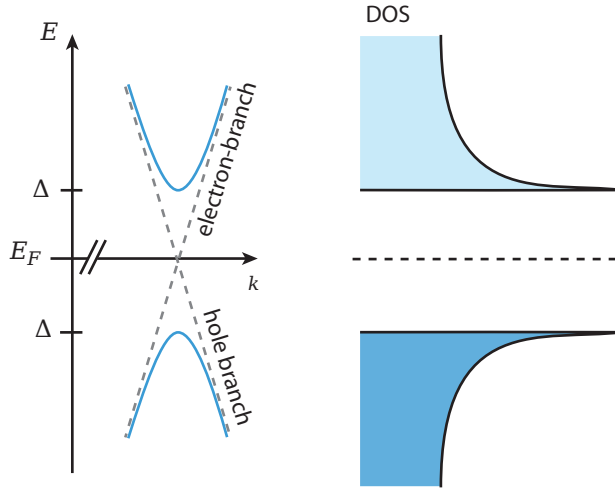


Figure 3.7.: Electron and hole excitation energy in the normal state (dashed line) compared to the quasi-particle energies in the superconductor. The corresponding density of states (DOS) of the quasi-particles is drawn schematically on the right side in the same energy scale.

state. At large kinetic energies the normal full electron or hole character is restored. The density of states (DOS) of the quasi-particle spectrum can be obtained from eq. 3.11

$$D_S(E) = D_N(\varepsilon) \frac{d\varepsilon}{dE} = \begin{cases} D_N(\varepsilon) \frac{E}{\sqrt{E^2 - \Delta^2}} & (E > \Delta) \\ 0 & (E < \Delta) \end{cases}, \quad (3.12)$$

and is depicted on the right side in fig. 3.7. The normal state DOS D_N is usually assumed to be constant in the small window of a few meV around E_F , i.e. $D_N(\varepsilon) \approx D_N(E_F)$. At energies close to Δ the DOS diverges towards the gap edge. For $E < \Delta$

there are no quasi-particle states. This gap is often drawn in analogy to the band diagrams of semiconductors with bearing in mind that the Cooper pair condensate pair exist still at the Fermi energy.

As the temperature is increased from $T = 0$ quasi-particles are excited, thereby reducing the number of Cooper pairs which is related to the superconducting gap. Hence, the gap smears out and finally is reduced. The temperature dependence of the gap can be approximated by [99]

$$\Delta(T) \approx \Delta_0 \left(1 - \frac{T}{T_C}\right)^{1/2} \quad (3.13)$$

where Δ_0 is the gap at $T = 0$. Δ_0 can be set in relation to the critical temperature T_C with further assumptions and approximations $\Delta_0 \sim 1.74k_B T_C$.

The BCS theory provides another important quantity called the BCS coherence length

and is related to the superconducting gap Δ_0 and the Fermi velocity v_F . Using the energy uncertainty $\Delta_0 \sim \Delta p \frac{\hbar}{m} \sim v_F \Delta p$ an estimation by the momentum uncertainty relation $\xi \Delta p \gtrsim \hbar$ leads to

$$\xi = \frac{\hbar v_F}{\Delta_0}, \quad (3.14)$$

the coherence length ξ which describes the spatial extent of a Cooper pair. The values are generally between 10 nm and 100 nm, the same range as already estimated by the phonon interaction. We realize that on this scale about 10^6 to 10^7 other Cooper pairs will have their center of mass [100]. Usually, a collective phase is assigned by making the parameter Δ complex. The state is often described as a 'condensate' of Cooper pairs.

We are now prepared to explain the vanishing resistance and the existence of a critical field. The electrical resistance arises because this momentum relaxes due to collisions with lattice defects and vibrations. When an electrical current flows, all the electrons in the condensate obtain an additional momentum in the direction of the electric field leaving the pairing mechanism intact. In a superconductor inelastic scattering events have to break up the Cooper pair by providing an energy 2Δ to be effective. The current flows without resistance due to the suppressed scattering. When the center of mass momentum \mathbf{P} equals the pair breaking energy 2Δ superconductivity breaks down. All the energy in the current is then dissipated. From this argument it is also reasonable that an external magnetic field can suppress superconductivity when the induced persistent currents reach a critical value. We will use this property to switch our leads between the superconducting and the normal state.

3.3.3. Andreev Reflection

The interesting question is how single electrons and holes carrying the current in a normal conductor can cross over to a superconductor in which the current is mediated by a collective momentum of the Cooper pairs. Understanding the process and the

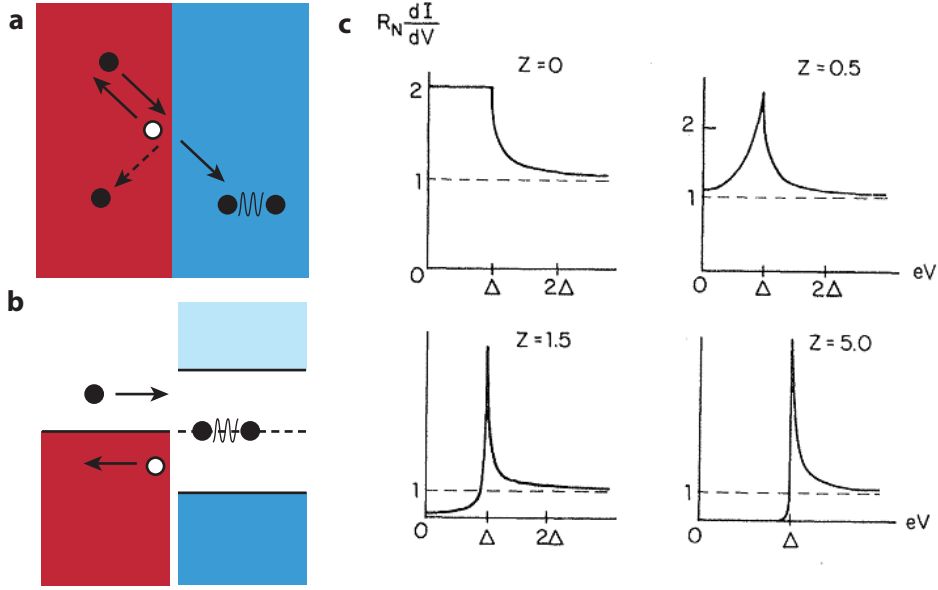


Figure 3.8: **a** | Real space schematic of the Andreev reflection process. An impinging electron (full circle, solid arrow) gets reflected as a hole (empty circle) or partially specularly reflected (dashed arrow) in case the interface is not fully ballistic ($Z \neq 0$). **b** | The Andreev reflection in an energy diagram. **c** | Calculated differential conductance dI/dV by the BTK theory for different interface barrier strength Z [106]

whole normal-superconductor (N-S) interface will be important for the later experiments, e.g. Cooper pair splitting (CPS). We look at the process on a microscopic level.

Let us consider an electron in the normal metal (N) with an energy $E_F < E < \Delta$, larger than the Fermi level but still smaller than the superconducting gap Δ . As the electron impinges onto the superconductor (S) it cannot just enter because there are no available quasi-particle states below Δ which could take up an electron. When we consider a fully transparent interface the electron cannot be reflected, either. Normal reflection (dashed arrow in fig. 3.8) requires a momentum change up to $2p_F$. In absence of a potential barrier at the interface (transparent interface), nothing can provide the momentum needed. A rough estimation of the momentum exerted by the superconductor $\Delta p \sim \frac{dE}{dx} \Delta t \sim \frac{\Delta}{v_F}$ gives values order of magnitude lower than p_F [104].

The dilemma was resolved by Andreev who realized that a hole is reflected from the interface from the interface [105]. The hole will travel backwards along the electron trajectory carrying a positive charge, illustrated as empty circle in fig. 3.8. Upon the reflection process, the charge is therefore changed from $-e$ to $+e$. The Cooper pair condensate in S must be involved in the process and has to take up the total charge $-2e$ impinging at the interface. It does this by simply forming an additional Cooper pair.

The whole process is known as Andreev reflection and can theoretically be described by the popular Blonder-Tinkham-Klabwjk (BTK) model [106]. In this model, a two component wave function approach is made to solve the problem of a barrier at the interface. The scattering potential is modelled as delta function. The boundary condition are such that the wave functions are matched. The treatment is not very difficult but would expand the section unnecessarily. We constrict ourselves to the most important results. In the model a barrier strength Z is introduced to describe the interface. When elastic scattering is absent at the interface, i.e. $Z = 0$, the only process possible is Andreev reflection and the current is increased by a factor of 2 at energies $|E| < \Delta$ compared to both sides being normal. However, the condition $Z = 0$ is never met in reality because it requires dissimilar materials with the same Fermi velocity v_F . Fig. 3.8c shows the calculated differential conductance through an N-S interface for several values of Z . With increased Z , normal reflection at the interface becomes partially possible and a washed out gap starts to appear. In the full tunnel barrier limit $Z \gg 1$ ($Z = 5$ in fig. 3.8), Andreev reflection is fully suppressed at $|E| < \Delta$ and the I-V characteristics of a N-S junction reflect the quasi-particle density of states of the superconductor. The transport through the interface at energies $|E| > \Delta$ is govern by quasi-particles.

For a more complete understanding of the N-S interface consider again an ideal interface with $Z=0$. The time reversed process of fig. 3.8 is also possible. An incoming hole is retro-reflected as an electron while a Cooper pair is removed from the condensate. This process is often referred as leaking of Cooper pairs into N. The Cooper pair can be viewed to gradually evolve into a quasi-particle as it passes over the interface. The quasi-particle consisting of an electron and a hole part slowly loses its phase relation on the length scale of phase coherence length in N. However the process depends also the energy of quasi-particle. The nice insight of T.M. Klapwijk [107]

In absence of any attractive interaction there is still a finite probability of finding a Cooper pair in N which is equivalent to stating that the Andreev reflected electrons and holes maintain phase-coherent over certain length [...]

relates the Andreev reflection also to the superconducting proximity effect.

The crucial point for us is that the Andreev process is coherent and the spin state of the Cooper pair is also transferred across the interface leaving the electron and hole in singlet state. When the electron and hole are spatially separated one would have source of entangled electrons for a test of entanglement. We will see in the next section that a non-local version of Andreev reflection indeed exists.

3.4. Cooper pair splitter devices

3.4.1. Crossed Andreev Reflection

The Andreev reflection discussed in section 3.3.3 was the reflection of a hole upon an electron impinging on the N-S interface. From momentum and charge conservation it became clear that the hole moves back along electron trajectory and a Cooper pair is formed. Since the Cooper pairs have a spatial extent of the superconducting coherence length ξ , the hole does not need to be reflected from the same position, but up to $l \lesssim \xi$ apart. In devices with multiple terminals, electron and hole can even go into different leads giving rise to cross conductances. In the simplest case two normal leads, N1 and N2, are connected to a superconductor S within a small distance. A schematic of the device and the process is shown in fig. 3.9a where an incoming hole in lead N1 is reflected as electron into lead N2. This non-local analogue of the Andreev process is known as crossed Andreev reflection (CAR). In the discussion about Andreev reflection we left out the fact that hole and electron have to be in a spin singlet state because Cooper pairs are too, a result of the coherence of the process. Also in the reverse process, the non-local generation of a Cooper-pair, the incoming electron need to have spin up and reflected hole spin down or vice versa. Thus, CAR triggered a lot of attention as potential source for spin entangled electrons.

In metallic structures first hints to a CAR process were found [108, 109]. However other processes tend to mask or cancel the CAR signal. For example, an incoming electron in N1 can also be transmitted to N2 via a higher order process involving a quasi-particle state above Δ . This non-local process is called elastic co-tunnelling (EC) and analogous to the co-tunnelling discussed through quantum dots (section: 3.2). The exact contributions of EC and CAR to the current can be modelled, for example by the scattering matrix approach by with the scattering matrix approach. However, it turns out that EC and CAR have same order of magnitude and both depend and decay exponentially over ξ [110].

3.4.2. Cooper pair splitter with quantum dots

In purely metallic N-S-N junctions it is difficult to enhance CAR over EC since these structures provide very little control over the individual transport processes. In a influential paper from 2001, Recher et al. proposed to lift this drawback by inserting tunable quantum dots between N and S. Figure 3.10a shows a schematic of the proposed device which we shall call Cooper pair splitter (CPS). Ideally all the listed parameters in fig. 3.10a would be tunable to improve the Cooper pair splitting efficiency: The couplings of the QDs to the normal leads (Γ_{N1} , Γ_{N2}) and to S (Γ_{S1} , Γ_{S2}) as well as the level positions ε_1 , ε_2 and the charging energies $E_{C,1}$, $E_{C,2}$ of each QD could be tuned for example by local gate voltages. The chemical potentials of the leads, μ_{N1} , μ_{N2} and μ_S , are controlled by the applied bias voltage and superconducting gap Δ by an external magnetic field. δr denotes the distance between the two tunnelling points of the Cooper pair electrons. The ingenious part of the idea by Recher *et al.* is that the quantum dots by themselves ideally suppress tunnelling

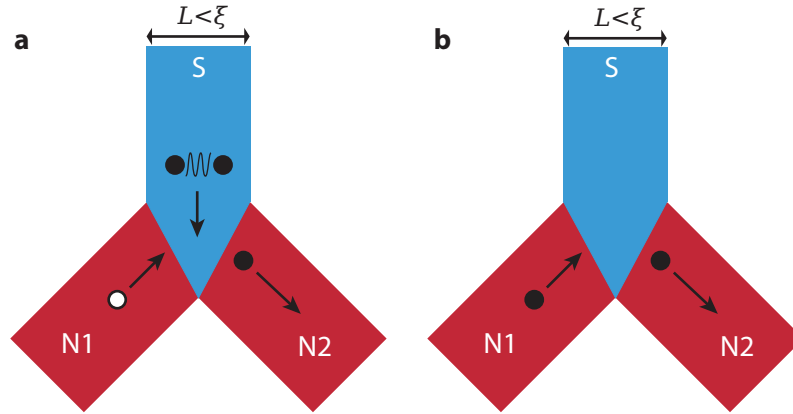


Figure 3.9.: **a** | Illustration of the non-local Andreev reflection (CAR) in a three terminal device. If two normal leads (N1,N2) are connected to a superconductor S within ξ , CAR is possible **b** | Illustration of the non-local analogue of the specular reflection known as elastic co-tunneling (EC). Electrons in the normal leads can be transmitted into the other lead via virtual quasi-particle states in S.

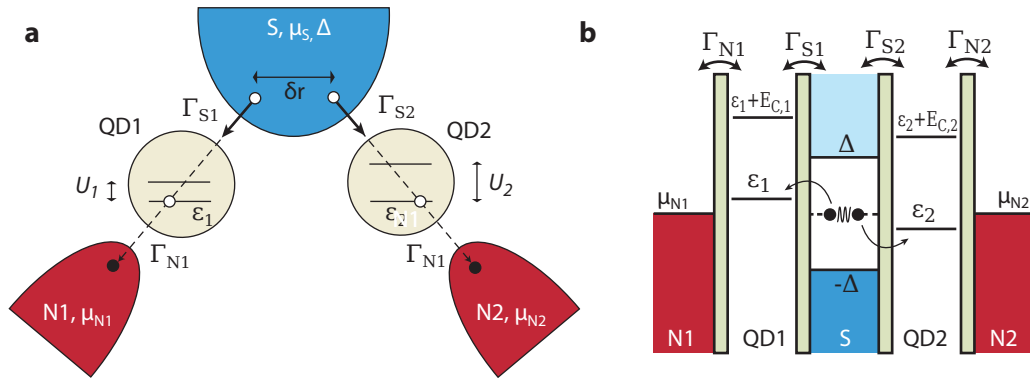


Figure 3.10.: **a** | Schematic of the the Cooper pair splitter device with all relevant energies and couplings. Adapted form [111] **b** | The same device in an energy diagram. Adapted from [112, 113]

of a Cooper pair into the same lead thereby enhancing the CAR process. This local pair tunnelling (LPT) has two possible routes: a pair directly tunnels to a quantum dot corresponding to local Andreev reflection (LAR) or the electrons of a pair tunnel one-by-one through a QD. The former process, LAR, is suppressed by $1/E_C$ (for the theoretical discussion we will assume $E_{C,1} = E_{C,2} = E_C$). Due to the Coulomb interaction on the quantum dots ($E_{C,1}$, $E_{C,2}$) double occupancy is unlikely. The second electron of a Cooper pair can only tunnel onto the QD at an energy cost of E_C and then leave to the normal lead. In the second process, the Cooper pair breaks up and the electrons tunnel sequentially through the QD (sequential pair tunnelling, SPT). While the first electron tunnels, the second is excited to an electron like quasi-particle state above Δ . If the first electron tunnels out to the lead the second electron can follow after it, without double occupancy of the QD. The process is suppressed by $1/\Delta$, the energy of the quasi-particle excitation.

Cooper pair splitting and local pair tunnelling current

Quantitative expression for the Cooper pair splitting current and the local pair tunnelling current were obtained by Recher *et al.*

$$I_{\text{CPS}} = \frac{e\Gamma_S^2\hat{\Gamma}}{(\varepsilon_1 + \varepsilon_2)^2 + \hat{\Gamma}^2/4} \exp\left(-\frac{2\delta r}{\pi\xi}\right) \left[\frac{\sin(k_F\delta r)}{k_F\delta r}\right]^2. \quad (3.15)$$

The first term is a double Breit-Wigner resonance around the energy levels $\varepsilon_1, \varepsilon_2$ of the QDs whereas the broadenings are defined as $\hat{\Gamma} = \Gamma_{N1} + \Gamma_{N2}$ and $\Gamma_S = \Gamma_{S1} = \Gamma_{S2}$. The second term in eq. 3.15 includes the spatial separation of the two tunnelling points δr as illustrated in fig. 3.10a. The CPS current decays exponentially with the superconducting extent of the Cooper pairs ξ what is plausible since the coherence length reflects the spatial extent of the Cooper pairs. The last term is a geometry dependent factor which is discussed separately further below. For now we assume the last two terms constant and set it to $P(\delta r) = \exp\left(-\frac{2\delta r}{\pi\xi}\right) \left[\frac{\sin(k_F\delta r)}{k_F\delta r}\right]^2$.

The double Breit Wigner resonance takes its maximal value at $\varepsilon_1 = -\varepsilon_2$

$$I_{\text{CPS}} = \frac{4e^2\Gamma_S^2}{\hat{\Gamma}} P(\delta r), \quad (3.16)$$

The local pair tunnelling current includes both local processes, LAR and SPT, and its maximum is given by

$$I_{\text{LPT},i} = \frac{2e\Gamma_S^2\Gamma_{Ni}}{\mathcal{E}^2}, \quad \frac{1}{\mathcal{E}} = \frac{1}{\pi\Delta} + \frac{1}{E_C}, \quad (3.17)$$

where $i \in \{1, 2\}$ is a label for the respective QD.

For the suppression to work in both cases the energy should be provided neither by the temperature nor by a bias voltage³. We therefore require $k_B T \ll U, \Delta$ and $|eV_{\text{sd}}| \ll U, \Delta$ what makes large Δ and E_C advantageous for the CPS. In principle 100% efficient device could be achieved with E_C and Δ being large enough.

³In section we will give experimental evidence that the bias voltage actually can be larger than Δ .

Assumptions

Recher *et al.* states that it is "most efficient" to work in a regime where the QDs should be empty on average. The best way to support this is by requiring $\Gamma_N \gg \Gamma_S$. The electrons will much faster tunnel to normal lead than be refilled with S. This simplified also their model calculation because QD population need not be accounted for. Two more conditions are identified ensuring negligible occupation of the QDs. When $|eV_{sd}| > k_B T$, Γ is fulfilled the quantum dot will indeed be empty all time because the thermal occupation of the QD can be neglected. The small bias voltage prevents the backward processes of the electrons. In general finite occupation of the QDs leads to a competition of the different transport processes.

Additional processes can arise if we take into account an inter-dot coupling Γ_{12} . The electrons can always hop between the QDs by elastic co-tunnelling (EC) or possibly by a direct tunnel barrier if the QDs are close, giving rise to an effective tunnel coupling between QDs. Obviously, an inter-dot coupling can spoil the Cooper splitting process. Both electrons can end up in the same lead although originally split. For example, after a Cooper pair has split, the electron in QD1 leaves to N1. Then the electron in QD2 has a finite chance to tunnel into QD1 and leave also to lead N1. This would increase the current in lead N1 and decrease it in lead N2. With a semi-classical rate equation model co-workers could show that the currents to each lead can indeed be different [19]. For optimal splitting efficiency we therefore require as well $\Gamma_N \gg \Gamma_{12}$ making the electron leave to the leads much more likely.

There is a trick how to lower the elastic co-tunnelling probability. The extracted Cooper pairs have to obey energy conservation, meaning that $\varepsilon_1 = -\varepsilon_2$ if $\mu_S = 0$ for simplicity. By further setting $\varepsilon_{1,2} \neq 0$ elastic processes are suppressed and the co-tunnelling has a reduced probability due to the additional relaxation process.

Spatial decay of crossed Andreev reflection

The last term $P(\delta r)$ is a geometry dependent factor which is ambiguously discussed in literature. Recher *et al.* consider a 3-dimensional ballistic superconductor and find [111]

$$F(\delta r) = \left[\frac{\sin(k_F \delta r)}{k_F \delta r} \right]^2 \quad (3.18)$$

where k_F is the Fermi wave vector of the superconductor. The term proves problematic because for any separation $\delta r > \lambda_F$ the efficiency of a CPS would be severely suppressed. If one assumed a typical separation $\delta r = 150$ nm and takes $\lambda_F = 3.8$ Å from aluminium a factor $\sim 10^{-7}$ is obtained. In reference [114], the superconductor was considered in the diffusive limit, where the mean free path l is shorter than the coherence length. The modification to $F(\delta r) = \sin(k_F \delta r)^2 / (lk_F)(k_F \delta r)$ is marginal: the suppression changes only by one order of magnitude. Interestingly, no indications of such an algebraic suppression have been found in the experiments performed in either CNT [17, 19] or InAs nanowires [16, 18]. Therefore, it seems that the factor $F(\delta r)$ is not active in the calculations due to some bad assumptions. For example, one can

consider 2-dimensional or 1-dimensional superconductors instead of 3-dimensional. $F(\delta r)$ is then proportional to $1/(k_F \delta r)$ and to $|\sin(k_F \delta r)|$, respectively [115, 116]. For 1-d it basically only leaves the exponential decay with the coherence length (second term in eq. 3.15). A 1-dimensional superconductor is for example obtained by virtue of the proximity effect when a 1-d conductor is coupled to a superconductor. Indeed it was speculated that in CNT and InAs nanowire devices the Cooper pairs are actually split in the 1-dimensional wire segment below the S lead and not from the bulk superconductor [16, 112]. Another reason could be that δr is actually small and the Cooper pairs tunnel always from a single point in the device.

Efficiency and regime of interest

To arrive at the regime of interest we define a splitting efficiency

$$s = \frac{2I_{\text{CPS}}}{I_{\text{tot},1} + I_{\text{tot},2}} = \frac{2I_{\text{CPS}}}{2I_{\text{CPS}} + I_{\text{LPT},1} + I_{\text{LPT},2}}, \quad (3.19)$$

We use the expression from eq. 3.16 and eq. 3.17 to arrive at

$$s = \frac{P(\delta r)}{\hat{\Gamma}^2/\mathcal{E}^2 + P(\delta r)} \quad (3.20)$$

where we note that Γ_S has actually cancelled in the limit $\Gamma_S < \Gamma_N$. If we consider $P(\delta r)$ a constant of order 1 but not larger, the right side of in eq. is simple function of $\hat{\Gamma}/\mathcal{E}$ that is maximized when the ratio $\hat{\Gamma}/\mathcal{E}$ is minimal. For the regime of interest we require therefore Δ and E_C as large as possible and $\hat{\Gamma}$ as small as possible. The condition $\Gamma_S < \Gamma_N$ implies that also the individual $\Gamma_i = \Gamma_N, i+\Gamma_S, i$ of the QDs should small as possible what basically constitutes our design formula. With the discussion in the assumptions the ideal working conditions are summarized as follows

$$\Delta, E_C, \delta E > |eV_{\text{sd}}| > \Gamma, k_B T, \quad \Gamma_N > \Gamma_S, \quad \varepsilon_1 = -\varepsilon_2 \neq 0, \quad (3.21)$$

where $\Gamma = \Gamma_N + \Gamma_S$ still applies.

These ideal conditions are easily abandoned. If, for example, $\Gamma_N \ll \Gamma_{12}$ the splitting efficiency can not exceed 50% [17, 112]. The electrons exchange fast between the QDs and will exit randomly into leads N1 and N2. The large inter-dot coupling causes also hybridization of the two QD levels. In general, as soon as the dot occupation has finite probability competition between the transport processes start a problem which we try to address in the end of chapter 7.

The regime of interest is experimentally feasible. Where earlier work [16, 17, 19] relied basically on luck we can show a first tuning of the different coupling strengths and employ Nb to improve the ratio further.

4. Fabrication and Measurement Techniques

This chapter describes the fabrication of the InAs NW devices and the basic experimental set-up used to measure the produced devices. We will and can only present the concepts and techniques used and sometimes the recipe. But like with cooking the process is learned by doing and a recipe rarely succeeds the first time. So although this chapter is short, a fair amount of time of a PhD student in nanoelectronics goes to work in the clean room and to learning the trade. As in other craftsmanships the processes undergo continuous change and improvement. Thus, the chapter continues after an overview with newly developed techniques to the ones already known in our work group and ends with an introduction to the experimental set-up.

4.1. Fabrication Overview

The sections follows the fabrication for a Cooper pair splitter (CPS) device as used at the end of the thesis. The overview includes most the fabrication steps used in this thesis. Some steps are described in more detail in the later sections or in the appendix. Other device types than CPS just stop at a certain point or leave out some steps. A short fabrication summary is given in the respective chapters which allows to infer the fabrication process.

Wafer cleaning All devices are fabricated on highly doped silicon wafer which is capped with 400 nm silicon oxide (SiO_x). The wafers are cleaned by immersing them in acetone, deionized water and isopropyl alcohol (IPA) and sonicating them in each solvent for 10 min. Afterwards they are exposed to an UV/ozone treatment. When unknown residues persisted, the wafers are alternatively cleaned in a oxygen plasma or in a mild piranha solution.

Base structure fabrication In the next step, standard e-beam lithography (EBL, see next section) is used in order to pattern the wafer with markers that help localize the nanowires and fabricate the further steps. These markers are arranged in a square grid with a basic spacing of $20\text{ }\mu\text{m}$ and cover an area of $0.4 \times 0.4\text{ mm}$. The markers design is completed with closely spaced gate structures that serve later as bottom gates for the NWs. However, the fabrication of these bottom gates requires slightly refined methods and is covered separately in section 4.3. The whole wafer is then covered with SiN_x in a plasma-enhanced chemical vapour deposition process (PE-CVD).

Nanowire deposition The nanowires are placed as perpendicular as possible above the bottom gates by micromanipulators (see section 4.4). Afterwards the nanowires are localized in the dark field of a light microscope (*MX51*, Olympus, Tokyo, Japan.) in which the NWs are visible down to a diameter of 20 nm [117]. An example image can be found in fig. 4.1a. Alternatively, the NWs can be imaged in the SEM for more precise position information. However, we prefer the optical method whenever possible due to its non-invasive character. The electron beam of the SEM might damage the NWs. The position of the nanowire relative to the marker grid is then transferred to a GDS-II file which can be edited with the EBL writing software Elphy (Raith GmbH, Dortmund, Germany). In the latter the needed contact structures are designed around the NW, too.

Electrical contacts to the bottom gates The bottom gates below the insulating SiN_x need to be contacted. For this purpose an etch mask out of PMMA is fabricated by EBL having opened windows close to the NW. A CHF_3 plasma with a small oxygen content etches the SiN_x selectively and stops at the SiO_2 ¹[118, 119]. Subsequently, the etch mask is removed carefully in acetone at room temperature. This step is critical because the NWs can change position or be removed completely by the solvent. A standard lithography step with metallization follows in order to contact the bottom gates. The contact leads are extended to $300 \times 300 \mu\text{m}$ large bonding pads. After development we use an oxygen plasma (recipe in app. A) to remove any resist residues that could compromise the metal-metal contacts. Also here care has to be taken, that the NWs are not flushed away.

Contacts to the nanowire only work if the native oxide on the NW is removed. Prior to metallization, we employ a sulphur passivation based on NH_4S_x solution or physical Ar bombardment which was found to give better contacts [37]. The Ar milling sputters the thin bottom gates away otherwise the fabrication of the normal contacts and the bottom gate contacts are combined. Usually the last step is the fabrication of the superconducting contact. As superconductor we use an evaporated Ti/Al bilayer (4 nm/100 nm) or pure Nb which is sputtered in very high vacuum (5×10^{-9} mbar). In total four to five EBL steps are required for the fabrication of a CPS device, however multiple structures are processed at the same time.

Chip connection In the last fabrication step the Si chips with the fabricated devices are cleaved to $4 \times 4 \text{ mm}$ large pieces which are glued into a chip-carrier with silver paint. This ensures contact to the highly doped Si substrate which acts as global back gate. The other electrical connections between the chip-carrier contacts and the metallic leads are made by wire bonding. Thereby, a thin Al wire is melted locally by an ultra sonic power burst. Because the chip-carrier has only 20 connections we can only bond one CPS device (out of two on a chip) at the time having 12-13

¹A recipe valid for the RIE machine *PlasmaLab 80Plus* (Oxford Instruments, United Kingdom) is given in Appendix A

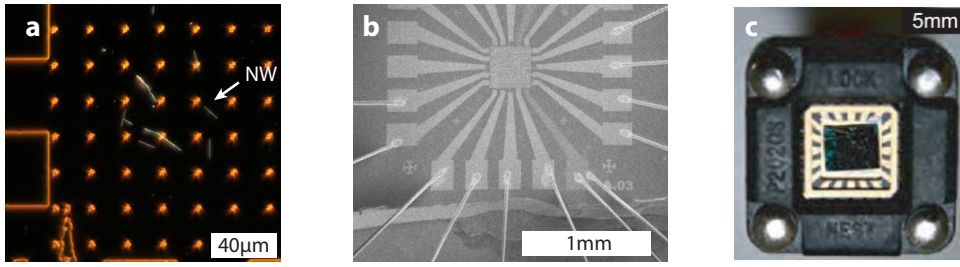


Figure 4.1.: **a** | Optical image of nanowires. In the dark field of the optical microscope the NWs are very well visible. Their position is extracted relative to the markers and used for the design of device. **b** | SEM image of a chip with a finished device that is connected to 12 bonds. The chip is glued into a chip-carrier which can be mounted to a chip-carrier holder. **c** | Optical image of the chip-carrier holder attached to a measurement system. Image source: [120]

connections. From the moment of bonding special care has to be taken to proper grounding of equipment and worker in order to avoid electrostatic discharges (ESD). Their consequences are briefly discussed in the appendix.

This concludes the fabrication and the devices are ready to be tested electrically. If possible, we build the sample directly into a measurement set-up to avoid again unnecessary handling and ESDs. The measurement setups and cryostats are introduced in the last section of this chapter.

4.2. Basic e-beam lithography

The basic steps of the e-beam lithography process are illustrated in fig. 4.2. First, an e-beam resist is applied on the wafer by spin-coating (1.). For this purpose, a solution with resist polymer is spread onto the wafer chip which is afterwards rotated fast. The rotations speed (typically 4000 rpm) and the concentration determine the resulting layer thickness. The resist is then hardened for 5 min on a hotplate at 180°C. As resist polymer, we use either polymethylmethacrylate (PMMA) or ZEP 520K (Zeon Chemicals) [121]. The resist thickness varies between 60 nm and 400 nm depending on the EBL step, but is 350 nm for the standard steps like contact fabrication.

In the second step in fig. 4.2 the desired pattern is written into the resist by a highly focused electron beam. In our lab we use a normal scanning electron microscope (SEM) which is equipped with a RAITH (Raith GmbH, Dortmund, Germany) writing system. During the electron beam exposure the long chains of the polymer break up into smaller segments rendering the exposed parts more soluble. With the right solvent the lighter fragments can be selectively dissolved leaving the unexposed resist intact (3.). The slightly angled profile (undercut) in the resist drawn in fig. 4.2 is due to electron scattering in the resist and in the substrate but is also wanted for the subsequent metallization process. In the fourth step (4.) the chips are placed into a high vacuum chamber and the desired metals are deposited on the polymer

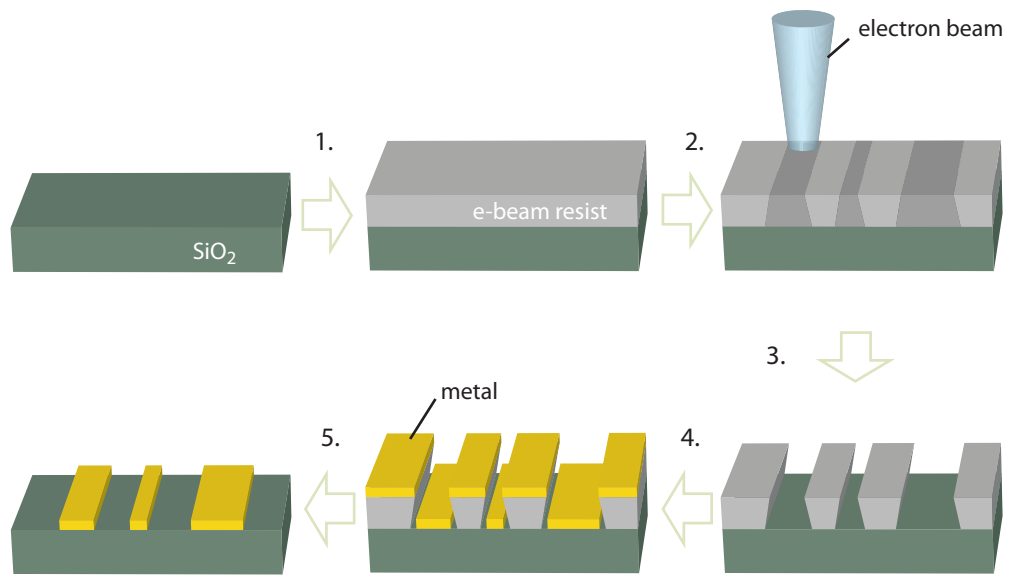


Figure 4.2.: Illustration of a standard e-beam lithography process. The SiO_2 substrate is covered with an e-beam resist (1.) and patterned with a highly focused electron beam (2.). The exposed areas are dissolved in adequate solvent (3.) leaving a profile which is subsequently covered with an evaporated metal layer (4.). Lift-off in warm solvent removes the resist and leaves the desired pattern as metal film.

by e-beam or thermal evaporation or sublimation or by sputtering technique. For the base structure we use Ti/Au (5 nm/45 nm) bilayer or Ti/Pt (4 nm/18 nm) bilayer where the Ti helps the adhesion on the SiO₂ and the heavy elements improve the SEM contrast. The latter property is needed because the so fabricated makers are used for alignment of the additional lithography steps on top of each other. In the last step called lift-off, the resist and the covering metal is removed in warm solvent (5.) while the written pattern stays as metal on the wafer. The undercut profile helps to break the metal layer and lets the solvent creep below it. Regardless, we need to help sometimes the lift-off process by creating a turbulent environment in the solvent with a syringe. The chips are rinsed and blown dry, what finishes the basic EBL step.

4.3. Bottom gate fabrication

Bottom gates offer optimal tunability for quantum dots in InAs nanowires and are currently preferred gate architecture in research devices. Our fabrication methods follow ref. [122]. Bottom gates should be on the size of the nanowire and thus on the limit of our EBL resolution. The resolution can e.g. be increased by using higher acceleration voltages of the electron beam. Therefore, we collaborated with Vitaliy Guzenko from Paul Scherrer Institute PSI (Villigen, Switzerland) to gain access to a dedicated e-beam writing system with 100 kV acceleration voltage. At high acceleration voltages the undercut is reduced due to the large penetration depth of the electrons. To still obtain a pronounced undercut, a bilayer resist system is used, where the lower layer is more sensitive to the energetic electrons and is exposed in a wider area than the top layer. After development, evaporation of a Ti/Pt film was done in house and SiN_x deposition again at PSI. The lift-off and the edge quality of the metal strips could be improved by O₂ plasma before evaporation, but this also yielded wider gates. Reasonable structures with a 100 nm pitch and a line width of 40 nm were eventually achieved in an optimized process

It is also possible to fabricate the bottom gate resist mask with the in house e-beam machines with lower acceleration voltage. ZEP 520K resist with a layer thickness of 60 nm is applied on the well-cleaned SiO₂ wafer surface. An acceleration voltage of 10 kV makes the undercut larger and improves the lift-off process. However, the undercut angle and the resist thickness limit the possible center-to-center pitch. In fig. 4.3a the resist thickness was only increased from 60 nm to 70 nm by accidental evaporation of solvent from the diluted resist solution. It is visible that the resist ridges start to move (red ellipse) because the undercut gets too large in the cleared area and the ridges detach from the surface. Using a lower dose to prevent this, can lead to interruptions of the metal as hardly visible in the yellow ellipse in the same figure. If the line dose is increased to have less faults in the lines, the large exposed areas create additional dose to the nearby bottom gates (proximity effect). In this case lift-off fails (fig. 4.3b) or the dose in the areas has to be lowered below a value for good clearing. Therefore, the fabrication requires a well optimized recipe where different parts of the structure are exposed with a different dose. Successfully

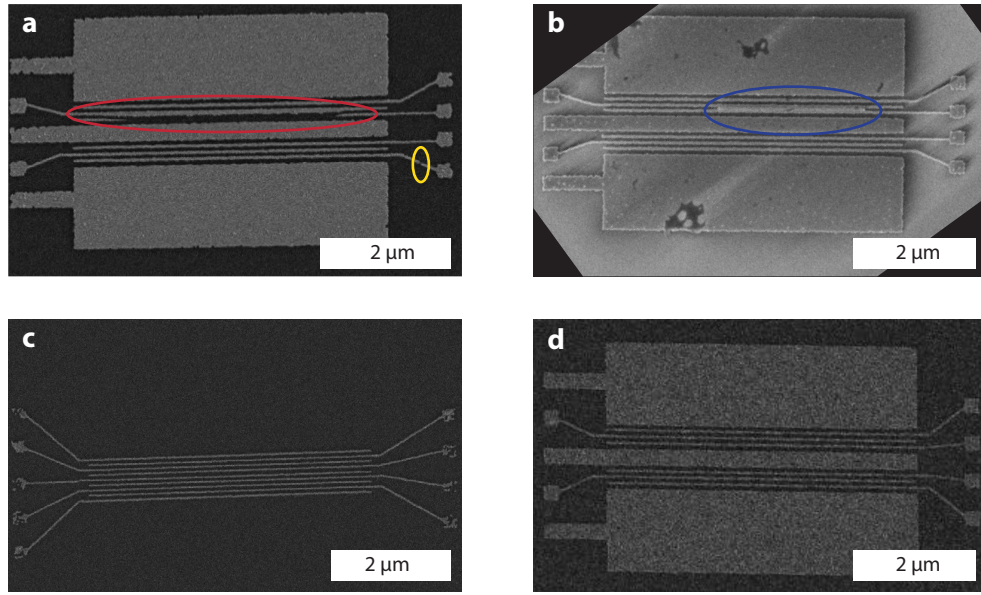


Figure 4.3.: **a** | SEM image illustrating different issues of the in house fabricated bottom gates. The resist ridges detach from the wafer due to too thick resist and a too large undercut (red ellipse) although the e-beam dose is still below a good clearing value and causes interruptions in the metal strips (yellow ellipse). **b** | The large exposed areas lead to lift-off errors (blue ellipse) due to the SEM proximity effect (polymer chain scission outside of the e-beam exposed area) **c** | SEM image of bottom gates with the lowest achieved pitch of 85 nm **d** | Successfully in house fabricated bottom gates.

fabricated bottom gates with 85 nm center-to-center pitch are shown in fig. 4.3c what is better than the 100 nm pitch achieved in collaboration with PSI. A more elaborated bottom gate design used for CPSs could be achieved, too and an example is displayed in fig. 4.3d. The large scale integration over several base structures proves however still demanding.

4.4. Nanowire placement

Three different techniques were used to deposit nanowires on the wafer surface. In the beginning of the thesis, trials were made with dry clean wipes. As the growth substrate is touched by a wipe, nanowires are picked up mechanically. Then the nanowires are deposited randomly as the wipe is wiped over the base structure. The disadvantages of this method are that the nanowires tend to break into shorter pieces and deposition is very unprecise. In a second method, the nanowires are suspended in IPA by sonication and tiny droplets of the suspension are spotted to the base structure. Then the solvent is left to evaporate. Here the amount of nanowires is not very well controlled. The third technique relies on thin glass or In tips used to manipulate single NWs. The used setup and method is described below.

Bottom gates arrays have to be fabricated before the nanowire deposition which makes it desirable to place the nanowires more precisely than by random droplet deposition. Although it is possible to rely on a random distribution the nanowires over many bottom gate structures and the method was also explored, obtaining good position and angle stayed a rare coincidence. Here we present a technique by which one can place individual NWs with micrometer precision and angular precision of a few degrees. Indium (In) or glass tips are used in combination with mechanical micromanipulators (3D) to pick up, move and deposit single NWs. The technique was recommended to us by members of the group of L.P. Kouwenhoven² and is discussed in detail in reference [123]. The set-up used is dedicated to multiple purposes and provided by the group of M. Poggio³.

A photograph of the setup is shown in fig. 4.4a. An optical bright field microscope is used to monitor the NWs during manipulation. It is equipped with two objectives with a large working distance (23.5 mm and 17 mm) leading to a magnification of 100 \times and 1000 \times , respectively. Two manipulators with pneumatic translation are attached to the movable table of the microscope.

Glass tips are pulled from glass rods with a commercial device (*Model PC-10*, Narshige, Tokyo, Japan). The rods are locally heated and their two ends are pulled apart with weights what yields highly reproducible tip shapes. In contrast the In tips are produced manually with the help of a micrometer screw. A droplet of In is placed on a glass slide and heated with a soldering tool to 160-180°C. Then, tungsten carbide (WC) tips attached to the micrometer screw are dipped into the liquid droplet and slowly removed so that a thin In tip is formed. The shape of the tips depends on the temperature of the In and the pulling velocity and presumably also the wetting properties of In on WC which are not ideal, but the WC tips were readily available. The resulting tip radii are for both materials ~ 150 nm, however the In tips are very ductile and deform easily during manipulation whereas the glass tips are stiffer and more elastic.

Manipulating the nanowires requires patience and practice that let us in end pick up single nanowires from the growth substrate. For this purpose a glass tip is preferentially used and placed next to a NW standing upright on the wafer. The tip is then pushed against the NW until it breaks off. Generally, the wire sticks to the tip and it can be moved to the base structure. With the help of a second tip the NW is arranged and brought into contact with the surface where it usually sticks quite well. However, the nanowires do not always lie flat on the wafer or are aligned the intended way. We can correct the position of the NW by pushing them slightly with the tips. Eventually, a lateral accuracy below 1 μ m and an angular accuracy of $\sim 10^\circ$ is reached.

The technique is not ideal for the manipulation of very thin wires. On the one hand, nanowires with diameters below 60 nm are hardly visible in the large WD objectives and the placement has to be cross-checked in the dark field of the optical microscope.

²TU Delft, The Netherlands

³University of Basel, Switzerland

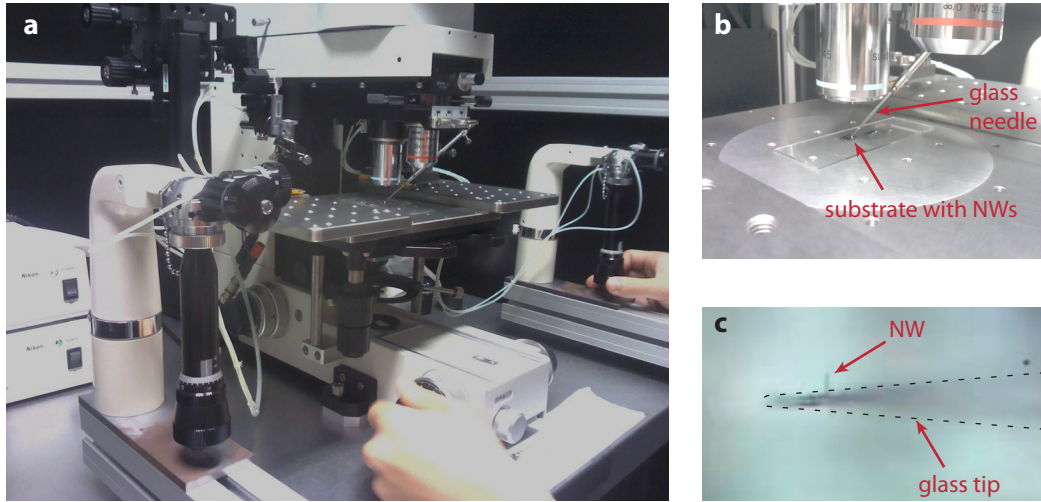


Figure 4.4: **a**| Photograph of the micromanipulation set-up in use. **b**| Close-up on the wafer with the nanowires. A glass needle is approached to the surface and used for nanowire manipulation. **c**| View through the microscope of the manipulation set-up. A single NW adheres to the glass tip of which large parts out of focus but is surrounded by a dashed line as guide to the eye.

On the other hand, thin wires bend and break very easily. If the nanowire needs to be thin and be placed precisely, we suggest to etch a thicker wire thinner.

The technique provided a reasonable yield for the CPS device on bottom gates.

4.5. Experimental Setup

The observation of quantum dots requires that the temperature is sufficiently lower than the charging energy E_C , the orbital level spacing δE or the superconducting gap Δ of an attached lead. Most of these energies are in the meV range or lower, so that most of the experiments were done below 1 K.

To cool a sample down to so low temperature can be quite elaborate. That is why we test the NW devices before at room temperature (RT) for leakage currents between the gates themselves and measure 2-terminal device resistances. If the latter is of more than 500 k Ω , it indicates 'bad' ohmic contact formation and often do not conduct at low temperature even at large gate voltages.

Several cryogenic systems are available in our lab to cool the samples down to the required temperatures. They all rely on the light gases ^4He and ^3He or on mixtures of them. A cryostat with the sample inside is usually lowered into a liquefied ^4He bath having a temperature of 4.2 K, the boiling point of ^4He . The simplest cryostat immerses the sample as well into ^4He and keeps it 4.2 K. Such a dipstick is ideal for short tests at low temperature as it can be cooled and warmed up within an hour. Lower temperatures are reached by pumping on the ^4He . The increased evaporation

cools the remaining liquid to a minimal value of 1.2 K where the vapour pressure decreases drastically. The same principle can be used with ^3He , the lighter but rare (and expensive) isotope of helium. Its vapour pressure stays large to lower temperatures and allows to reach 230 mK in our system. In such ^3He cryostats the sample is thermally isolated by a vacuum from the ^4He bath.

Even lower temperatures are reached in dilution refrigerators which rely on a $^4\text{He}/^3\text{He}$ mixture. Below ~ 870 mK the mixture separates into a ^3He -rich and a ^3He -poor phase. The phase transition of ^3He from the rich into the poor phase takes up a certain latent heat which exists down to very low temperatures [124]. By driving the phase transition with a smart pumping scheme, temperatures below 10 mK can be reached. All these cryostat systems are these days commercially available. They also provide large field superconducting magnets to put the sample into a magnetic field. The measurements recorded in Budapest were done in the newly available cryo-free systems which replace the ^4He bath with a (fancy) heat pump.

The chip-carrier holder with the sample is connected by thin wire in twisted pairs to a break-out box at room temperature (RT) and from there with BNC cables to the measurement electronics. Since the electron and phonon temperature decouple at low temperature the phonon bath cannot take up all the heat transported through the measurement lines. Therefore, the lines are well filtered for high frequency radiation and the filters are thermally anchored at low temperature as good as possible. A so-called tape worm filter with cut-off frequency ~ 10 MHz [125] is placed at the entrance to a Faraday cage which encloses the sample and shields it from thermal radiation. Additionally we filter most of the lines at RT with commercial π -filters which have a cut-off at 1 MHz.

Since the measured QDs have usually resistances between 10 k Ω and basically infinite when they are in blockade, we voltage bias the devices and measure the current. The voltage bias consists of a dc part supplied by a *YK7651* (Yokogawa Electronic Corporation, Tokyo, Japan) and an ac part which is provided by a lock-in amplifier (*SR830*, Stanford Research Systems, Sunnyvale, USA) and superimposed with a transformer. The bias is then attenuated to usually 10 μV by a voltage divider just before the break-out box of the cryostat. The ac measurement frequency is chosen at typically $f = 133$ Hz limited by the line capacitances. The current through the device is measured by homebuilt current-to-voltage amplifier (IV-converter) at room temperature. They have a transimpedance of 10^7 V/A and allow changing their offset voltage. The output voltage is fed back to the lock-in amplifier. Thus, the differential conductance $G = dI/dV \approx I_{ac}/V_{ac}$ is usually plotted. Voltages to the gates are applied by a homebuilt 8-channel digital to analog (DAC) voltage source or, if voltages larger than 10 V are needed, by a *YK7651*. The whole measurement instrumentation is controlled via RS232 or GPIB connections by self-written Labview programs on a nearby computer.

5. Tunnel Barrier Formation in InAs Nanowire Quantum Dots

The electrodes of a QD can consist of different normal metals or semiconductors yet even superconductors or ferromagnets. The latter we call *exotic* as well as all other materials with different electron correlation and spin ordering rendering their interaction with quantum dots particularly interesting. Vice versa such bulk correlations are interesting to investigate with a highly tunable single electron system. The electron wave function of a QD adopts the properties of the *exotic* lead as electrons are exchanged through the tunnel barrier. The hybridization strength is determined by the strength of the tunnel barrier between the lead material and the QD. Hence, by tuning the tunnel barrier we can change the properties of the quantum dot. When the barrier is low, the wavefunction of QD and the lead will overlap more and the electrons in the QD will correlate similar to the *exotic* lead.

Different material systems have different advantages for the investigation of these *exotic* couplings. For example, the tunnel barrier can be well tuned and controlled in a lateral 2DEG. However, in these systems, the tunnelling is usually to the surrounding 2DEG what can hardly be replaced into an *exotic*. In contrast, quantum dots formed in CNTs or nanowires are readily connected to superconducting and ferromagnetic materials, but the barrier is more difficult to control. This thesis is focused on the InAs nanowires. Finding ways to achieve tunable tunnel barriers was one of the primary goals of the thesis. Thus, in this chapter devoted to the specific ways of quantum dot formation in InAs nanowires.

The electron wave function in a InAs nanowire with sufficiently small diameter is already confined in two dimensions. By making barriers along the wire confinement in the 3rd dimension is introduced leading to a discrete energy spectrum. Assuming a 3-dimensional particle in a box picture with an electron density of

$$n = \frac{N}{L^3} = \frac{k_F^3}{3\pi^2} \quad (5.1)$$

we can estimate the level spacing

$$\delta E = \left(3\pi^2 N\right)^{-1/3} \frac{\hbar^2 \pi^2}{m^* L^2} \quad (5.2)$$

where k_F is the Fermi wave vector and N the number of electrons in the box [82]. Note that this estimation is only valid for materials with a parabolic dispersion relation and about equal spatial extent in all directions. This is the case for our studied InAs nanowire quantum dots as this chapter will show. Quantum dots with a 2-dimensional

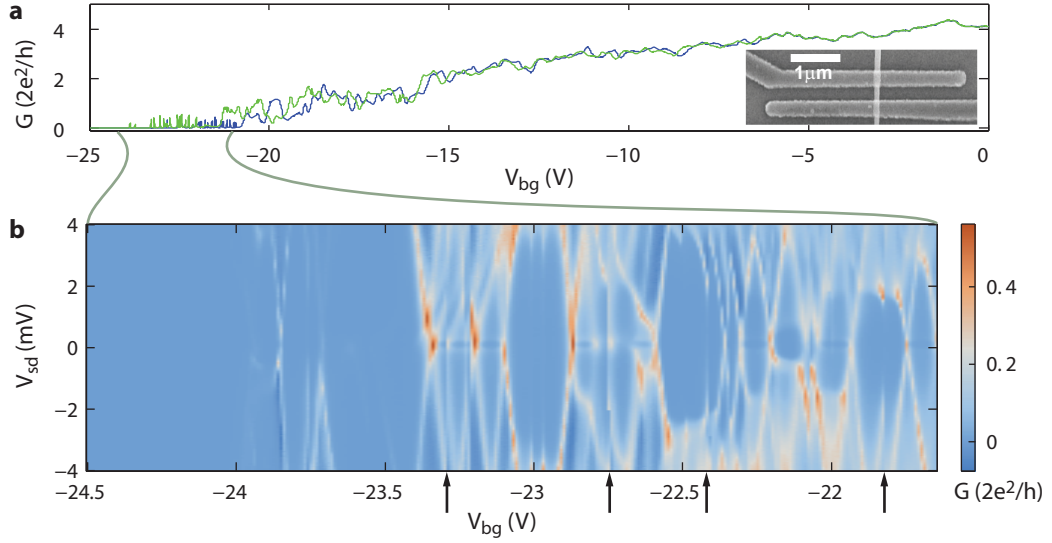


Figure 5.1.: **a** | Differential conductance $G(V_{bg})$ measured through a nanowire from $V_{bg} = 0$ V to $V_{bg} = -25$ V in blue and from $V_{bg} = -25$ V to $V_{bg} = 0$ V in green at 0.3 K. The conductance is hysteretic, indicating the existence of possibly shallow charge traps. At gate voltages $\gtrsim -20$ V contacts are 'open' and universal conductance fluctuations (UCF) are observed. The inset shows an SEM image of the investigated device. **b** | Stability diagram in region of crossover from the strong CB regime to the intermediate regime. The measurement is taken under magnetic field ($B = 0.3$ T) to suppress the superconductivity in the Ti/Al leads.

geometry as in 2DEG will have a different dependence on N . In 1-dimensional CNT quantum dots the level spacing will even have a $1/L$ length scaling due to the linear dispersion relation.

The question arises how to confine the wave function along the wire to induce a quantum dot. We present in the following sections the three possibilities used in this thesis. In a first method, a global potential is applied by backgate to a short piece of nanowire. The second method uses etchants to make constrictions in the nanowire while the third method applies local potential variations by closely spaced gates which are in close proximity to the nanowire.

5.0.1. Quantum Dots induced by global gates

Single electron transport can be observed in nanowires by using the simplest device geometry of two ohmic contacts to a nanowire [126, 127, 128, 86]. Isolated electronic islands are formed at low temperature and low electron density. The barriers to the islands (QDs) are tunable by a potential applied to a global back gate [128]. The main advantage of this technique is that the quantum dots have been shown to couple to superconductors [129] or ferromagnetic leads [130].

Fabrication and measurement follow the methods described in chapter 4. An image

of a typical device is shown in the inset of fig. 5.1a. For an exemplary device, two contacts out of a Ti/Al bilayer¹ are fabricated on a InAs nanowire deposited on 400 nm thick SiO₂ layer. The substrate is highly doped Si that is used as the global back gate.

In fig. 5.1a the conductance in the linear regime is plotted as function of V_{bg} . In the measurement we first deplete the nanowire following the blue curve starting from $V_{bg} = 0$. Subsequently the gate voltage V_{bg} is swept in the other direction and the green conductance curve is obtained. Around zero gate voltage the electron density is large and reproducible universal conductance fluctuations are observed. The sweeps are especially at large negative V_{bg} hysteretic and do not reproduce. We find a shift of the threshold voltage $\Delta V_{\text{thres}} \sim 0.6$ V. Below ~ -20 V the device exhibits Coulomb blockade. This region is more closely investigated by measuring the voltage bias V_{sd} dependence in addition (5.1b). At higher gate voltages, we identify Coulomb blockade in the strong coupling regime, where the peaks are broadened and Kondo features are possibly observed². The Coulomb diamonds have different sizes and irregular shape, suggesting that more than one quantum dot is formed along the wire. Moreover, sudden disruptions are seen at the positions indicated by arrows in fig. 5.1b which we attribute to charge rearrangements in shallow charge traps in the insulators surrounding the nanowire.

The occurrence of charge traps is also consistent with the hysteresis in the large voltage-range gate-sweeps in fig. 5.1a. We presume that shallow traps with binding energy $E_b \sim k_B T$ screen the gate potential on the time scale of the voltage sweep. However the main driving of the charge rearrangement seems to be the large electric potential because towards higher V_{bg} the hysteresis gets smaller and the measurement reproduces around zero gate voltage. The true threshold voltage is therefore believed to be at a higher gate voltage. Nevertheless, the threshold voltage is quite negative indicating a strong doping in the InAs nanowire. Based on experience, the strong doping arises often for Ti/Al contacts as discussed in detail in sec. 2.4.

We turn the attention again to the plot in fig. 5.1(b). Surprisingly, the Coulomb diamonds are shifted to the right with each charge rearrangement, suggesting that the electric potential is reduced in its absolute value. This observation supports the above interpretation of screening of the gate potential by charge traps. The shift is also an indication that the confinement potential is not significantly deformed, but only shifted in potential energy. Hence, we suspect that the charge traps are located further away in the SiO_x layer rather than in the native oxide where they would have more effect on the confinement potential.

On the other hand, localized charges could generate a disorder potential with multiple local minima that are strong enough, to allow for electron island formation inside

¹Al is a superconductor below 1.2K. A proximity effect is usually expected and observed through the thin Ti layer into the nanowire.

²Most likely a few split Kondo resonances are seen in fig. 5.1(b). We discuss the Kondo effect in magnetic field in chapter 6. Around $V_{bg} \sim -23.4$ V the regime changes to weak coupling, i.e. the Coulomb peaks are narrower and conductance goes to zero between them. Fig. 5.1b is recorded at 0.3 T to suppress the superconductivity in the leads.

the nanowire. Although Jespersen *et al.* have reported single dot behaviour [128] they are rarely observed in our samples. A random disorder potential prevents that one can predict size and coupling Γ of the observed quantum dots. Although the coupling regime can usually be changed from strong to weak (Kondo to narrow peak), a local tunability of a single charge state is clearly lacking.

While charge rearrangements are a common phenomena in our group also for people working on CNT devices, other studies find that interfacial traps freeze out at 77 K [71] without commenting on the location of the charge traps. Without analysis, we find an increased frequency of the charge rearrangements at large gate voltage.

In summary, we ascribe the irregular shaped Coulomb diamonds in global gate induced QDs to multiple island formation in the InAs nanowire. Frequent charge rearrangements at large negative gate voltage compromise the stability for the measurements. The location of charge traps as well as the location of the QD barriers remain unclear. Further a local, predictable tunability is absent. Thus, we explored other methods for tunnel barrier fabrications are at defined locations.

5.0.2. Etched Nanowire Quantum Dots

Different publications in the field find a strong decrease of the mobility in InAs nanowires when the wire diameter is reduced below 40 nm [71, 72]. If the diameter would be decreased locally, we suggest that a barrier could form. The mechanism is not fully clear. Either the surface scattering is increased due to the reduced diameter as elaborated in section 2.5 and 2.3, or the nanowire is locally depleted. If depletion is the mechanism, one can imagine a tunability of the barrier strength by local or global gates.

A constriction can be achieved by etching the nanowire locally with a weak piranha solution following references [131, 132]. The acidic solution called piranha is a combination of sulphuric acid (H_2SO_4) and hydrogen peroxide (H_2O_2) in water. It is known for its strongly oxidizing properties and often used in wafer cleaning at high concentrations. Smaller concentrations can be used to etch semiconductors in a controlled way. The native oxide on InAs is dissolved easily and fast in acidic solutions while the oxidation is usually slower. Similarly, InAs nanowires can also be etched with alkaline solutions, e.g. NH_4Sx [133]. The latter is often used in low concentrations for surface passivation leading to a self-terminating process. However, when employed at higher concentrations, InAs is etched at a constant rate giving precise control on the etch depth on the nanometer scale³ In the following, three different etch processes based on piranha NH_4Sx solutions are presented along with a discussion of the resulting structures.

³The precision is given by the liquid handling. However, with etch rates of 5 nm/min (4% solution) the concentration variation of the etch solution rather important.

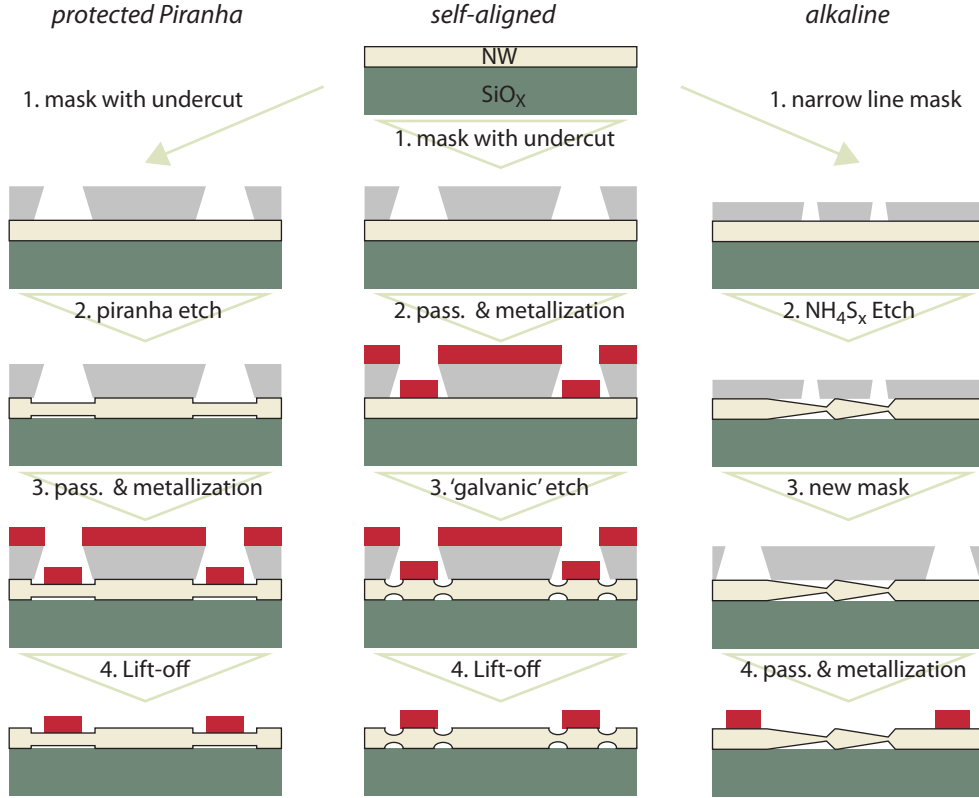


Figure 5.2.: Overview of the etching processes. In the protected Piranha process (1st column) the nanowire is etched before the metallization process and thus thinner on the whole length below the contact. The self-aligned process swaps the etching and metallization step resulting in local constrictions just next to the contact. The best reproducibility is achieved with anisotropic process (3rd column). It uses a second lithography mask that places the metallic contacts further away from the etched constrictions. The details of each process can be found in the text.

Fabrication processes

Figure 5.2 summarizes the different fabrication processes used to fabricate constrictions in nanowires by chemical wet etching. The first column (protected Piranha) illustrates the processes investigated by a former co-worker [120] who found that passivation can inhibit acidic etching what is needed to prevent the otherwise large under etching of the mask. Hence, the nanowires are first deposited on the SiO_x substrate and sulphur passivated⁴. Only after, a PMMA-mask is defined with the help of e-beam lithography. The passivated layer is then locally removed by a short exposure to an oxygen plasma, allowing to etch the nanowire locally with a mild piranha solution in the ratio 100:3:1 $\text{H}_2\text{O}/\text{H}_2\text{SO}_4/\text{H}_2\text{O}_2$. Afterwards, contact fabrication follows

⁴see chapter 4 for more details

in the usual form employing a second passivation treatment. The self-aligned process (column II) reverses the order of acidic etching and contact formation, and was developed in collaboration with G.Fülöp⁵. After evaporation of the metal leads the sample is exposed to oxygen plasma enabling the etchant (Piranha) to attack the semiconductor. The etching occurs in the undercut of lithography mask. That is why a well exposed lithography mask is of importance. This method is called 'self-aligned' etching because no further mask is required to etch the nanowire close to the contact. An SEM picture of a finished device can be found in fig. 5.3b.

The third process does not need a preceding sulphur passivation, but more involved lithography. A 150 nm thick PMMA film is directly applied on the deposited nanowires and exposed with a 30 kV beam. In a cold development step a line width of 40 nm is obtained. Afterwards the nanowires are etched with a 4% sulphur saturated NH_4Sx solution with an etch rate $\sim 5 \text{ nm/min}$. In the end contacts are fabricated the usual way further away from the etched area. Here a SEM picture of a finished device is printed in fig. 5.4a.

Results of the self-aligned method

We found that the etch rate is reproducible when the nanowires are freely lying on the substrate and was sulphur passivated beforehand. when contacted by Ti/Au leads, however, the etch rate increases 10x or more. This reduces etch times to a few seconds, a time scale hard to control precisely by our liquid handling techniques. More diluted and control solutions were employed with the result that H_2O_2 is obsolete for the etching process. Moreover, a sulphuric acid solution with pH 2 is sufficient for the etch process [134].

We believe that the mechanism involves a galvanic cell reaction at the micro scale [135]. While the InAs is continuously oxidized and dissolved by the acidic solution, protons are reduced on the metal surface. Because ohmic contacts were already formed beforehand, the electrons can flow from the InAs NW to the metal surface as illustrated in fig. 5.3a. In this picture the uncontrollable etch rate can be explained by a surface area dependence of the reduction half reaction. However, experiments performed with different metal electrode sizes remained inconclusive. We think that imperfect and variable ohmic contacts could limit the electron current.

The self-aligned method places the leads on unetched part of the nanowire what should give more reliable ohmic contacts due to the larger area. However, we found that the initial well-conducting contacts are degenerated in the etching step and high ohmic devices are obtained. We speculate that the contact is either largely under etched or oxidized. Nonetheless, a working device was obtained which exhibited Coulomb blockade over large gate ranges as shown in fig. 5.3c. The device proved to be very stable and charge rearrangements occurred rarely.

⁵Budapest University of Technology and Economics

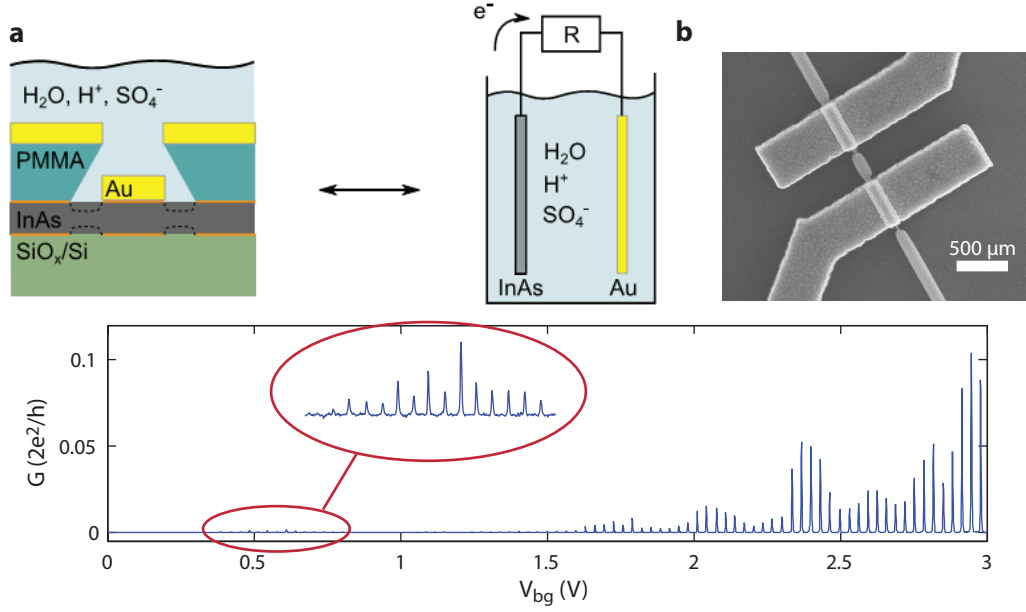


Figure 5.3.: **a** | Schematic cross-section of a 'self-aligned' etched device. Next to it is a schematic for clarification of the galvanic process. InAs is oxidized close to the contact while the reduction reaction happens at the gold surface by formation of molecular hydrogen. Adapted with permission from [134]. **b** | Scanning electron micrograph of the investigated device. **c** | Measured backgate response exhibiting regular Coulomb blockade over large voltage range. The inset expands a low conductance area showing small amplitude Coulomb peaks.

Results of the alkaline etching

Even though etched through the small opening of 40 nm the InAs nanowires are etched up to 400 nm below the PMMA. The etching occurs highly anisotropically along the nanowire axis with a flat and a steep angle to the axis (figs. 5.4a or 5.2). Etching along lattice planes is a common phenomena. Etched constrictions on the same nanowire showed all the same directionality (up to four were fabricated). Further, the narrowest constriction is not at the same place as the mask opening inferred from the resist residues sometimes seen in the SEM image (dashed lines). We attribute the anisotropy to the absence of an inversion symmetry in the hexagonal wz structure and conclude that the nanowires must indeed be stacking-fault free.

The etching is generally very reliable and controllable on the nm scale with etch times longer than 10 min. The etch rate is determined from SEM images by comparing the thinnest constriction size to the original diameter of the nanowire. We find the diameter reduction to be linear with etch time. Doubling concentration of the solution (from 2% to 4% $(NH_4)_2S$) doubles the etch rate. Because multiple wires are processed at the same time the absolute constriction size still varies up to 20 nm from wire to wire but corresponds to the diameter spread of the nanowires. An island structure for a QD can be obtained by opening two lines with a separation larger than 500 nm

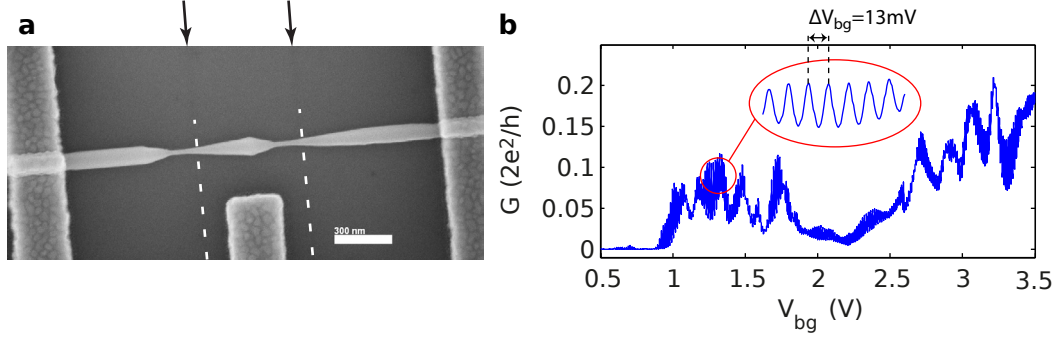


Figure 5.4: **a** | SEM image of the investigated device. **b** | 2-terminal conductance through the wire part as function of the backgate voltage V_{bg} . Regular Oscillations in the whole gate range are observed and made visible by the inset.

in the etching mask. If they are designed more closely, no clear QD structure is found neither in the nanowire nor in the measurement. Instead, multiple dots are induced by the back gate as described in the section above (5.0.1).

In fig. 5.4(b) the conductance as function of the back gate voltage V_{bg} is plotted for a typical device. Very regular Coulomb blockade oscillations are observed over the whole range, indicating that a single QD dominates the transport. The inset points out the observed oscillations which are fully reproducible and not due to noise. The Coulomb peak height in the measurement in fig. 5.4b is modulated within several neighbouring peaks, yet the maximal peak amplitudes are in the whole conductance range between 0 and $0.2 G_0$. A constant charging energy of $E_C \sim 4$ meV is obtained from bias spectroscopy measurements. The lever arm is with $\alpha_{bg} \approx 0.4$ much larger than lever arms of global gate induced quantum dots typically ~ 0.1 . Analysis of the peak spacing shows no 2-fold pattern as expected from a spin filling. Excited states are not observed either which would allow to extract the level spacing in a different way. Thus, we estimate the quantization energy from eq. 5.2 and obtain values in the single digit μeV range much smaller than the temperature of this measurement (4 K). A size of $L = 120$ nm and electron number of $N = 50$ was assumed⁶.

We argue now why we think the QD is indeed formed between the two etched constrictions. The unusual large lever arm is an indication the quantum dot is most likely far away from any large metal electrodes screening the gate potential. The not resolvable level spacing in the measurement is in agreement its estimation for the size etched island. Therefore the QD is large and more similar to a single electron transistor (SET).

We attribute the modulation of the peak height to mesoscopic fluctuations. Inside QDs the latter are usually treated theoretically with random matrix theory (RMT) with the main publications in the 1990ties, [82, 136]. However the nearest neighbour peak positions are uncorrelated in this theory. Also semi-classical theories were pub-

⁶Although the electrons can in principle be counted in the measurement, we don't think that the we see the first electron in the QD. The conductance is pinched off before.

lished explaining the correlation between the peaks by classical periodic orbits [137]. Both approaches assume the full quantum regime where $\delta E \gg k_B T$ what is not the case for the presented QD in fig. 5.4. Still, an intuitive picture can be gained from them and is given in the following since the regime $\delta E \gg k_B T$ applies in other QDs measured in this thesis. An irregular shape of a QD gives rise to chaotic scattering from its boundaries. Therefore, the spatial structure of the wave function varies in a chaotic way upon application of external fields. In particular, the amplitude of the wave function in the vicinity of the tunnel barrier determines the coupling of the QD to its leads. Thus, different orbitals lead to a random peak amplitudes.

Quantum interference effects known as universal conductance fluctuations (UCF) depend on potential variations and are usually observed in transparent devices (large coupling to the leads). In the here discussed device the leads are not directly metallic reservoirs but multi-mode nanowires which are known to exhibit UCF [66]. It is easy to imagine that the effective coupling depends on the interference effects at the tunnel barrier. This would also explain the variation of the peak height as well as the correlation between neighbouring peaks, since UCF have usually a weaker gate dependence than the Coulomb blockade oscillations.

Figure 5.5 shows the results from a second device. The QD stability diagram in fig. 5.5(a) is as well over large ranges regular. The charging energy is varying around 3 meV, but no orbital level structure is observed. Peak amplitudes are fluctuating, too, as discussed above. The general characteristics are very similar to the first device in fig. 5.4 demonstrating the reproducibility of the method. As described in section 3.1.2, the coupling strength of the quantum dot can be obtained from the FWHM of a Coulomb resonance in the strong coupling regime ($k_B T \ll h\Gamma$). Figure 5.5(b) shows the FWHM of several neighbouring peaks as function of temperature. At low temperature the points approach a constant value independent of temperature as expected for life-time broadened resonances. A minimal coupling of $h\Gamma = 280 \mu\text{eV}$ is obtained with the narrowest points of constrictions in the etched structure being 49 nm.

Peak height variations not only occur by sweeping the gate voltage but when applying an external magnetic field [82, 138]. The measurement involves a two-dimensional raster since not only the height but also the peak position depends on the magnetic field (see section 3.1.4). Here we plot the data of four distinct peaks (fig. 5.5c) to illustrate the variability which cannot be neglected when applying large magnetic fields. The conductance can even be suppressed completely.

Summary

We have shown that quantum dots can be formed by diameter constrictions in InAs nanowires using different etching recipes. While acidic etching has a rather low device yield, the alkaline method is quite promising yielding stable quantum dots. We are not aware of any other publications reporting the usage of NH_4Sx based solution to etch constriction into nanowires. The method has some restriction as rather large quantum dots have to be formed to fulfil the needed geometry for island structuring.

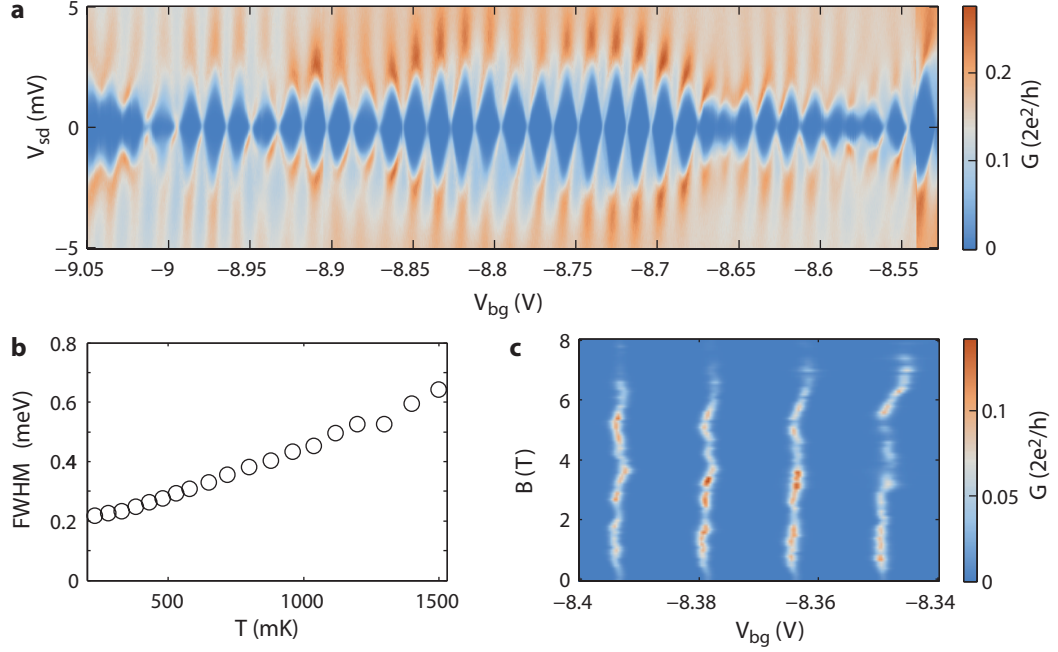


Figure 5.5.: Measurement results of a second device etched by the alkaline method (process III in fig. 5.2). **a** | Stability diagram of the device showing mostly regular diamonds, thus indicating the formation of only a single QD ($T=230$ mK) **b** | Extracted FWHM of several peaks as function of temperature. At low temperatures the strong coupling limit ($\hbar\Gamma \gg k_B T$) is reached leading to a saturation of the broadening. **c** | Magnetic field evolution of four neighbouring resonances. Mesoscopic fluctuations change the amplitude drastically even to full suppression at very high fields.

Moreover, these QDs were so far only coupled to nanowire parts and not directly to metallic leads.

The coupling strength $\Gamma \approx 200 \mu\text{eV}$ is still larger than the superconducting gap Δ of aluminium. As will be described in sec. 3.4, a smaller Γ would be advantageous for the proposed quantum devices, e.g. Cooper-pair splitters and Majorana Fermion state devices. We are confident that the coupling strength could be decreased by further reducing the constriction diameter. Structures with constriction sizes of 20 nm were fabricated already but unfortunately, those were destroyed by electrostatic discharges (ESD). In order to prove that the coupling Γ depends really on the radial constriction diameter, further studies would be needed. In principle, one could also think of combining this technique with a local gate structure similar to the one which is presented in the next section in order to tune the coupling.

5.0.3. Bottom gate induced quantum dots

In this section we use narrow gates below insulating layers to locally deplete the nanowire and thereby induce tunnel barriers. Different research groups have already employed local gates for this purpose [122, 139, 140]. Top gates are the most straightforward method for this purpose and promise the best tunability. Thin metal strips are evaporated on top of the semiconducting nanowires (NW), insulated either by the native InAs oxide on the NW or by an additional oxide layer grown by atomic layer deposition (ALD). The approach was tried in house [141], but we find that top gates on the native oxide render the devices unstable in agreement with other groups⁷. Trapped charges in the oxide rearrange frequently. Therefore that route was abandoned.

A second option is to fabricate local gates separately and cover them with an insulator before nanowires are placed on top. The expected lever arm is expected to be smaller due to geometry but similar values have been reported [140]. The fabrication of such bottom gates is described in section 4.3 of this thesis. Here the measurements of a typical device are presented and the induced tunnel barriers are discussed.

Quantum Dot characterization

The device discussed here as an example had two titanium / gold contacts at a distance of $1 \mu\text{m}$. Ten bottom gates between these contacts were connected but only the first eight from the source lead successfully. A schematic of the device can be found in fig. 5.6a. The field-effect response of the device is first characterized for each bottom gate (fg1-fg8) separately. At room temperature the local bottom gates cannot suppress the conductance completely. This absence of a sharp pinch-off voltage at room temperature is explained differently in literature. Nyård *et al.* measured the conductance as function temperature and gate voltage and found that the temperature

⁷Private communications with the groups of K. Ensslin (ETH Zurich), L. Kouwenhoven (TU Delft) and H. Xu (Lund University)

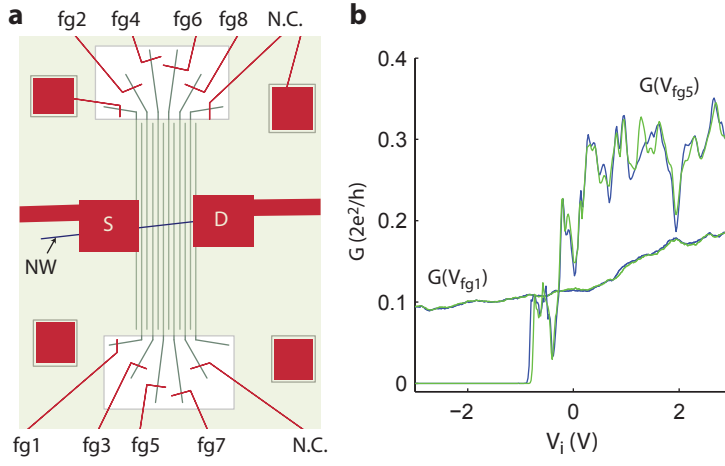


Figure 5.6.: **a** | Schematics of the presented bottom gated device. Quantum dots can be formed by applying negative voltages to the finger gates (fg1-fg8) to induce tunnel barriers in the nanowire (NW). **b** | Conductance G as function of at 4 K

activated transport is in agreement with the Boltzmann distribution, implying the existence of barriers which are overcome with temperature activation [140]. On the other hand, Javey *et al.* employed C-V measurement to characterize interfacial charge traps and found them freezing out around 100 K [71]. Moreover, their surface passivation technique yields devices with threshold voltages independent of temperature [49] indicating the reduction of trapped charges.

Figure 5.6b shows two typical measurements of the 2-terminal conductance through the device as function of a bottom gate voltage at 4 K. The blue and green curves are the down and up sweep, respectively. Gate fg5 shows a threshold voltage of $V_{fg5} \sim 0.9$ V while fg1 tunes the electron density only little and shows no pinch-off. The threshold voltage of other bottom gates are also varying but on average ~ 1.5 V, yet threshold voltages near zero or positive are also observed. We find that bottom gates in the vicinity of the contacts, e.g. gate fg1, have a lower lever arm and rarely deplete within the investigated voltage range. These bottom gates close a contact seemed to be screened either by the metal electrode nearby or by a locally larger electron density in the nanowire. The latter can originate from induced surface states by the metal (see section 2.4). Dahl Nissen *et al.* speculates that positive threshold voltages originate from imperfect contact processing [140].

We use the threshold voltage as guide value for the induction of local barriers in the nanowire. Figure 5.7a shows a charge stability diagram of a QD formed with three bottom gates next to each other. On the outer two gates (fg3, fg5), negative voltages close to the threshold were applied, inducing two barriers in the NW, while the remaining gates were kept at constant positive voltage including the central gate (fg4). The latter was also used to tune μ_i of the QD and therefore called tuning gate. The gates with negative voltages are from here on referred as barrier gates, although they also tune μ_i with a certain lever arm. Vice versa the induced tunnel barriers are not independent of the tuning gate. Fig. 5.7b shows a measurement of a differently formed QD and should illustrate that the function of the individual bottom gate (barrier/tuning) can be swapped. In this second gate configuration, we

use five bottom gates next to each other on the same NW segment to form a larger QD. Gates fg3 and fg7 are used as barrier gates and fg4, fg5 and fg6 as tuning gates, i.e. they had a positive voltage applied to them. As expected for a larger QD we find a smaller charging energy of 3 meV. As expected, E_C and the orbital level spacing δE

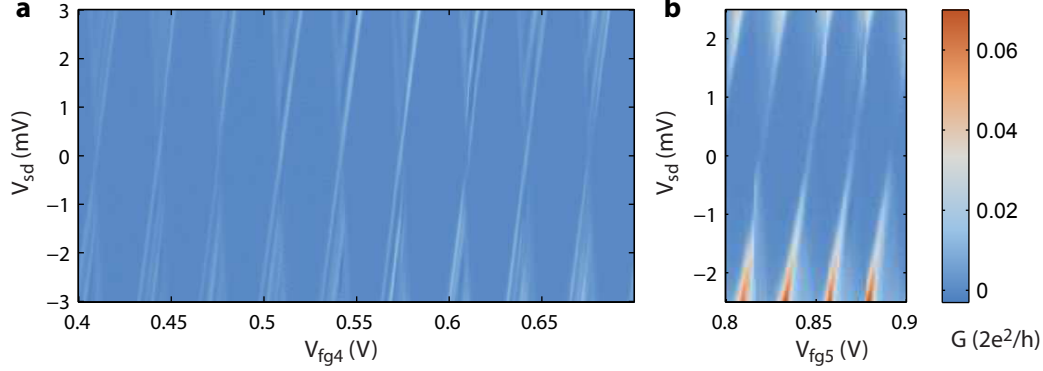


Figure 5.7.: **a** Differential conductance versus source-drain bias V_{sd} and tuning gate voltage V_{fg4} of a quantum dot defined by three adjacent bottom gates on an InAs nanowire. The middle gate is the tuning gate of the dot, while the other two gates are kept a negative potential inducing two barriers in the NW. **b** Same measurement as in **a** of a QD formed using five neighbouring bottom gates, where the three inner ones define the QD.

(not resolved in fig. 5.7b) are decreased with the QD size.

We first argue how to extract the QD position. First, a single QD dominates the charge transport through the wire over large gate ranges as shown in fig. 5.7a. There are no multiple dot structures observed as in the case of global gate induced QDs (fig. 5.1b in sec. 5.0.1) which would indicate a random formation of quantum dots. Second, the gates not used for the QD formation also couple to the quantum dot capacitively. The capacitive coupling strength, i.e. lever arm, depends on the distance to the QD. We can extract the ratio of the lever arms of two gates in conductance measurement as function of both gates. A typical measurement is plotted in the inset of fig. 5.8b. The results are summarized in table 5.1 for a QD induced with gates fg4 and fg6 (barrier gates), where fg5 is the tuning gate. The lever arms become smaller away from fg5, which is consistent with the QD formed above fg5. Thus, we are confident that quantum dots are where they supposedly are.

Gate	fg1	fg2	fg3	fg4	fg5	fg6	fg7	fg8
ratio to gate fg5	-	0.02	~ 0.07	0.4	1	0.34	0.05	0.045
lever arm	-	0.004	0.015	0.088	0.22	0.075	0.011	0.010

Table 5.1.: Lever arm study of the quantum dot formed between gate fg4 and fg6. The barrier gates have already significant smaller lever arm to the quantum tuned with plunger gate fg5.

Double quantum dots are easily induced as well, e.g, from the QD formed with five gates and lowering the central gate voltage, thereby inducing an additional barrier and dividing the larger QD in two. QDs formed in this manner have good stability, i.e very few charge rearrangements happen. We conclude that SiN_x is a good gate insulator. In addition, the bottom gates screen the back gate nearly completely (very small lever arm) and therefore all the charge rearrangements that could occur in the SiO_2 gate dielectric as well.

Barrier tuning

Tunability of the tunnel barriers is shown directly by the change of the tunnel coupling $\Gamma = \Gamma_S + \Gamma_D$ which is at the same time the width of the Coulomb resonance at low enough temperatures (see sec. 3.1.2). To demonstrate tuning of Γ_S and Γ_D , a quantum dot is formed with gates fg4, fg5 and fg6. Fig. 5.8a shows four Coulomb resonances tuned by the tuning gate voltage V_{fg5} . As the barrier potential (V_{fg4}) is tuned to change Γ , the resonances shift also along the V_{fg5} axis due to the capacitive coupling. They are fitted by a Lorentzian (eq. 3.4) and the coupling is obtained using the known lever arm extracted from a single Coulomb diamond. Additionally, the width of the resonances can be extracted when fitted to eq. 3.5, i.e. the temperature broadened limit. The results are shown for a single resonance in fig. 5.8b in green

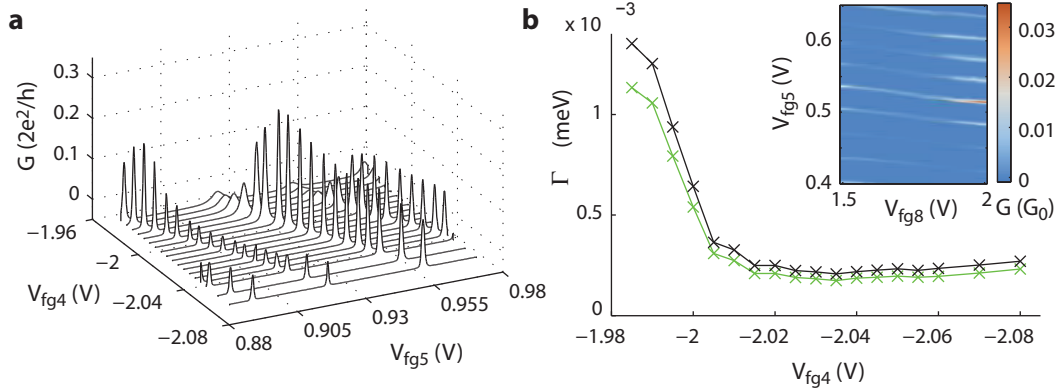


Figure 5.8.: **a** | Waterfall plot of G as function of the tuning gate at different barrier gate voltages. **b** | Extracted lifetime broadening Γ by of the central resonance in a. The fit by a Lorentzian (green) yields better congruence at large coupling values, while eq. 3.5 fits better to the smaller couplings. The inset shows a similar measurement as in (a) but instead of the barrier gate voltage the potential of a dégaagé gate (V_{fg8}) is changed.

(Lorentzian) and black (eq. 3.5). Γ varies from 1 meV to a saturation of $\Gamma = 200 \mu\text{eV}$. At the saturation value the Beenakker line shape (3.5) fits better indicating that the width is limited by the temperature, although the corresponding temperature of $T = 650 \text{ mK}$ is quite large compared to the base temperature of the cryostat ($T_{\text{base}} = 230 \text{ mK}$).

In general, the change of Γ is not monotonous with gate voltage although a trend is

followed from the open dot regime to the pinch-off voltage. The barrier gate voltage changes not only the tunnel barrier, but also the confinement potential of the QD. Thereby the wave function overlap with the leads is changed. In addition, we suspect that the coupling can also be tuned by interferences in the nanowire lead. The inset of figure 5.8b shows the conductance through the quantum dot as function of the tuning gate (V_{fg5}) and a remote gate (V_{fg8}). On the large gate range the width and height of the Coulomb peaks are varied. Such effect are even present in most clean CNT devices [22]. Therefore, a straight forward monotonous Γ -tuning can be only found on small gate voltage intervals.

Γ_1 and Γ_2 can be extracted from the peak height and width of a lifetime broadened resonance, but an assignment of the values to the specific lead is not possible to our knowledge. However, the assignment is important in view of the CPS devices where we would like to know if $\Gamma_N > \Gamma_S$ or not. A possible route discussed during this thesis is to assign Γ_1 and Γ_2 from bias spectroscopy measurements. The observed Coulomb diamonds have often asymmetric shape, an effect explained in sec. 3.1.3 by the capacitances of lead 1 and 2. The Coulomb diamonds often exhibit either a weak drain or the source resonance slope, e.g. as in the measurement in fig. 5.7b or fig. 5.9c. We model the measurement in fig. 5.9c with the single level model by Beenakker [84] who gives for the current

$$I = -\frac{|e|}{h} \frac{\Gamma_1 \Gamma_2}{\Gamma_1 + \Gamma_2} [f_1(\mu_N) - f_2(\mu_N)]. \quad (5.3)$$

Expressions $\mu_N = -|e|\alpha_S V_{sd} - |e|\alpha_g V_g$, $\mu_1 = -|e|V_{sd}$ and $\mu_2 = 0$ are used for the chemical potentials giving an asymmetric biasing as in the experiment [47]. The source lever arm is obtained from the Coulomb diamond slopes in the measurement $\alpha_S = \frac{m_+}{|m_+| + |m_-|}$ (sec. 3.1.3). Temperature and the couplings are adapted to the conductance. The calculated current is shown in fig. 5.9a. It has a plateau at large

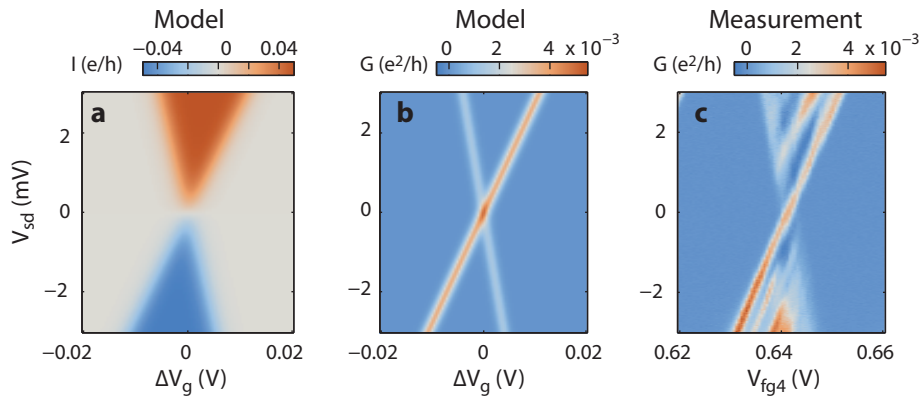


Figure 5.9.: **a** | Calculated current of a single level connected to metallic leads according to eq. 5.3 as function of a gate and bias voltage. **b** | Differential conductance obtained from a. **c** | G from an example measurement. The conductance of negative diamond slope is reduced compared to the other slope.

bias voltages and when a level is inside the bias window seen as dark blue and red regions. In order to obtain the differential conductance the current is derived in y -direction corresponding to the ac-bias from the measurement setup (sec. 4.5). The rise of the current along the positive diamond slope is steeper leading to a larger differential conductance (fig. 5.9b). The ground state resonances in fig. 5.9c) are well reproduced. We note that if the source lever arm α_S is set to 0.5, symmetric diamonds and equal differential conductance along the slopes is obtained. From this discussion we conclude that the change in current perpendicular to the resonance line is given by the Fermi functions, but along V_{sd} it depends on the slope, i.e. on the capacitive couplings. Γ_1 and Γ_2 are not in this picture. Γ_S and Γ_D could lift the symmetry when higher order processes, relaxation or excited states are considered in more advanced models.

5.1. Summary

Different approaches for quantum dot formation in InAs nanowires have been investigated with emphasis on the tunability of the tunnel barriers. The conventional global back gate induced quantum dots are prone to formation of multiple quantum dot. Also they lack the tunability of a single charge state completely. The second conventional approach employs local gate structures. While top gates proved rather unstable, bottom gates are much more promising. They provide good stability and good tunability if located not too closely to a metal lead. Monotonous control of the tunnel coupling is only achieved over small gate voltage ranges. Last an effort was made to establish quantum dots formed by etched constrictions in the nanowire. Most stable and regular Coulomb blockade were obtained. If combined with a local gate structure this could improve tunability further.

6. g -factor Anisotropy in InAs Nanowires

The electron g -factor in semiconductor quantum dots (QDs) plays an important role in modern concepts of spintronics and spin-based quantum computation. A tunable g -factor is crucial for addressing single spin qubits in an array [10]. Even though the manipulation and control of a spin Qbit has been shown in InAs nanowire double quantum dot [142], precise knowledge of the g -factor is still important.

There exist different possibilities for the determination of the g -factor. Within electron transport studies, the earliest methods used for InAs QDs is excited state spectroscopy [143]. Other studies in few electron QDs rely on the shift of electrochemical potential visible in a simple gate voltage sweep [144, 145]. However, the excited states and the Coulomb resonances might not always be that well resolved especially for large and well coupled quantum dots. The Kondo effect provides another tool to measure the g -factor in QDs. The method is not new [86] but has only lately been used in extensive study of the g -factor anisotropy [146]. Nilsson *et al.* compared all the above three mentioned methods on a single state and found no discrepancy [140]. In addition, optical studies on single QDs exist [147].

In this work, we measure the g -factor anisotropy with help of the Kondo effect and from the shift of the electrochemical potential and focus on the dependence of g -factor on the NW orientation with respect to the applied external magnetic field. Moreover, this chapter provides results that show that the Kondo resonance splitting can exhibit different characteristics, depending on the angle of the external field. The measurement results have also been published elsewhere in similar form [148]. Coworker G. Fábíán helped with sample fabrication and data analysis and co-worker A. Baumgartner with analysis and writing.

6.1. g -factor Anisotropy

Spin degeneracy of an orbital level in a quantum dot is lifted by application of an external field and the level will separate linearly with field according to $\Delta E_{Z,N} = g_N^* \mu_B B$. The spin-flip processes giving rise to the Kondo effect (sec. 3.2) become inelastic with energy E_Z leading to a splitting of the Kondo resonance $\delta = 2E_Z$ which is in good approximation larger by a factor of 2 than the Zeeman energy E_Z . In contrast, the electrochemical potential in the linear conductance regime shifts only by half the Zeeman energy $\Delta V = 1/2 g^* \mu_B B / e\alpha$, where ΔV is the shift in gate voltage and α is the lever arm of the gate. In general g^* is anisotropic and well described by a second order tensor

$$g(\mathbf{B}) = \frac{1}{|\mathbf{B}|} \sqrt{g_1^2 B_1^2 + g_2^2 B_2^2 + g_3^2 B_3^2} \quad (6.1)$$

where g_1 , g_2 and g_3 are the g values along the principle axes of the tensor and B_1 , B_2 , B_3 are the components of the magnetic field vector \mathbf{B} . The origin of the large g -factor in InAs is the significant spin-orbit interaction (SOI) which couples the spin and orbital angular momentum. The SOI depends on the precise nature of the wave function which in return depends on the exact shape of the confinement potential. Theoretical studies investigated the g -factor anisotropy disk-shaped QDs [89, 149] and pyramidal QDs [150]. If the dot size is estimated by the full lead spacing (< 250 nm) and the nanowire diameter (~ 100 nm) a small anisotropy is expected because the confinement potential perpendicular to the NW is slightly larger. Since the magnetic field probes angular momentum perpendicular to the field, the g -factor along the NW is expected to be reduced.

A typical device is shown in fig. 6.1: the InAs nanowire is connected to two Ti(5 nm)/Al(100 nm) superconducting contacts ~ 250 nm apart. As back gate serves a highly doped Si substrate which is separated by 400 nm SiO₂. More details about fabrication and measurements can be found in sections 4.1 and 4.5. The sample is

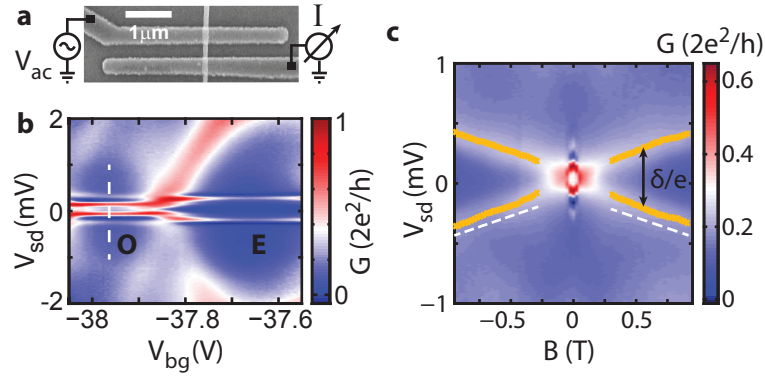


Figure 6.1.: **a** | SEM image a device and simplified schematic of the measurement setup. **b** | Differential conductance G as a function of the backgate (V_{bg}) and the bias voltage (V_{sd}). The dashed line indicates the gate voltage of the measurement in figure (c). **c** | G vs. V_{SD} and magnetic field B at angles $\varphi_1 = -25^\circ$ and $\theta = 72^\circ$. Yellow crosses indicate the extracted peak positions of the split Kondo resonance.

loaded into a dilution refrigerator at ~ 60 mK base temperature. A 2-axis vector magnet and the rotatable insert allows us to apply an external magnetic field \mathbf{B} in any direction relative to the NW axis.

In fig. 6.1b, the conductance G is plotted as a function of V_{bg} and V_{sd} . A magnetic field of $B = 200$ mT suppresses the superconductivity (not shown) which allows us to identify a Kondo resonance in the odd charge state labelled "O". The corresponding features in the superconducting state in fig. 6.1b are consistent with Kondo modulated Andreev transport discussed in ref. [151, 152]. Here we focus on the splitting δ of the Kondo resonance in an external magnetic field. In fig. 1c, G is plotted as a function of B and V_{sd} for $V_{bg} = -37.95$ V (dashed line in fig. 6.1b). At low fields the

contacts are superconducting and the field evolution of G is given by the suppression of the superconductivity. At $B > 150$ mT the superconductor is in the normal state and a clear Kondo resonance develops, which splits linearly with increasing field B . We use the position of the peak maximum (marked yellow) to measure the energy splitting δ , from which we extract the effective g -factor g^* using eq. 3.8. Linear fits for $250 \text{ mT} < B < 500 \text{ mT}$ improve the accuracy of the results. We repeat such measurements and the procedure for different directions of the magnetic field.

In our coordinate system the substrate plane is in the xz -plane. Since the nanowire was placed by liquid deposition it lies in an arbitrary angle $\theta_{\text{NW}} = 47^\circ$. The direction of the magnetic field is described by the two angles θ and φ where θ is the polar angle from the z -axis and φ the azimuth. The arrangement is illustrated in fig. 6.2a. The nanowire position is marked by black line in the grey $\varphi = 0^\circ$ plane. Two measurement

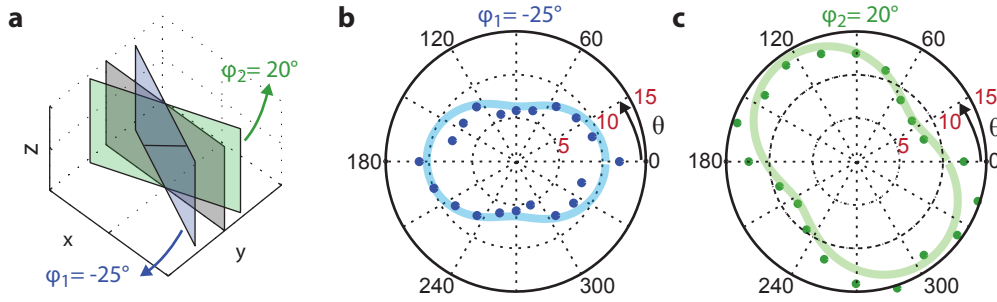


Figure 6.2.: **a** | The defined coordinate system for the experiment. The nanowire lies in the xz -plane (grey). **b and c** | g -factor extracted from the Kondo splitting s as a function of the polar angle θ at the settings $\varphi_1 = -25^\circ$ and $\varphi_2 = +20^\circ$, respectively. The radial position corresponds to the value of the g -factor. The continuous curves stem from the fit explained in the text.

series were performed at fixed azimuths $\varphi_1 = -25^\circ$ and $\varphi_2 = 20^\circ$, while the polar angle θ is varied. The resulting g^* values in the two planes are plotted as dots in figs. 6.2b and 6.2c.

The g -factor is found to be anisotropic. It takes a minimal value of $|g_{\min}| = 5.2$ at $\theta = 288^\circ$ and $\varphi = 25^\circ$ for the extracted values. The maximal measured value $|g_{\max}| = 15.3$ at $\theta = 288^\circ$ and $\varphi = 20^\circ$ exceeds the bulk value only slightly. The data is fitted to eq. 6.1. by rotation of the tensor in the coordinate system. The fit parameters are the principle g -factors g_i and the Euler angles of the rotation. The results are shown as pale curves in fig. 6.2. The fit is in good agreement with the data for g_i between 5 and 15.

In a similar way, we extract the g -tensor from gate dependent measurement in the linear conductance regime. Figure 6.3a shows a single resonance from a *different* charge state than above as function of gate voltage and magnetic field. The superconducting gap suppresses the conductance at low magnetic fields. As soon as the superconductivity has vanished we extract the peak position (marked yellow in the

figure) and perform a linear regression on the points. The g value is obtained from the fitted slope. The lever arm needed for the energy conversion is extracted from bias spectroscopy measurements (not shown).

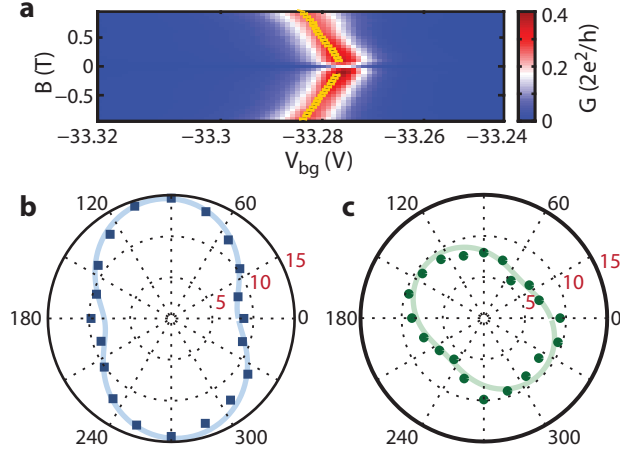


Figure 6.3.: g -factor extraction from the Zeeman shift of a Coulomb blockade resonance. **a** | Differential conductance of a single QD resonance as function of back gate voltage V_{bg} and magnetic field B . Yellow crosses indicate again the peak position. **b and c** | g -factor extracted from the slope of peak shift in (a) as function of the magnetic field direction θ at the same settings φ_1 (blue) and φ_2 (green) as in fig. 6.2

The measurement and extraction procedure is repeated for the same angles of the magnetic field as in the Kondo study above (fig. 6.2). The data points for the two azimuths φ_1 and φ_2 are plotted in fig. 6.3b and c. A g -tensor is again fitted to the points and shown as light curves. The obtained maximal $|g_{max}| = 14.6$ and minimal values $|g_{min}| = 5.63$ are only in a marginally smaller range than the values extracted by help of the Kondo effect. Precisely because the anisotropy is completely different in this charge state, we assess that the principal axes of g tensor not congruent with the principal axes of the nanowire and anisotropy is basically random.

Discussion

In the following the obtained values and anisotropies are discussed. In contrast to previous work [86, 87], we do not observe g -factors significantly larger than the bulk value ($|g^*| = 14.7$). The one value observed to be larger than the bulk value lies within the error range of the linear fit. The latter might be further compromised by anomalies in the Kondo splitting which are separately discussed in the next section. On the other hand, the values from the gate dependent study might suffer from inaccuracies of the lever arm extraction. In addition, we cannot observe the spin pair at smaller occupation number because of charge instabilities. Therefore, additional shifts of higher order in B cannot be excluded.

Björk *et al.* studied g -factors in InAs QD with fixed size [143]. Two InP tunnel barriers defined a quantum well inside a InAs nanowire. Its depth was varied by the growth process. In agreement with corresponding calculations [89] it could be shown that only sizes below 20 nm would reduce g -factor down to values of 5. Moreover, theoretical studies of InAs QDs found that the quenching of the angular momentum should be negligible for crystals exceeding 50 nm [88]. This is an indication that our induced quantum dot is not spanning the whole distance between the leads. Note that the calculations are mainly valid for the zb crystal structure, yet our nanowires are grown in the wz phase and theoretical g -factor calculations are rare [149]. The larger band gap of the wz phase could be indication of a smaller g -factor.

Takahashi *et al.* has shown that even in highly symmetric pyramidal self assembled QDs the spin-orbit interaction can deviate from principal axes just by the presence of the lead electrodes [153]. In a later study, the same authors could conclude the same by measurement of the g -factor [146]. Small changes in the confinement potential will therefore change the anisotropy of SOI and g -factor. Other groups showed that the g -factor is tunable with electric field applied by a side or bottom gate [87, 145]. Early studies of the g -factor in metallic QD found level-dependent and anisotropic g -factors [154]. In this case the anisotropy is ascribed to mesoscopic fluctuations of the SOI. Therefore, we found support for the conclusion in section 5.0.1 and the one from previous work in our group [86] that the gate induced quantum dots states are largely defined by mesoscopic details.

6.2. Anomalies of Kondo effect in magnetic field

In our experiments, we find rather different field evolution characteristics of the Kondo splitting for different field orientations. Figure 6.4 shows three examples in addition to fig. 6.1c. For $(\varphi_1, \theta = 0, g^* \approx 12)$ in Fig. 6.4a the splitting is linear in B , but with an offset of $\Delta B \approx 150$ mT, while for $(\varphi_1, \theta = -72^\circ, g^* \approx 5.5)$ in fig. 6.4b the evolution is not linear in B . For $(\varphi_2, \theta = 72^\circ, g^* \approx 11)$ in fig. 6.4c the amplitudes of the two split Kondo resonances do not evolve monotonously with B and are not symmetric with respect to $V_{SD} = 0$. We find no relation between these characteristics and the extracted g -factor.

We tentatively attribute these observations to a modification of the Kondo state by another transport process becoming available at finite bias. One possibility is that the Zeeman split level starts to cross the next orbital. Spin-orbit interaction would cause an anti-crossing of the two levels [79], but change the spin considerably. Probably this would interfere with the spin-flip processes generating the Kondo effect. Another possibility is that inelastic processes start contributing to the formation of the spin-dependent resonance, which might also account for the bias-asymmetry in asymmetrically biased samples.

The low-field offset of the Kondo splitting is in agreement with the theory. Moore and Wen [155] predict that $\delta < 2|g^*|\mu_B B$ for all B fields, however experimental evidence points to the opposite. For example, Kogan *et al.* find the Kondo splitting

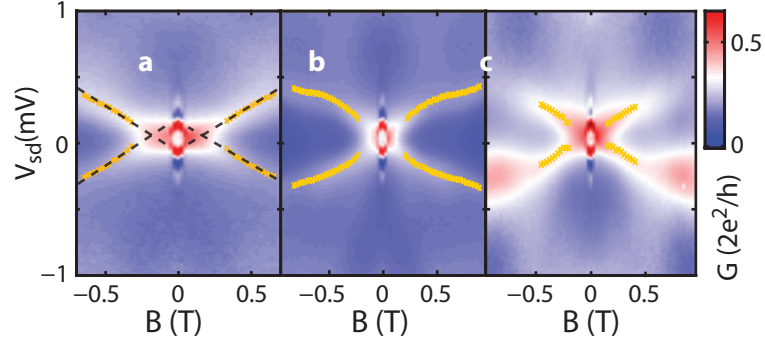


Figure 6.4.: G as function of V_{SD} and B showing a qualitatively different evolutions of the Kondo resonance. **a** | The Kondo splitting s is linear in B with an offset of $\Delta B \approx 150$ mT ($\varphi_1, \theta = 0^\circ$). **b** | The splitting is non-linear in B ($\varphi_1, \theta = -72^\circ$). **c** | The peak conductances are strongly varying and are asymmetric in V_{SD} ($\varphi_2, \theta = 72^\circ$).

to be larger than expected from eq. 3.8 [156]. We have no explanation why the offset should be direction-dependent.

6.3. Summary

We could extract the g -factor anisotropy in stacking fault free InAs NW QDs. The angle dependence in a magnetic field is mapped either by measuring the splitting of a Kondo resonance or the electrochemical potential shift in gate voltage. We find random orientation of the principal axes of the g tensor compared to the nanowire orientation. Mesoscopic fluctuations not only vary the g -factor for each QD level, but also alter as well the anisotropy of g -factor in a random way due to different orbital angular momentum and spin-orbit contributions. In addition, we document different splitting characteristics of the Kondo resonance in the external field.

7. Tunable Cooper Pair Splitters

In this chapter we present experimental result from gate tunable Cooper pair splitter (CPS) based on a InAs nanowire. By simultaneous charge transport measurement in both normal leads of the CPS, we identify correlated currents similar to earlier reported experiments [16, 17, 113, 18, 19] opening up the possibility for entanglement detection between spatially separated electrons. In most of these earlier devices the tunnel coupling between the QDs and the electrical contacts could not be controlled in-situ, but were determined by the fabrication process. Here we report experiments on a CPS device based on an InAs nanowire (NW) with a global back gate and ten local gates, by which the QDs are formed and gated electrostatically. We find a strong dependence of the measured non-local signals on the gate configurations, thereby shedding light on the electron dynamics in such systems. In particular, we tune the barriers on the normal (section 7.2) and the superconductor side (section 7.3) of the QDs, as well as the inter-dot coupling between the dots (section 7.4), each inducing a transition from positive to negative correlations between the non-local signals. Our results are a first step towards controlling and maximizing the CPS efficiency required to detect prospective electron entanglement [15].

The presented work is a close collaboration between the research groups of S.Csonka¹ and C. Schönenberger². Sample fabrications was performed by the author and the measurements were carried out in Budapest by G.Fülöp and the author. Text and graphics follow a manuscript prepared together with G.Fülöp and A.Baumgartner for publication in a peer-reviewed journal.

7.1. Sample fabrication and characterization

An artificially coloured SEM image of a sample is shown on fig. 7.1a. First, using electron-beam lithography, an array of ten local gates was fabricated on a highly doped silicon substrate that serves as a global backgate, insulated by ~ 400 nm SiO_2 . The local gates consist of 4 nm Ti and 18 nm Pt and are ~ 40 nm wide with an edge to edge separation of ~ 60 nm. These gates are overgrown by ~ 25 nm SiN_x for electrical insulation using plasma-enhanced chemical vapor deposition (PECVD). The SiN_x was removed at the edges of the gate array by a reactive ion etch (RIE) with CHF_3/O_2 [118] to fabricate electrical contacts to the local gates. In the next step we deposit a single InAs NW (~ 70 nm diameter) perpendicular to the gates using micromanipulators. The 330 nm wide and 40 nm thick superconducting Nb source

¹Budapest University of Technology and Economics, Hungary

²University of Basel, Switzerland

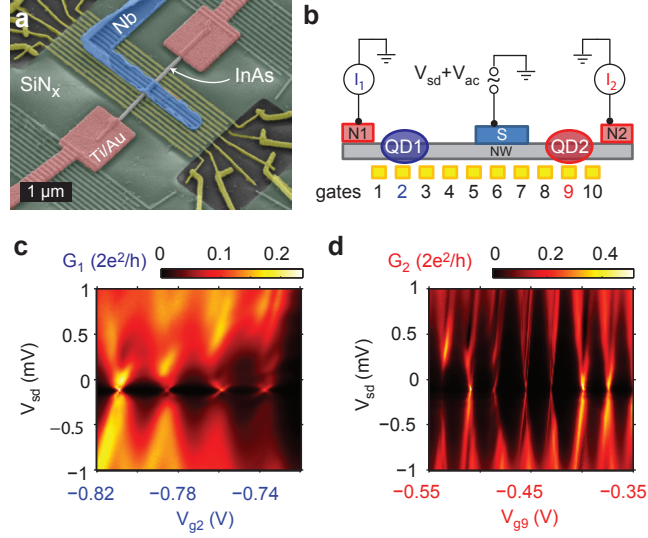


Figure 7.1.: **a** | SEM image of a representative CPS device. The InAs nanowire on the SiN_x layer (green) is contacted by a Nb lead (S, blue) in the center and by Ti/Au at the sides (N1 and N2, purple). The local gates below the SiN_x are colored yellow. **b** | Schematic of the device and the measurement setup. Gates 1-3 are used to form QD1 and gates 8-10 for QD2. Gates 6 and 7 are below S. Two more gates are not shown in the schematic and held at zero potential. **c** and **d** | Differential conductance of QD1 and QD2 as a function of the bias and the respective local tuning gate.

contact and the two normal metal drain electrodes (7/95 nm Ti/Au) were fabricated in consecutive lithography steps, with prior ammonium sulfide passivation[133] to remove the native oxide on the NW.

The experiments were carried out in a dilution refrigerator with a base temperature $T \approx 50$ mK. As illustrated in fig. 7.1b, we applied a sinusoidal voltage $V_{ac} \approx 10 \mu\text{V}$ to the superconductor S and simultaneously recorded the resulting variations in the two drain currents of contacts N1 and N2, $I_1^{(ac)}$ and $I_2^{(ac)}$, using current-voltage (IV) converters and lock-in amplifiers. We define the differential conductances through QD i as $G_i = I_i^{(ac)}/V_{ac}$. The lever arms of the different gates were found by bias spectroscopy experiments, applying a dc voltage to S. If not stated otherwise, all presented experiments were done at zero dc bias, which was achieved by compensating offsets in the IV-converters by external voltage sources (not shown in the schematics of fig. 7.1b).

The local gates g_i are numbered consecutively, as illustrated in fig. 7.1b. The tunnel barriers for the QDs are formed for the conduction band electrons in the InAs NW by applying strongly negative voltages to the local gates. For QD1, g_1 and g_3 are used to induce the barriers and g_2 to tune the dot's chemical potential (tuning gate). QD2 is formed similarly with the local gates g_8 and g_{10} , using g_9 to tune the QD resonances. The other gates are kept on ground. The exact gate voltage settings in the presented experiments can be found in Tab. C.1 in the appendix. Fig. 7.1c

shows the differential conductance G_1 as a function of V_{g2} and the applied bias, from which we estimate a charging energy for QD1 of $E_{c,1} \approx 1$ meV. The relative lever arms obtained from similar experiments with the other gates suggest that QD1 is indeed formed between $g1$ and $g3$. At low bias some resonances occur, reminiscent of Andreev bound states,[157, 158] which suggests a relatively strong coupling to S and a weaker coupling to N1. From these states we deduce an effective superconducting energy gap on or near QD1 on the order of $\Delta^* \approx 30 \mu\text{eV}$. As shown in fig. 7.1d, QD2 exhibits clear Coulomb blockade diamonds and a negligibly small energy gap ($< 5 \mu\text{eV}$). QD2 forms between $g8$ and $g10$, as expected, with a charging energy of $E_{c,2} \approx 1.5$ meV. In bias-spectroscopy experiments in which the NW is gated to the more open multi-channel regime, we find a larger energy gap of $\sim 300 \mu\text{eV}$, but still smaller than the bulk Nb gap of ~ 1.45 meV,[159] possibly related to a ‘soft gap’.[160]

7.2. Tuning of a drain tunnel barrier

Cooper pair splitting results in a non-local signal, which, for simplicity, we take here as a change of the conductance in one of the QDs when the other QD is brought to resonance. All competing processes (discussed in more detail below) are local in nature and therefore depend intrinsically only on the settings of one QD. The aim of this work is to investigate the evolution of the non-local signal in a CPS device while one tunnel barrier of a QD is varied. In this section we tune the local gate $g1$ to change the coupling of QD1 to lead N1. Due to the close proximity of $g1$ to the center of QD1, this also leads to a change in the chemical potential of QD1, which we compensate using the local gate $g2$, which allows us to compare signals of the same Coulomb blockade (CB) resonance. The conductance G_1 as a function of the two gates $g1$ and $g2$ is plotted in fig. 7.2a. The modulation of the CB resonance widths and amplitudes suggests a variation of the involved tunnel barrier strengths. Intuitively, $g1$ tunes Γ_1 , i.e., the single electron tunnel coupling to N1 (drain contact to QD1). We expect that Γ_1 decreases when V_{g1} is made more negative, i.e., Γ_1 increases from position I in fig. 7.2a to position IV. We note, however, that the modulation of the resonance amplitude exhibits more than a single maximum on a larger gate voltage scale, in contrast to what one might expect from tuning a simple tunnel barrier in a transport broadened QD. We attribute this experimental finding to the fact that the gates also tune other parts of the device, though by a considerably smaller lever arm and thus on a larger voltage scale.

We now investigate the crossings of the resonances L1 and L2 of QD1 (labelled in fig. 7.2a) with the three resonances R1-R3 of QD2. This we do for the four different $g1$ -settings I-IV indicated in fig. 7.2a, for which we expect a consecutive reduction of the tunnel coupling of QD1 to N1. Fig. 7.2b shows the differential conductances G_1 and G_2 , respectively, measured simultaneously as a function of the local gates $g2$ and $g9$ at zero magnetic field and zero bias. While $g2$ tunes QD1 through the two resonances L1 and L2, $g9$ tunes QD2 through three resonances labelled R1, R2 and R3. The resonances of the two QDs run basically perpendicular in these plots, which shows

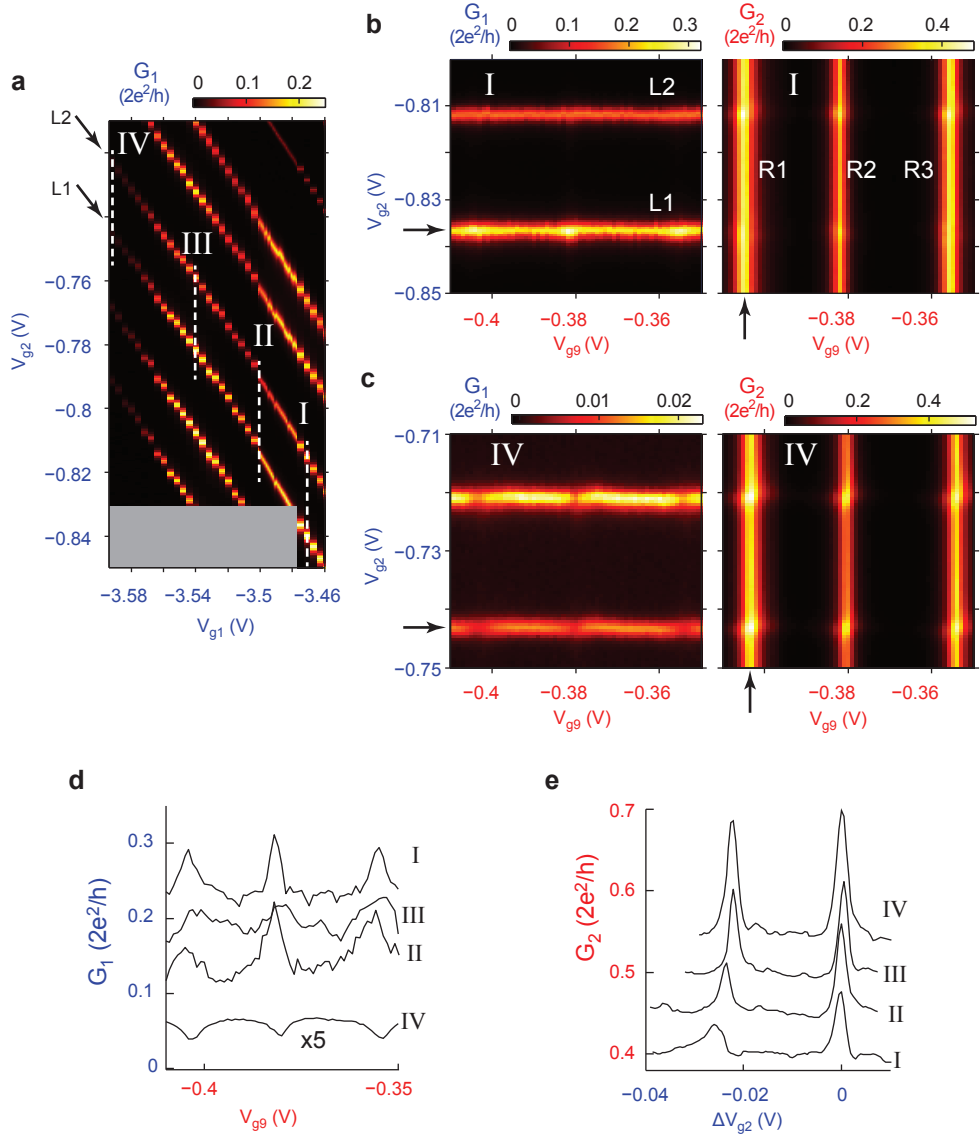


Figure 7.2.: **a** | G_1 as a function of the gate voltages V_{g1} and V_{g2} , which shows the tuning of the tunnel coupling to the normal lead of QD1. The dashed lines indicate the settings for the following experiments. **b** | G_1 and G_2 as a function of V_{g2} and V_{g9} , measured at $V_{g1} = -3.475$ V (setting I in fig. a). **c** | Conductance maps similar to b for the same QD states for $V_{g1} = -3.596$ V (setting IV in fig. a). **d** and **e** | Evolution of the resonance maxima of G_1 and G_2 along resonances L1 and R1, respectively, for the g_1 -settings indicated in fig. a (from I to IV $V_{g1} = -3.475$ V, -3.500 V, -3.540 V and -3.596 V. In d curve IV is multiplied by 5 and in e all curves are offset vertically for clarity and centred to the L2 resonance).

that the capacitive cross talk between the QDs is very small. Though not shown, we note that the conductance through QD1 and QD2 in series does not exhibit anti-crossings, which suggests that the inter-dot tunnel coupling is considerably smaller than the life-time broadening of the CB resonances.

The amplitude of one QD resonance is independent of the gate voltage applied to the other QD, except where both QDs become resonant with the Fermi energy in the leads. In fig. 7.2b both conductances increase at the resonance crossings,³ for which we use the term *positive correlation* between the conductance variations in the QDs. This positive correlation is characteristic for CPS,[19] as we discuss in more detail below. Similar gate sweeps over the same resonances in configuration IV are plotted in fig. 7.2c. Here the amplitudes of the QD1 resonances are *reduced* at the resonance crossings, while the QD2 resonances still exhibit an increased conductance. This means that, in contrast to configuration I, we find a *negative* non-local conductance correlation. We note that the non-local signal on QD2 only changes in amplitude, but not in sign. While the dips in G_1 are clearly related to the resonance on QD2, the origin is not trivial and will be discussed below. Here we only point out that 1) the background on the QD1 conductance determined by the local processes changes significantly between these gate configurations, and 2) different neighbouring QD states of similar amplitudes and widths can exhibit different correlations (not shown), excluding electrostatic effects. Also resistive cross talk[16] can be excluded as the origin of the observed effects because it would lead to a dip in both conductances at a resonance crossing.

The evolution from a positive to a negative non-local conductance correlation with the voltage on the local gate g_1 can be followed better in fig. 7.2d, where the amplitude of the QD1 resonance L1 is plotted as a function of the voltage on the local QD2 gate g_9 , V_{g9} , for the four g_1 -settings indicated in fig. 7.2a. We observe three peaks where g_9 tunes QD2 through the resonances R1-R3. The conductance variation on these crossings, ΔG_1 , are similar for the settings I and II, but decrease significantly for setting III. For the configuration IV, we find a dip instead of a peak at the resonance crossings. For all four curves the local conductance background and the non-local conductance variations both decrease with more negative V_{g1} . We note that no offsets are subtracted in fig. 7.2d and curve IV is multiplied by 5. This evolution of the non-local signal on QD1 has to be compared to the one on QD2. In fig. 7.2e the amplitude of the QD2 resonance R1 is plotted for the same g_1 -settings I-IV. Because the local conductance background is almost identical for all curves, II-IV are offset for clarity. Here we find a peak in the conductance for all four g_1 -settings as R1 crosses L1 and L2. The non-local conductance variation increases in amplitude with decreasing V_{g1} by almost a factor of 2 between I and IV.

As a measure for the CPS efficiency we use $s = \frac{2G_{\text{CPS}}}{G_1 + G_2}$, which essentially compares the fraction of currents due to CPS to the total current in the system.[19] We will see in the simple model presented below that if the non-local conductance variations are the same in both QDs, we obtain a conservative estimate for s by setting $\Delta G_{\text{CPS}} =$

³For resonance L2 this difficult to discriminate because of the conductance scale.

$\Delta G_1 = \Delta G_2$). This is applicable for the g1-setting I, for which we find, for example for the resonance crossing (L1,R2), an efficiency of $s \approx 17\%$. Clearly, we cannot use this approximation for the cases II-IV. Another useful number is the visibility of the non-local signal in one branch of the CPS device given by $\eta_i = \Delta G_i / G_i$. [19] For this purely experimental number we find for the resonance (L1,R2) and for the g1-settings I-IV $\eta_1 = 29.4\%, 27.6\%, 14.7\%$ and -40.6% , and $\eta_2 = 8.5\%, 12.8\%, 23.1\%$ and 28.7% , respectively. We note, however, that in the visibility parameters relevant in a Bell inequality test, $\eta_i = \Delta G_{\text{CPS}} / G_i$, one can set only $\Delta G_{\text{CPS}} = \Delta G_1 = \Delta G_2$, in configuration I. [19] We discuss possible origins of the evolution from a positive to a negative correlation between the non-local signals below.

7.3. Tuning of a source tunnel barrier

In this section we investigate the evolution of the non-local signals in the CPS device when tuning gate g8, which forms the barrier of QD2 to the superconductor S, see fig. 7.1b. The exact gate voltages used to form the QDs are given in Table C.1 in the Appendix. For simplicity, we only focus on a single QD2 resonance, whose differential conductance, G_2 , is plotted in fig. 7.3a as a function of the voltages applied to the local QD2 gates g8 and g9.⁴ With a more negative voltage V_{g8} the resonance amplitude and width decrease markedly. Similarly as discussed for Γ_{N1} in the previous section, this probably corresponds to a stronger barrier and a weaker coupling Γ_{S2} to S. The two vertical lines labelled V and VI are the two g8-settings for which we now investigate the non-local signals.

The QD1 and QD2 conductances, G_1 and G_2 , are plotted in fig. 7.3b as a function of V_{g2} (QD1) and V_{g9} (QD2) for setting V of g8 (see fig. 7.3a). While g2 tunes QD1 through two resonances, g9 tunes through the QD2 resonance shown in fig. 7.3a. We do not find significant capacitive or tunnel couplings (compared to the life time broadening) between the QDs. On the resonance crossings, we observe small peaks in G_1 (e.g. visibility $\eta_1 \approx 2.8\%$ on resonance ...) and more pronounced peaks in G_2 , see fig. 7.3b ($\eta_2 \approx 48\%$). Again we take this positive correlation between the non-local conductance variations as an indication for CPS. However, we could not tune these resonances to a g8-setting for which $\Delta G_1 = \Delta G_2$. The amplitude of the QD2 resonance is plotted in fig. 7.3c, curve V, as a function of the QD1 gate g2, which shows the peaks at the crossings. The main finding in this section is that the same experiment for configuration VI, i.e. for a more *positive* voltage on g8 leads to dips in the amplitude of G_2 at the resonance crossings, see curve VI in fig. 7.3c (e.g. visibilities of resonance crossing ...: $\eta_1 \approx 16.5\%$, $\eta_2 \approx -23.2\%$). Because the non-local signals on G_1 are still positive (not shown), this corresponds to a negative correlation between the non-local conductance variations. This is remarkable since this evolution of the non-local signals from a positive to a negative correlation was induced in section III by tuning g2 to more *negative* voltages. We discuss a possible

⁴Due to a charge rearrangement we were not able to exactly identify the same resonances as used in section III.

explanation in section V.

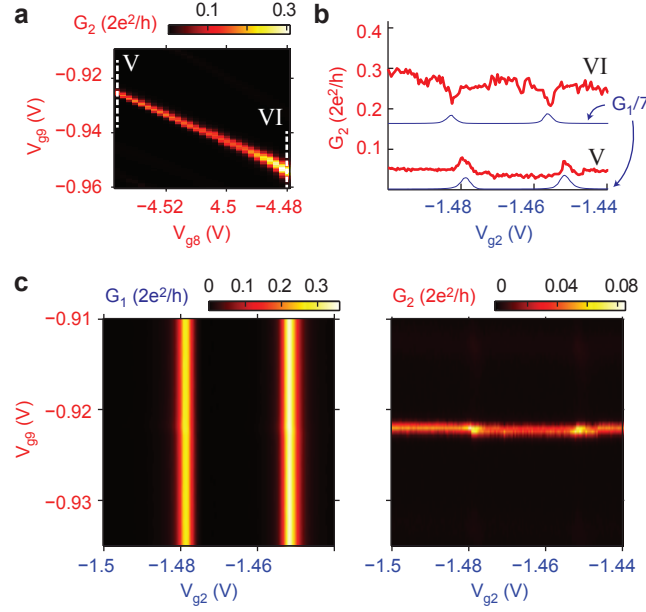


Figure 7.3.: **a** | Differential conductance of QD2, G_2 as a function of the two local gates g_8 and g_9 . Two gate configurations, V and VI, are indicated by colored lines. **b** | G_1 and G_2 as a function of the QD1-gate g_2 and QD2-gate g_9 showing two resonance crossings in the gate configuration V. **c** | Amplitude of the QD2 resonance for g_8 -settings V and VI when QD1 is tuned through the two respective resonances shown in b.

7.4. Tuning of the inter-dot coupling

In a third experiment we defined the QDs using only two gates, namely g_4 and g_5 for QD1 and g_8 and g_9 for QD2, see Table C.1 in Appendix A. For this reason we use a barrier-defining gate, g_8 , to tune the chemical potential of QD2. The aim is to investigate the effect of the gates g_6 and g_7 *below* the superconducting contact S on the non-local signals. Because of the finite size of the NW and despite the screening by the superconductor, we expect that the electron density below S is reduced when the gates are set to more negative potentials, which should lead to a reduction of the single electron tunnelling rate between the QDs. In fig. 7.4a the amplitude of a QD1 resonance (G_1) is plotted as a function of V_8 , i.e. the gate defining QD2, while the amplitude of a QD2 resonance (G_2) as a function of V_2 , i.e. a gate of QD1, is shown in fig. 7.4b. The curves have the same background (local) conductance within experimental error and are shifted vertically for clarity. This suggests that the tunnel barriers to the source and drain contacts are not significantly altered by the gates g_6 and g_7 . In addition, the curves are shifted horizontally so that the resonance crossings are centred at $\Delta V_8 = 0$ and $\Delta V_2 = 0$, respectively. This is necessary because these

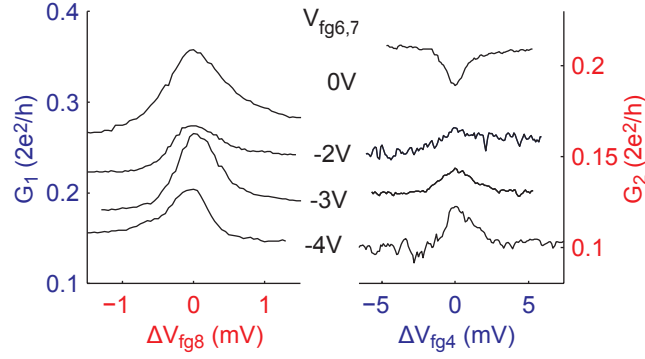


Figure 7.4: **a** $|G_1|$ as a function of the voltage on gate g8 (V_{g8}), which tunes QD2 through a resonance for a series of voltages $V_{g6} = V_{g7}$ applied to the gates below S. The curves are shifted vertically for clarity and horizontally such that the resonance crossings occur at $\Delta V_{g8} = 0$. **b** $|G_2|$ as a function of V_{g5} , which tunes QD1 through a resonance. The curves are shifted similarly as in (a).

gates affect the resonance position of both QDs by a small capacitive coupling. In all experiments we set $V_{g6} = V_{g7}$. For $V_{g6} = V_{g7} = 0$ the non-local signal on QD1 is positive, but negative on QD2, so that we find a negative correlation between the non-local conductance variations at the resonance crossing. When we continuously tune both gate voltages to more negative values, the non-local signal at the resonance crossing on QD2 evolves from negative to positive values, while the non-local signal on QD1 is only slightly reduced. At $V_{g6} = V_{g7} = -4$ V we find a positive correlation of the non-local signals with similar amplitudes. The visibilities in the two arms evolve with decreasing voltage from $\eta_1 = 0.42$ and $\eta_2 = -0.23$ at $V_{g6} = V_{g7} = 0$ to $\eta_1 = 0.26$ and $\eta_2 = 0.17$ at $V_{g6} = V_{g7} = -4$ V. In the next section we present a simple model that qualitatively explains these and the above findings.

7.5. Simple model

In the experiments presented above we find large qualitatively and quantitatively differences in the conductance variations at resonance crossings of the two QDs. These ‘non-local’ signals are surprisingly simple to tune from a positive to a negative correlation. In fact, we can induce such transitions by using any single local gate. In this section we present a simple toy model (similar to the one in Ref. [19]), which qualitatively describes the experimental findings and allows to identify the physical mechanisms that could lead to the observed transitions in the conductance correlations. The two basic ideas are that 1) the different local and non-local processes compete for the QD occupation, which lets these processes interfere with each other, and 2) a finite inter-dot coupling can lead to currents between the QDs that are not related directly to tunnel processes involving the superconductor S.

We first describe the model in some detail. Because of the large charging energy,

each QD can only be empty or occupied by a single electron at a time, i.e., the system occupies the states $(0,0)$, $(1,0)$, $(0,1)$ or $(1,1)$, which correspond to no electrons in the system, one in QD1 or in QD2, or an electron in both QDs, respectively. As illustrated in fig. 5, we consider several processes that lead to transitions between the system states with rates determined by the tunnel couplings of the QDs to the three contacts, see Table 1. Γ_{N1} and Γ_{N2} are the couplings to the normal metal contacts, Γ_{S1} and Γ_{S2} to S, and Γ_{12} is the direct coupling between the QDs. The steady state QD occupations $P_{(i,j)}$ can be calculated in a classical rate equation. The processes we consider here are 1) tunnelling of an electron from a QD to the respective normal electrode with the rates Γ_{N1} and Γ_{N2} (denoted by SET, single electron tunnelling). This process leads to a current in the respective contact. 2) local pair tunnelling (LPT), where the electrons of a Cooper pair (CP) are transmitted sequentially through the same QD i . This requires the QD to be empty initially and leads to an electron emitted to lead N_i and to the occupation of the QD i by the second electron. The probability of this process scales with $\Gamma_{Si}^2\Gamma_{Ni}$. 3) Cooper pair splitting, where the electrons of a Cooper pair tunnel into two empty QDs. CPS scales as $\Gamma_{S1}\Gamma_{S2}$ and leads to two full QDs, but not directly to a current in the normal leads. 4) Here we also investigate in more detail the effect of a direct single electron tunnel coupling between the QDs (SET between QDs), which scales directly with Γ_{12} . 5) Because of a possibly large inter-dot coupling, we also consider the processes where Cooper pair electrons sequentially tunnel to one QD and the first leaves the dot by tunnelling to the other QD. We call these processes *sequential CPS* (SCPS), stressing that they lead to a transition of two empty dots to two filled dots, similar to the direct CPS considered above. Sequential CPS scales as $\Gamma_{Si}^2\Gamma_{12}$ and do not lead directly to a current in the normal leads. 6) As a last process we also consider the tunnelling of a single electron from S to one of the QDs, which scales with Γ_{Si} . We assume that electrons tunnel effectively only from S to N1 or N2.

Each process should be weighted in addition with individual prefactors accounting for the density of states, differing effects of the superconductor energy gap (e.g., a soft gap allows the emission of single electrons) and the inverse scaling of the CPS probability with the separation between the emission positions of the two Cooper pair electrons.[111] Since we only aim for a qualitative picture, we refer the reader to the literature for more involved techniques (Refs) and simply set the prefactors for

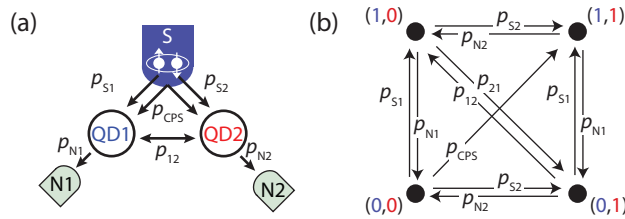


Figure 7.5.: **a** | Schematic of the device and transition probabilities. **b** | Schematics of transitions between the allowed system states.

Process	diagram	rate	transitions
SET to N1		$\Gamma_{N1} (\Gamma_{N2})$	$(1, 0) \rightarrow (0, 0)$ $(1, 1) \rightarrow (0, 1)$
LPT into lead N ₁		$\Gamma_{S1}^2 \Gamma_{N1}$	$(0, 0) \rightarrow (1, 0)$ $(0, 1) \rightarrow (1, 1)$
CPS		$\Gamma_{S1} \Gamma_{S2}$	$(0, 0) \rightarrow (1, 1)$
SET between QDs		Γ_{12}	$(1, 0) \rightarrow (0, 1)$ $(0, 1) \rightarrow (1, 0)$
SCPS via QD 1		$\Gamma_{S1}^2 \Gamma_{12}$	$(0, 0) \rightarrow (1, 1)$
SET from S to QD1		$\Gamma_{S1} (\Gamma_{S2})$	$(0, 0) \rightarrow (1, 0)$ $(0, 1) \rightarrow (1, 1)$

Table 7.1.: Single electron and Cooper pair transport processes taken into account in the model: acronym, rate and transition in QD occupancies.

CPS and SET from S to $k = 0.1$ and all other prefactors to 1. We note that we do not modulate the resonance widths with the tunnel couplings, which is not a straight forward task (Refs).

We calculate the conductance into N1 (similar for N2) from the average system state occupation, $P_{(i,j)}$, and the probability for local SET and LPT to N1:

$$G_{N1}/G_0 = \Gamma_{N1} [P_{(1,0)} + P_{(1,1)}] + \Gamma_{S1}^2 \Gamma_{N1} [P_{(0,1)} + P_{(0,0)}]$$

Similar expressions can easily derived for the other currents in the system. In particular, the ratio of CPS can be found as

$$G_{\text{CPS}}/G_0 = k \Gamma_{S1} \Gamma_{S2} P_{(0,0)}$$

In this model we only find a positive correlation between the conductance variations on the two QDs on a resonance crossing if the CPS rate is non-zero. In other words: even with many other processes involved, CPS can be identified qualitatively by a positive correlation of the non-local signals. A negative correlation between the non-local signals, however, can have different mechanisms: A) with a finite inter-dot

coupling the current through one QD can be partially diverted to the other QD, thereby decreasing the current to the one drain contact and increasing the current to the other. No non-local process is involved in this scenario for negative correlations. B) On each QD the local processes and CPS compete for the dot occupation. For example, switching on CPS by bringing QD2 into resonance leads to an increase of the average QD1 occupation, which reduces the frequency of the local processes. For this mechanism no inter-dot coupling is required.

In fig. 7.6 the resulting conductances through the QD1 (left column) and QD2 (right column) into the respective normal metal contacts are plotted for a series of systematic changes of a single tunnel coupling, with all other parameters held constant (the values are given in the caption to fig. 7.6). Figs. 7.6a and fig. 7.6b show the evolution from a positive to a negative conductance correlation in the non-local signals when reducing Γ_{N1} , similar to the experiments in Section III. In our model we can trace this transition to an increased population of QD1 when the barrier to N1 is made more opaque, so that the tunnel coupling to QD2 becomes more relevant as a path to emit electrons from QD1. We point out that the inter-dot coupling is not necessarily a direct single electron process, but could also be due to higher order processes mediated by the superconductor. It is interesting to note that in our simple model we were able to generate strong negative conductance correlations similar to the experiments only if we included quasi particle tunnelling from S.

Figures. 7.6c and 7.6d show the effect of tuning the coupling of QD2 to the superconductor S. Here the increased coupling to S leads to an increase of the QD2 population ('stronger filling rate') and a transition from a positive to a negative conductance correlation. In particular, a *weaker* barrier to S has a similar effect as a *stronger* barrier to the normal metal contact, in qualitative agreement with the experiments in sections III and IV.

In figs. 7.6e and fig. 7.6f the effect of tuning the inter-dot coupling is investigated, which should be compared to the experiments in Section V. Here we start with a negative conductance correlation by setting $\Gamma_{S2} = 0.5$, i.e., due to a large QD2 population (all other rates are the same as above). When the inter-dot coupling Γ_{12} is reduced, we find a transition from the negative to the positive conductance correlation. The relation to the gates g6 and g7 in Section IV is quite intuitive, since they probably tune the electron density below S and thus might pinch-off the coupling between the QDs.

7.6. Summary

In summary, we report the tuning of the non-local signals by local bottom gates in a Cooper pair splitter device with a Nb contact. We find strong systematic transitions between positive and negative conductance correlations on resonance crossings, which can be explained qualitatively by the electron dynamics on the double dot system and Cooper pair splitting. In the presented simulations it is clear that the CPS part is modulated strongly by tuning the local gates. However, in the experiments the

different contributions to the conductances are difficult to disentangle. The recovery of the positive correlations with all relevant gates strongly suggests that the CPS signal can be optimized using local gating techniques, which is an important step towards a reproducibly working source of entangled electron pairs.

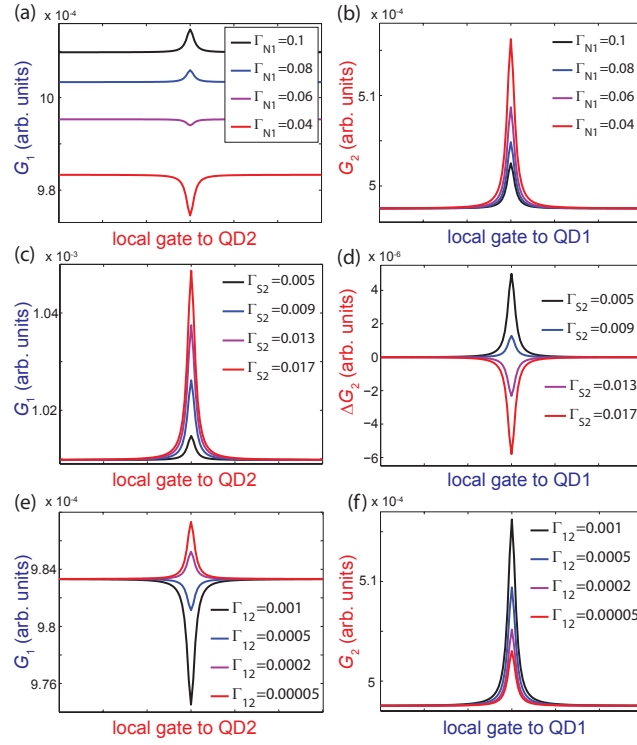


Figure 7.6.: Results of the model calculation showing the transition between positive and negative correlations between the conductance variations on a resonance crossing. If not stated otherwise in the subfigures, the tunnel couplings are set to $\Gamma_{S1} = 0.01$, $\Gamma_{N1} = 0.001$, $\Gamma_{S2} = 0.005$, $\Gamma_{N2} = 0.05$ and $\Gamma_{12} = 0.001$. **a and b** | Transition induced by tuning Γ_{N1} , **c and d** | transition induced by tuning Γ_{S2} , and **e and f** | transition induced by tuning Γ_{12} , for fixed to $\Gamma_{S2} = 0.5$.

8. High-Bias Cooper Pair splitting

In the last chapter results with current correlations as function of level position and coupling in a Cooper pair splitter device have been presented. However, additional device parameters are accessible. In particular the electrochemical potential of the leads can be controlled by the applied bias voltage which was kept at zero in the last chapter. The bias voltage can tune the relative weight of the different transport processes, crossed Andreev reflection (CAR), elastic co-tunneling (EC) and local pair tunnelling (LPT). For example, symmetric biasing allows no net current contribution from EC. When the bias voltage is larger than the superconducting gap additionally quasi-particle tunneling (QPT) processes become available.

In this chapter we present preliminary results of a similar Cooper pair splitter device as in chapter 7, where the two normal leads are individually biased. Similar early experiments in biased metallic NSN structures enhance the CAR over the EC by excitation of modes in the electrostatic environment [108, 161, 162] which is experimentally difficult to control. By inserting QDs between the N and S lead the CAR process is enhanced by the electron-electron interaction on the QD instead [111]. The bias voltage is now used to put the QDs most of the time in an empty state (sec. 3.4.2). CPS device based on InAs were investigated at finite bias by Hofstetter *et al.* but lacked a clear quantum dot in the second arm [113]. Moreover, they did not observe an increase in splitting efficiency as suggested by theory [111, 163]. Here we present an improved device with quantum dots in both arms operated in the closed dot regime and find indications that CPS is possible at bias voltages larger than the superconducting gap (hence the term high-bias). However, the measurements have been performed rather recently in Basel and they should be considered preliminary together with the analysis.

8.1. Device and Measurement Set-up

An SEM image of the sample is shown in fig. 8.1a. The fabrication followed the description in chapter 4: First, bottom gate arrays of nine gates were fabricated on a SiO₂ layer covering a highly doped Si substrate. The bottom gates consist of 4 nm Ti and 18 nm Pt and have different widths depending on their position. The outer most gates and the central one are wide and located below the nanowire contact in order to increase the local electron density and improve the ohmic contacts. In between are three thin gates (~ 40 nm wide) on each side to form the QDs. The bottom gates are overgrown by 25 nm SiN_x in a plasma-enhanced chemical vapour deposition (PECVD). After the deposition of individual nanowires by micromanipulators, the SiN_x is locally removed by reactive ion etching (RIE). Contacts to the bottom gates

and to the nanowire are then fabricated in subsequent electron beam lithography (EBL) steps whereas the native oxide on the nanowires is removed by Ar sputtering. We evaporated a Ti/Pd (5/105 nm) bilayer as normal leads and a Ti/Al (4.5,120 nm) bilayer as superconducting contact.

Measurements are performed in a dilution refrigerator operating at 50 mK. A magnetic field can be applied perpendicular to the sample plane. The differential conductances are measured in a voltage bias set-up which is shown schematically in figs. 8.1b. An ac voltage of $V_{ac} \approx 10 \mu\text{V}$ is applied to the central superconducting (S) lead at a typical frequency of $f = 133 \text{ Hz}$. The resulting current modulations in the normal leads (N1, N2) are translated to voltages by homebuilt current-voltage (IV) converters and demodulated by two phase-locked lock-in amplifiers. A symmetric dc biasing scheme is used where the dc voltage V_S is applied on the S lead. The dc offset of one IV-converter is adjusted by a constant voltage V_{comp} to match the dc offset of the other IV-converter, thus the electrochemical potential in the normal leads stay the same but a constant offset of $V_S = 0.15 \text{ mV}$ corresponds to a real zero bias setting.

The bottom gates fgi are numbered consecutively from lead N1 to N2 as illustrated in fig. 8.1c. Before forming QDs in each arm of the nanowire we characterize each gate response at 4 K with a large-range voltage sweep while measuring the conductance. The resulting curves are plotted in fig. D.1. Not all gates allow to deplete the wire within a reasonable gate voltage range that does not risk electrical breakdown of the insulator (SiN_x). These gates can only partially be used to induce a tunnel barrier in the NW. Nevertheless, QD1 can be formed by applying negative voltages to gates $fg2$ and $fg3$, while the other gates on this side are kept at positive potential. On the other hand QD2 is mainly induced by the single gate $fg8$, although the $fg6$ and $fg7$ have large negative potentials.

We investigate a single resonance of QD1 and two resonances of QD2. The resonances are shown in 8.1c for QD1 and 8.1d for QD2 as function of V_S . As plunger gates we use $fg3$ and $fg8$ which have the largest lever arm on the corresponding QDs indicating the QDs are formed above the respective gate. From measurements over a larger gate and bias range we estimate the charging energies $E_{C,1} \approx 2 \text{ meV}$ and $E_{C,2} \approx 4.5 \text{ meV}$. The tunnel couplings for all resonances are $\sim 100 \mu\text{eV}$, which is of the same order of magnitude as the effective superconducting gap $\Delta \approx 120 \mu\text{eV}$ observed more clearly in both arms of the CPS in the open dot regime. By similar bias-spectroscopy measurements, we find a critical field of 20 mT also in agreement with field dependence of the resistance of the superconducting contact strip. The gap is smeared out and hardly visible in the closed dot regime and Andreev and quasi-particle processes dominate the 2-terminal conductance. We emphasize that all measurement and numbers related to the bias voltage are offset by $150 \mu\text{V}$. The gap edges are therefore found at $30 \mu\text{V}$ and $270 \mu\text{V}$

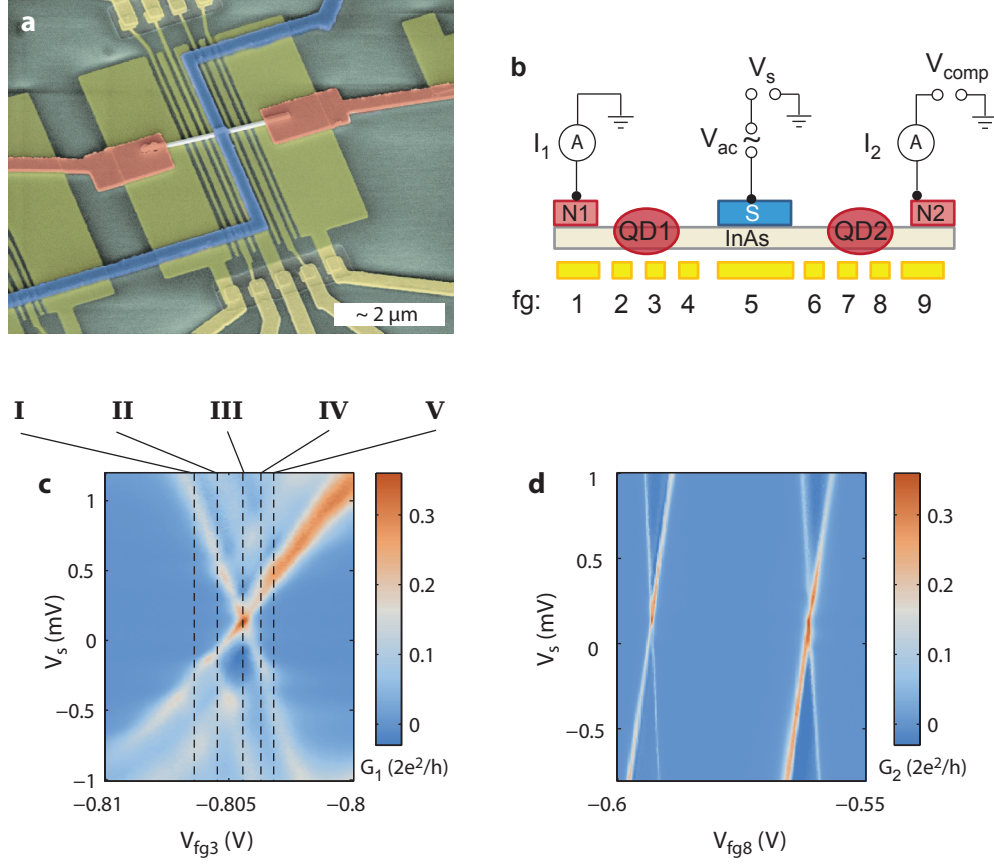


Figure 8.1.: **a** | Artificially coloured SEM image of the investigated device. The superconducting lead S (Ti/Al) is blue, the normal leads are red (Ti/Pd), bottom gates yellow and the SiN_x green. **b** | The measurement set-up integrated in a device schematic with colours corresponding to a. An ac bias V_{ac} and a dc bias V_s is applied symmetrically to the device on the central S lead. The offsets of the ammeter (IV-converter) are compensated by V_{comp} to keep the lead N1 and N2 at the same potential. **c** | Differential conductance $G_1 = dI/dV_{ac}$ as function of the bias voltage V_s and the local gate voltages V_{fg3} through the left arm of the CPS. The different markings **I-V** around the resonance illustrates the measurements in fig. 8.3 **d** | Same measurement as in c but through the right arm and as function of V_{fg8} .

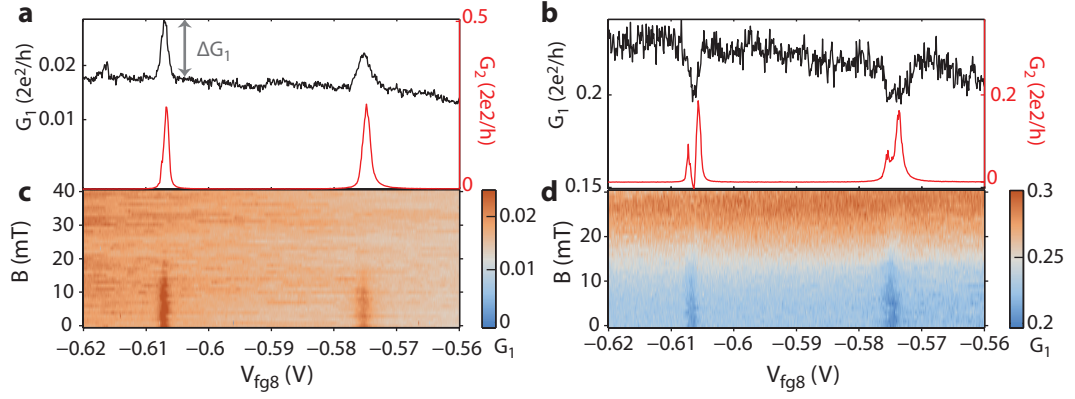


Figure 8.2.: **a** | Differential conductance G_1 (black) and G_2 (red) as function of V_{fg8} at finite dc bias $V_S = 0.27$ meV and fixed V_{fg3} . G_1 shows a clear positive non-local signal ΔG_1 whenever QD2 is on resonance. **b** | The same measurement as in **a** at larger dc bias voltage $V_S = 0.41$ meV. G_1 exhibits in this case a negative ΔG_1 . **c,d** | G_1 additionally as function of magnetic field. The non-local signals vanish around 20 mT in accordance with the suppression of the superconductivity in the S lead.

8.2. Non-local signals at large bias voltages

We find significant non-local signals at a finite bias voltages. In fig. 8.2a, QD1 set to an fixed off resonant position by gate fg3 and QDs are symmetrically biased by increasing V_S to 0.27 meV leading to a small background conductance of $G_1 \approx 0.018 G_0$ through QD1, where $G_0 = 2e^2/h$. Then, two resonances of QD2 are tuned through the opened bias window by gate fg8 and G_1 and G_2 is simultaneously recorded. G_2 is shown as red conductance curve in fig. 8.2a and exhibits two broadened peaks being actually two resonances due to the applied finite bias. G_1 (in black) shows peaks at the same fg8 voltages as G_2 on top of a background. The background conductance is only changing marginally due to a lever arm of gate fg8 on QD1 (cross capacitance) which is about 500 times smaller than the lever arm of fg3. Therefore, we fit the background with a linear regression and subtract it to obtain the change in differential conductance $\Delta G_1 = G_1 - G_{background}$ and extract $\Delta G_1 = 0.011 G_0$ exemplary for the left resonance of QD2 in fig. 8.2a. Since G_1 depends on QD2, we call this the non-local signal.

The same procedure is repeated at a larger bias $V_S = 0.41$ mV (fig. 8.2b top). Due to the large bias, the local resonances in G_2 (red) are split into two peaks corresponding to the QD level aligned with source or drain chemical potential. In contrast to the lower bias, we find a decreased differential conductance G_1 when the levels of QD2 are in the bias window and extract an negative $\Delta G_1 = -0.0273 G_0$ again for the left resonance. At even larger bias voltages the non-local signals vanish.

The bottom graphs in fig. 8.2 (c,d) show the magnetic field dependence of the corresponding signals above it. The positive as well as the negative ΔG_i disappear at the same field scale as the superconducting gap. This confirms that the effect is

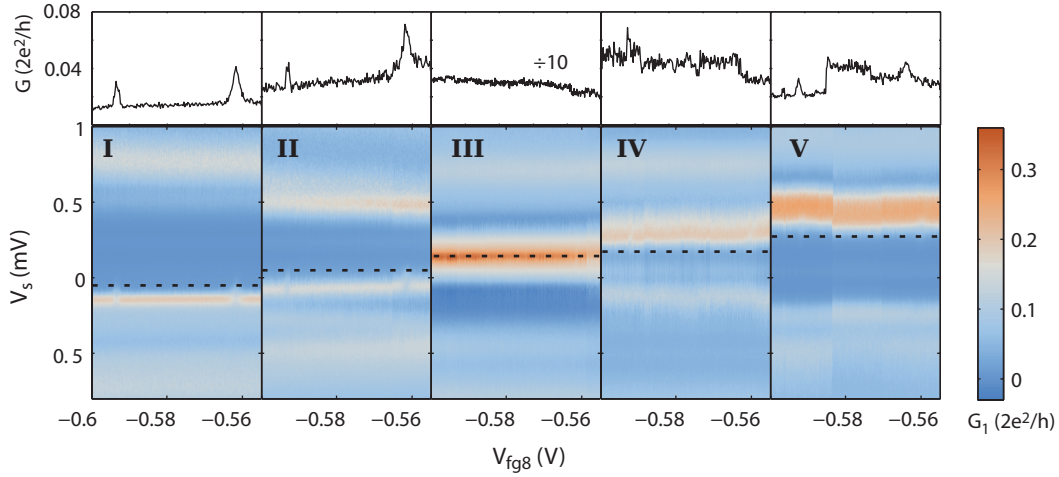


Figure 8.3: a | Non-local differential conductance G_1 as function of the local gate voltage V_{fg8} and symmetric bias voltage V_S for different fixed gate voltages V_{fg3} labelled **I-V** and shown in b. Non-local signals are observed at $V_{fg8} = -0.56$ V and $V_{fg8} = -0.595$ V but at various bias voltages in settings **I-V**. For clarification, line cuts of G_1 from the dashed lines are presented above the contour plots. The colorscale is the same for all contour plots

related to superconductivity. In contrast to earlier work [16] no resistive cross talk is observed when the superconductivity is suppressed.

8.3. Gate and Bias dependence of the non-local signals

The separate tunability of each QD allow us to investigate dependence of the non-local signal on the energy level position of QD1. For this purpose we fix the gate voltage V_{fg3} at different values and record G_1 and G_2 as function of V_{fg8} . At the same time we measure the bias dependence by varying V_S . Thus, in such a measurement G_2 reproduces basically the plot in fig. 8.1d, whereas G_1 is plotted in fig. 8.3. The fixed voltages V_{fg3} are indicated in fig. 8.1c for the situations **I-V**. Situation **I & II** are on left of the Coulomb resonance, situation **III** is right on it and situation **IV & V** are on the right side, i.e. at larger occupation number of QD1.

Positive and negative non-local signals (ΔG_1) are observed in different gate bias settings. In the following we describe the pattern of the appearing non-local signals. In settings **I** and **II** non-local signals occur at negative bias voltage while in setting **IV** and **V** the small indications of non-local conductance change can be found at positive V_S . Opposite biasing reveals no non-local signal in these situations. When the resonance of QD1 is at zero bias (situation **III**) no conductance change in G_1 can be made out either. Further, any observed non-local signal is either found at $V_{fg8} = -0.56$ V or $V_{fg8} = -0.595$ V corresponding to a resonant situation of QD2. The positive and negative non-local signal follow a pattern along the bias axis in fig. 8.3. At low conductance of QD1 and at small absolute bias voltages the non-

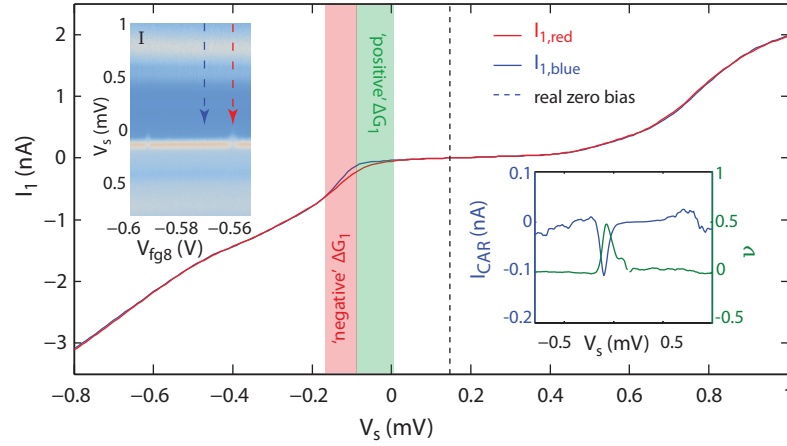


Figure 8.4.: Calculated current-voltage characteristics from the non-local conductance G_1 in situation **I** shown again in the left inset. , the red curve when it is at resonance. Clearly the absolute current I_1 is increased in the red and green coloured bias interval. The increase is attributed to CAR and plotted in the right inset (in blue). The extracted maximal efficiency is shifted against the maximal current and reaches 48%

local signal ΔG_1 is positive. As the bias voltage is increased ΔG_1 vanishes before turning negative. The largest negative ΔG_1 is generally found at the maximal G_1 along the bias axis. At very large bias voltages the non-local signal disappears. From considerations of a QD level as function of gate voltage and chemical potentials of the lead, it becomes clear that the non-local signals are only observed when the QD level is aligned with chemical potential of the source lead, which is in our case the S contact.

We note that in situation **I** and **V** the non-local signal arises at bias voltage $|V_S|$ is clearly larger than the superconducting gap whose edges are at $150 \pm 120 \mu\text{eV}$ due to the IV-converter offsets. However, there is generally no non-local variation of G_2 . We tentatively explain this by electron dynamics of the two QDs modelled with a rate equation *ansatz* [19, 164].

For a better understanding the current rather than the differential conductance is considered. As an example we take the measurement from fig. 8.3 in situation **I** and integrate G_1 numerically along the bias axes, thereby obtaining the current I_1 . We employ a trapezoidal algorithm starting from $V_S = 0.15 \text{ mV}$ towards both positive and negative bias. The current-voltage characteristics is shown in fig. 8.4 for two different gate voltages V_{fg8} . The blue curve $I_{1,\text{blue}}$ is obtained when QD2 is in Coulomb blockade ($V_{fg8} = -0.57$) the red one $I_{1,\text{red}}$ when QD2 is on resonance ($V_{fg8} = -0.562$). The values of V_{fg8} are also marked in the right inset in fig. 8.4 with blue and red arrows.

We find that the absolute current through QD1 I_1 is larger when QD2 is resonant. In fig. 8.4 the bias interval $V_S = [-0.17, 0.02] \text{ mV}$ is coloured red and green where the current $I_{1,\text{red}}$ is more negative than $I_{1,\text{blue}}$. This is also the interval where we

observe positive and negative ΔG_1 . At bias voltages outside of this interval the current through QD1 is approximately equal but asymmetric in bias voltage.

The additional current when QD2 is on resonance is ascribed to Cooper pair splitting and crossed Andreev reflection (CAR), respectively. The difference $I_{\text{CAR}} = I_{1,\text{red}} - I_{1,\text{blue}}$ is shown in dark blue in the right inset of fig.8.4 together with the visibility in green defined as $\nu = \frac{I_{\text{CAR}}}{I_{1,\text{red}}}$. In doing so, we assume that the local processes giving rise to current $I_{1,\text{blue}}$ do not change when QD2 becomes resonant. The maximal non-local current $I_{\text{CAR,max}}$ is found at a bias voltage of -0.1 mV and with value of 0.1 nA. The maximal efficiency is however shifted towards larger bias voltages. We find a maximal efficiency of $\xi = 48\%$ at $V_S = -0.07$ mV.

8.4. Discussion

The asymmetry in bias voltage is easily explained due to capacitive effects of the source and drain leads (see sec. 5.0.3). More critical is the extraction of tunnel couplings of the quantum dots with the superconductivity present in S. However, the conductance is hardly suppressed inside the gap, what we attribute to single particle processes. Therefore, we think that the extracted Γ reflect quite well the intrinsic tunnel coupling.

In the following we argue that CAR can still be possible at bias voltages larger than superconducting gap $|eV_S| > \Delta$ just because of the small tunnel coupling of the QDs. In the discussion it is assumed that $\delta E, E_C > |eV_S|$ and only a single level contributes to the transport. The energy space diagram in fig. 8.5a corresponds to situation **I** at negative $V_S = -0.06$ mV. The resonant level of QD1 is approximately aligned with the chemical potential of S μ_S . The lifetime broadening of the level is depicted as tunnelling density of states (TDOS) as (green dashed line). The chemical potentials $N1$ and $N2$, μ_{N1} and μ_{N2} are equal because the device is symmetrically biased. Therefore, no net current from EC processes is expected. In the measurement a level of QD2 is now moved through the bias window making the CAR process possible as the level is aligned with the tunnelling density of states of QD1. The CAR process is marked by orange arrows indicating the two electron originating from the Cooper pair condensate at μ_S . The black arrow in fig. 8.5a symbolizes a single electron originating from a quasi-particle states below $-\Delta$ and tunnelling through QD1. However, at energies smaller than $-\Delta$ there is only very little TDOS and the quasi-particle tunnelling (QPT) is filtered by the position of the QD level.

In fig. 8.5b, V_S is further lowered opening a larger bias window. In the energy diagram this means that μ_S is higher in energy. The QD1 level is slightly dragged along due to the source capacitance and marked by the red position and red TDOS. This situation corresponds to the voltage range also marked red in fig. 8.4 where we observe a negative ΔG_1 . The current I_1 through QD1 is in fig. 8.5b generally increased because the QPT from below $-\Delta$ are possible (black arrow). The current leads to an increased occupation the dot compromising the ideal CAR condition that the QDs should be empty on average. This means that CAR is suppressed as the

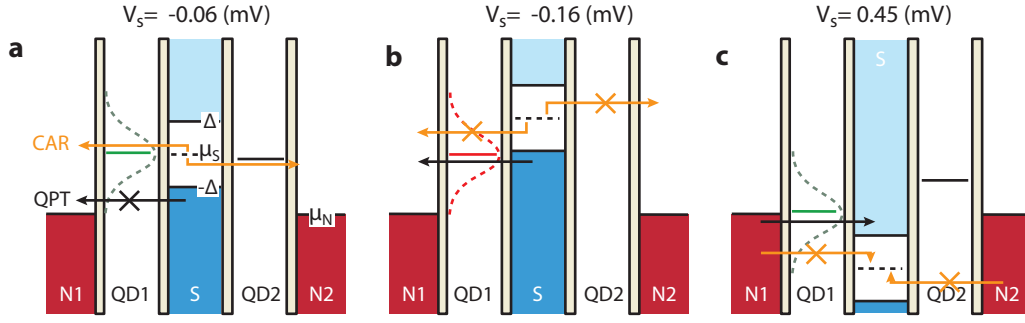


Figure 8.5.: **a** | Energy diagram illustrating the situation in the green coloured region in fig. 8.4 . The broadening of QD1 level is indicated as dashed green line. Quasi-paritcle transport from below the gap is energetically filtered by the small broadening of the QD and CAR is the dominant process. **b** | Same energy diagram as in (a) but the bias is more negative. The QD1 resonance is aligned to the lower edge of the superconducting gap $-\Delta$ thereby allowing quasi-particle processes to take over and suppressing CAR. **c** | Same energy diagram as in (a) but the bias is positive. The QD1 level is aligned with the normal lead chemical potential μ_N . Local quasi-particle processes will dominate the transport. This time the electrons tunnel from the N1 through QD1 into quasi-particle density of states above Δ (black arrow). The TDOS favours processes above the gap and CAR (in this case Cooper pair formation) is suppressed too.

bias is increased further and further and only quasi-particle and local processes occur leading to equal current $I_{1,\text{red}}$ and $I_{1,\text{blue}}$.

At positive bias voltage but same gate setting **I**, the QD1 level is aligned with the normal lead chemical potential as depicted in fig. 8.5c. Again local quasi-particle processes will dominate the transport. This time the electrons tunnel from the N1 through QD1 into quasi-particle density of states above Δ (black arrow). The TDOS favours processes above the gap and CAR (in this case Cooper pair formation) is suppressed too.

We are aware that QD2 is basically neglected in this discussion. We expect a clear dependence of the CAR signal on the energy of the QD2 level according to the double Breit-Wigner resonance (eq. 3.15). However, this is not what we observe. Instead it seems sufficient that a transport channel through QD exists. Further measurements are needed to clarify this. As the analysis suggest it is important to measure the dc current too, as soon as CPS devices are biased.

8.5. Summary

In summary, we present preliminary results and interpretation on bias dependent measurements of tunable Cooper pair splitter device based on InAs nanowires with two well defined quantum dots. The lifetime broadening of the QDs is smaller than the superconducting gap what fulfills a prerequisite for a large Cooper pair splitting efficiency. Strong indications are found that crossed Andreev reflection is possible at bias voltages larger than the superconducting gap. By integration of the measured differential conductance we assign 48% of the current to Cooper pair splitting. Elastic co-tunnelling process in this specific case can be excluded because the device is biased symmetrically and the domination of the CAR process is motivated by the strong

energy filtration effect of the clean QDs. On the other hand no double Breit-Wigner resonance is observed questioning the obtained results. Further measurements also including the pure dc currents are needed to clarify the results.

9. Summary and Outlook

This thesis focused on the Cooper pair splitting devices made from InAs nanowires. In such devices, two quantum dots (QDs) are coupled to a common superconducting electrode S. Each of the QDs is further connected to a normal leads N1 and N2. The electron-electron interaction in the QDs enhances the splitting of the Cooper pairs, however the exact splitting efficiency depends on the couplings Γ_S to S and $\Gamma_{N1,N2}$ to N1 and N2 electrodes, but also other parameters as the coupling between the dots Γ_{12} , the superconducting gap Δ and the bias voltage.

In chapter 5 we explore quantum dot formation in InAs nanowires and showed, that tuning of the coupling strengths is best possible with multiple gate structures below the nanowire. Such bottom gate structures provide less noisy measurements than top gated devices used in earlier device designs [16, 141]. CPS devices with integrated bottom gates were investigated in chapters 7 and 8. Tuning the local gate voltages we found non-local signals that systematically cross over from positive to negative correlation and show that the CPS signal can be optimized. The electron dynamics on the double dot system provide a qualitative explanation for the results.

A bias voltage can increase the splitting signal as well [111]. In chapter 8 we addressed this question with a second CPS device. Preliminary results indicate that Cooper pair splitting is indeed increased and even possible at bias voltages larger than the superconducting gap what is motivated by the strong energy filtration effect of small QD level broadenings that could be achieved with the bottom gates. Extended measurements are needed to confirm the results in preferably even cleaner and better devices.

Different ways are suggested to further improve the "cleanliness" of the InAs CPS. Theoretical work has shown that the transport at the InAs-S interface can be dominated by additional states inside the superconducting gap [160]. Lately, InAs nanowires could be epitaxially overgrown by an Al layer providing more pronounce gap features [165]. Better tunability might be achieved by reducing the surface defects and scattering. For this purpose the surface of the InAs nanowire is passivated by long alkane molecules with a linker group [166, 167] or radial heterostructure shell, e.g. out of InP [45].

A high splitting efficiency is ultimately needed for entanglement detection no matter which proposal is implemented. The proposals suggest a beam-mixer set-up with noise measurements [168] or non-collinear spin projection measurements with the help of ferromagnetic contacts. The InAs nanowire system provides no easy means to reconnect both arms of the splitter and ferromagnetic contacts are hard to control [121] and do not have the polarisation needed [15]. The best scheme for entanglement detection has yet to be found. Nevertheless, the SOI interaction and the g factor

could play an important role for entanglement detection.

In view of this, we characterize in chapter 6 the g -factor of single in InAs nanowire quantum dots states by mapping g -factor anisotropy. A random orientation of the anisotropy is found with a wide span of g values between 5 and 15. The anisotropy is attributed to a varying orbital contribution to the spin-orbit interaction due to mesoscopic fluctuations what implies a tunability of the anisotropy that could be confirmed by others [87, 146]. This paves a possible way to detect entanglement of continuous stream of electrons without ferromagnetic contacts but with two different spin-orbit fields in the two QDs of Cooper pair splitter [168, 12, 81].

In a wider prospect, the control of the coupling between a common or topological superconductor is also important for the detection of Majorana fermions [169, 23], for splitting of a Cooper pair from Majorana Bound states [170, 171] or for the coupling of spin qubits via a superconductor[115]. When the superconductor is strongly coupled Andreev Bound states (ABS) arise that can be probed non-locally [158]. The non-local correlation could also induce a new state. Consider a double quantum dot (DQD) with a normal tunnel coupling in-between the dots that couples the (1,0) and (0,1) charge state of the DQD. A molecular state will form as consequence of this hybridization. If the individual dots are coupled by CAR the charge states (1,1) to (0,0) hybridize leading to a new kind of molecular state that has been nicknamed *Andreev molecule* [112]. Our CPS devices are currently still being investigated for such non-local molecular states and theoretical models are worked by our collaborator F. Dominguez and A. Levy Yeyati from UAM, Madrid.

Altogether, the presented devices provide a playground for the investigation of non-local correlations.

Bibliography

- [1] T. Folger, *Science* **324**, 1512 (2009)
- [2] A. Einstein, B. Podolsky and N. Rosen, *Phys. Rev.* **47**, 777 (1935)
- [3] N. D. Mermin, *Physics today* **38**, 38 (1985)
- [4] J. S. Bell, *Physics* **1**, 195 (1964)
- [5] M. A. Rowe, D. Kielpinski, V. Meyer, C. A. Sackett, W. M. Itano, C. Monroe and D. J. Wineland, *Nature* **409**, 791 (2001)
- [6] M. Ansmann, H. Wang, R. C. Bialczak, M. Hofheinz, E. Lucero, M. Neeley, A. D. O’Connell, D. Sank, M. Weides, J. Wenner, A. N. Cleland and J. M. Martinis, *Nature* **461**, 504 (2009)
- [7] A. K. Ekert, *Phys. Rev. Lett.* **67**, 661 (1991)
- [8] C. H. Bennett, G. Brassard, C. Crépeau, R. Jozsa, A. Peres and W. K. Wootters, *Phys. Rev. Lett.* **70**, 1895 (1993)
- [9] M. Nielsen and I. Chuang, *Quantum Computation and Quantum Information*. Cambridge University Press, 10th ed. (2010)
- [10] D. Loss and D. P. DiVincenzo, *Phys. Rev. A* **57**, 120 (1998)
- [11] G. Deutscher and D. Feinberg, *Applied Physics Letters* **76**, 487 (2000)
- [12] Z. Scherübl, A. Pályi and S. Csonka, *Phys. Rev. B* **89**, 205439 (2014)
- [13] S. Kawabata, *J. Phys. Soc. Jpn.* **70**, 1210 (2001)
- [14] O. Malkoc, C. Bergenfeldt and P. Samuelsson, *EPL (Europhysics Letters)* **105**, 47013 (2014)
- [15] W. Kłobus, A. Grudka, A. Baumgartner, D. Tomaszewski, C. Schönenberger and J. Martinek, *Phys. Rev. B* **89**, 125404 (2014)
- [16] L. Hofstetter, S. Csonka, J. Nygard and C. Schonenberger, *Nature* **461**, 960 (2009)
- [17] L. G. Herrmann, F. Portier, P. Roche, A. L. Yeyati, T. Kontos and C. Strunk, *Phys. Rev. Lett.* **104**, 026801 (2010)

- [18] A. Das, Y. Ronen, M. Heiblum, D. Mahalu, A. V. Kretinin and H. Shtrikman, *Nat Commun* **3**, 1165 (2012)
- [19] J. Schindele, A. Baumgartner and C. Schönenberger, *Phys. Rev. Lett.* **109**, 157002 (2012)
- [20] F. H. L. Koppens, C. Buizert, K. J. Tielrooij, I. T. Vink, K. C. Nowack, T. Meunier, L. P. Kouwenhoven and L. M. K. Vandersypen, *Nature* **442**, 766 (2006)
- [21] Y. Hu, H. O. H. Churchill, D. J. Reilly, J. Xiang, C. M. Lieber and C. M. Marcus, *Nat Nano* **2**, 622 (2007)
- [22] J. Waissman, M. Honig, S. Pecker, A. Benyamini, A. Hamo and S. Ilani, *Nat Nano* **8**, 569 (2013)
- [23] V. Mourik, K. Zuo, S. M. Frolov, S. R. Plissard, E. P. A. M. Bakkers and L. P. Kouwenhoven, *Science* **336**, 1003 (2012)
- [24] C. M. Lieber and Z. L. Wang, *Mrs Bulletin* **32**, 99 (2007)
- [25] J. K. Hyun, S. Zhang and L. J. Lauhon, *Annu. Rev. Mater. Res.* **43**, 451 (2013)
- [26] X.-J. Huang and Y.-K. Choi, *Sensors and Actuators B: Chemical* **122**, 659 (2007)
- [27] E. C. Garnett, M. L. Brongersma, Y. Cui and M. D. McGehee, *Annu. Rev. Mater. Res.* **41**, 269 (2011)
- [28] F. Qian, Y. Li, S. Gradečák, D. Wang, C. J. Barrelet and C. M. Lieber, *Nano Letters* **4**, 1975 (2004)
- [29] C. Yang, C. J. Barrelet, F. Capasso and C. M. Lieber, *Nano Letters* **6**, 2929, PMID: 17163733 (2006)
- [30] J. C. Johnson, H.-J. Choi, K. P. Knutsen, R. D. Schaller, P. Yang and R. J. Saykally, *Nat Mater* **1**, 106 (2002)
- [31] S. Dayeh, D. P. Aplin, X. Zhou, P. K. Yu, E. Yu and D. Wang, *Small* **3**, 326 (2007)
- [32] C. Rehnstedt, T. Martensson, C. Thelander, L. Samuelson and L. E. Wernersson, *Electron Devices, IEEE Transactions on* **55**, 3037 (2008)
- [33] R. S. Wagner and W. C. Ellis, *Applied Physics Letters* **4**, 89 (1964)
- [34] X. Duan and C. M. Lieber, *Advanced Materials* **12**, 298 (2000)
- [35] M. Aagesen, *MBE grown nanorods and nanoplates*. Ph.D. thesis, University of Copenhagen (2007)

-
- [36] M. H. Madsen, *Indium Arsenide Nanowires - Fabrication, Characterization, and Biological Applications*. Ph.D. thesis, University of Copenhagen (2012)
- [37] M. J. L. Sourribes, I. Isakov, M. Panfilova and P. A. Warburton, *Nanotechnology* **24**, 045703 (2013)
- [38] P. Caroff, A. Dick, J. Johansson, E. Messing, K. Deppert and L. Samuelson, *Nature Nanotechnology* **4**, 50 (2009)
- [39] M. T. Björk, B. J. Ohlsson, T. Sass, A. I. Persson, C. Thelander, M. H. Magnusson, K. Deppert, L. R. Wallenberg and L. Samuelson, *Nano Letters* **2**, 87 (2002)
- [40] M. J. L. Sourribes, I. Isakov, M. Panfilova, H. Liu and P. A. Warburton, *Nano Letters* **14**, 1643 (2014)
- [41] C. Thelander, P. Caroff, S. Plissard, A. W. Dey and K. A. Dick, *Nano Letters* **11**, 2424 (2011)
- [42] J. Johansson, K. A. Dick, P. Caroff, M. E. Messing, J. Bolinsson, K. Deppert and L. Samuelson, *The Journal of Physical Chemistry C* **114**, 3837 (2010)
- [43] D. Forbes, S. Hubbard, R. Raffaele and J. S. McNatt, *Journal of Crystal Growth* **312**, 1391 (2010)
- [44] Y. Jing, X. Bao, W. Wei, C. Li, K. Sun, D. P. R. Aplin, Y. Ding, Z.-L. Wang, Y. Bando and D. Wang, *The Journal of Physical Chemistry C* **118**, 1696 (2014)
- [45] J. W. W. van Tilburg, R. E. Algra, W. G. G. Immink, M. Verheijen, E. P. A. M. Bakkers and L. P. Kouwenhoven, *Semiconductor Science and Technology* **25**, 024011 (2010)
- [46] P. K. Mohseni, A. Behnam, J. D. Wood, C. D. English, J. W. Lyding, E. Pop and X. Li, *Nano Letters* **13**, 1153 (2013)
- [47] T. Ihn, *Semiconductor Nanostructures: Quantum States and Electronic Transport*. Oxford University Press (2009)
- [48] C. Thelander, M. Björk, M. Larsson, A. Hansen, L. Wallenberg and L. Samuelson, *Solid State Communications* **131**, 573 (2004)
- [49] A. C. Ford, S. B. Kumar, R. Kapadia, J. Guo and A. Javey, *Nano Letters* **12**, 1340 (2012)
- [50] F. Vigneau, V. Prudkovkiy, I. Duchemin, W. Escoffier, P. Caroff, Y.-M. Niquet, R. Leturcq, M. Goiran and B. Raquet, *Phys. Rev. Lett.* **112**, 076801 (2014)
- [51] Q. Hang, F. Wang, P. D. Carpenter, D. Zemlyanov, D. Zakharov, E. A. Stach, W. E. Buhro and D. B. Janes, *Nano Letters* **8**, 49, PMID: 18052229 (2008)

- [52] G. R. Bell, C. F. McConville and T. S. Jones, *Phys. Rev. B* **54**, 2654 (1996)
- [53] M. J. Lowe, T. D. Veal, C. F. McConville, G. R. Bell, S. Tsukamoto and N. Koguchi, *Journal of Crystal Growth* **237-239**, 196 (2002)
- [54] S. Estévez Hernández, M. Akabori, K. Sladek, C. Volk, S. Alagha, H. Hardtdegen, M. G. Pala, N. Demarina, D. Grützmacher and T. Schäpers, *Phys. Rev. B* **82**, 235303 (2010)
- [55] L. Canali, J. Wildöer, O. Kerkhof and L. Kouwenhoven, *Applied Physics A* **66**, S113 (1998)
- [56] H. B. Michaelson, *Journal of Applied Physics* **48**, 4729 (1977)
- [57] G. W. Gobeli and F. G. Allen, *Phys. Rev.* **137**, A245 (1965)
- [58] S. Bhargava, H.-R. Blank, V. Narayanamurti and H. Kroemer, *Applied Physics Letters* **70**, 759 (1997)
- [59] N. W. Ashcroft and N. D. Mermin, *Solid State Physics*. Thomson Learning, Inc. (1976)
- [60] Z. M. Fang, K. Y. Ma, D. H. Jaw, R. M. Cohen and G. B. Stringfellow, *Journal of Applied Physics* **67**, 7034 (1990)
- [61] G. Koblmüller, K. Vizbaras, S. Hertenberger, S. Bolte, D. Rudolph, J. Becker, M. Döblinger, M.-C. Amann, J. J. Finley and G. Abstreiter, *Applied Physics Letters* **101**, 053103 (2012)
- [62] M. Möller, M. M. de Lima Jr, A. Cantarero, T. Chiaramonte, M. A. Cotta and F. Iikawa, *Nanotechnology* **23**, 375704 (2012)
- [63] Z. Zanolli, F. Fuchs, J. Furthmüller, U. von Barth and F. Bechstedt, *Phys. Rev. B* **75**, 245121 (2007)
- [64] A. De and C. E. Pryor, *Phys. Rev. B* **81**, 155210 (2010)
- [65] L. C. O. Dacal and A. Cantarero, *Materials Research Express* **1**, 015702 (2014)
- [66] T. S. Jespersen, M. L. Polianski, C. B. Sorensen, K. Flensberg and J. Nygard, *New Journal of Physics* **11**, 113025 (2009)
- [67] C. Thelander, T. Mårtensson, M. T. Börk, B. J. Ohlsson, M. W. Larsson, L. R. Wallenberg and L. Samuelson, *Applied Physics Letters* **83**, 2052 (2003)
- [68] C. Blömers, T. Grap, M. I. Lepsa, J. Moers, S. Trellenkamp, D. Grützmacher, H. Lüth and T. Schäpers, *Applied Physics Letters* **101**, 152106 (2012)
- [69] K. Storm, F. Halvardsson, M. Hurlin, D. Lindgren, A. Gustafsson, P. M. Wu, B. Monemar and L. Samuelson, *Nat Nano* **7**, 718 (2012)

-
- [70] New semiconductor materials. characteristics and properties - indium arsenide. <http://www.ioffe.rssi.ru/SVA/NSM/Semicond/InAs/index.html>, accessed: 15.05.2014 (1998)
- [71] A. C. Ford, J. C. Ho, Y.-L. Chueh, Y.-C. Tseng, Z. Fan, J. Guo, J. Bokor and A. Javey, *Nano Letters* **9**, 360 (2009)
- [72] M. Scheffler, S. Nadj-Perge, L. P. Kouwenhoven, M. T. Borgstrom and E. P. Bakkers, *J. Appl. Phys.* **106**, 124303 (2009)
- [73] F. Wang, S. Yip, N. Han, K. Fok, H. Lin, J. J. Hou, G. Dong, T. Hung, K. S. Chan and J. C. Ho, *Nanotechnology* **24**, 375202 (2013)
- [74] X. Jiang, Q. Xiong, S. Nam, F. Qian, Y. Li and C. M. Lieber, *Nano Letters* **7**, 3214 (2007)
- [75] A. E. Hansen, M. T. Björk, C. Fasth, C. Thelander and L. Samuelson, *Phys. Rev. B* **71**, 205328 (2005)
- [76] C. Blömers, M. I. Lepsa, M. Luysberg, D. Grützmacher, H. Lüth and T. Schäpers, *Nano Lett.* **11**, 3550 (2011)
- [77] S. Dhara, H. S. Solanki, V. Singh, A. Narayanan, P. Chaudhari, M. Gokhale, A. Bhattacharya and M. M. Deshmukh, *Phys. Rev. B* **79**, 121311 (2009)
- [78] A. Pfund, I. Shorubalko, K. Ensslin and R. Leturcq, *Physical Review Letters* **99** (2007)
- [79] C. Fasth, A. Fuhrer, L. Samuelson, V. N. Golovach and D. Loss, *Phys. Rev. Lett.* **98**, 266801 (2007)
- [80] T. D. Stanescu and S. Tewari, *Journal of Physics: Condensed Matter* **25**, 233201 (2013)
- [81] B. Braunecker, P. Burset and A. Levy Yeyati, *Phys. Rev. Lett.* **111**, 136806 (2013)
- [82] L. P. Kouwenhoven, C. M. Marcus, P. L. McEuen, S. Tarucha, R. M. Westervelt and N. S. Wingreen, *Mesoscopic Electron Transport* **345**, 105, sohn, LL Kouwenhoven, LP Schon, G NATO Advanced Study Institute on Mesoscopic Electron Transport JUN 25-JUL 05, 1996 CURACAO, NETH ANTILLES (1997)
- [83] R. Hanson, L. P. Kouwenhoven, J. R. Petta, S. Tarucha and L. M. K. Vandersypen, *Rev. Mod. Phys.* **79**, 1217 (2007)
- [84] C. W. J. Beenakker, *Phys. Rev. B* **44**, 1646 (1991)
- [85] P. Zeeman, *Nature* **55**, 347 (1897)

- [86] S. Csonka, L. Hofstetter, F. Freitag, S. Oberholzer, C. Schonenberger, T. S. Jespersen, M. Aagesen and J. Nygård, *Nano Letters* **8**, 3932 (2008)
- [87] M. D. Schroer, K. D. Petersson, M. Jung and J. R. Petta, *Phys. Rev. Lett.* **107**, 176811 (2011)
- [88] C. E. Pryor and M. E. Flatté, *Phys. Rev. Lett.* **96**, 026804 (2006)
- [89] A. De and C. E. Pryor, *Phys. Rev. B* **76**, 155321 (2007)
- [90] S. Cronenwett, *Coherence, Charging, and Spin Effects in Quantum Dots and Point Contacts*. Ph.D. thesis, Stanford University (2001)
- [91] A. C. Hewson and J. Kondo, *Scholarpedia* **4**, 7529, revision #91408 (2009)
- [92] J. Kondo, *Progress of Theoretical Physics* **32**, 37 (1964)
- [93] H. Bruus and K. Flensberg, *Many-Body Quantum Theory in Condensed Matter Physics*. Oxford University Press (2004)
- [94] L. Kouwenhoven and L. Glazman, *Physics world* **14**, 33 (2001)
- [95] L. Glazman and M. Raikh, *JETP Letters* **47**, 452 (1988)
- [96] D. Goldhaber-Gordon, H. Shtrikman, D. Mahalu, D. Abusch-Magder, U. Meirav and M. A. Kastner, *Nature* **391**, 156 (1998)
- [97] S. M. Cronenwett, T. H. Oosterkamp and L. P. Kouwenhoven, *Science* **281**, 540 (1998)
- [98] Y. Meir, N. S. Wingreen and P. A. Lee, *Phys. Rev. Lett.* **70**, 2601 (1993)
- [99] M. Tinkham, *Introduction to Superconductivity*. Dover, 2nd edition ed. (2004)
- [100] H. Ibach and H. Lüth, *Festkörperphysik*. Springer, siebte auflage ed. (2008)
- [101] H. K. Onnes, *Commun. Phys. Lab. Univ. Leiden* **12**, 120 (1911)
- [102] W. Meissner and R. Ochsenfeld, *Naturwissenschaften* **21**, 787 (1933)
- [103] L. N. Cooper, *Phys. Rev.* **104**, 1189 (1956)
- [104] C. W. J. Beenakker, *Pre-print* ArXiv:cond-mat/990293 (1999)
- [105] A. F. Andreev, *Sov. Phys. JETP* **19**, 1228 (1964)
- [106] G. E. Blonder, M. Tinkham and T. M. Klapwijk, *Phys. Rev. B* **25**, 4515 (1982)
- [107] T. Klapwijk, *Journal of Superconductivity* **17**, 593 (2004)
- [108] S. Russo, M. Kroug, T. M. Klapwijk and A. F. Morpurgo, *Phys. Rev. Lett.* **95**, 027002 (2005)

-
- [109] D. Beckmann and H. v. Löhneysen, *Applied Physics A* **89**, 603 (2007)
- [110] G. Falci, D. Feinberg and F. W. J. Hekking, *EPL (Europhysics Letters)* **54**, 255 (2001)
- [111] P. Recher, E. V. Sukhorukov and D. Loss, *Phys. Rev. B* **63**, 165314 (2001)
- [112] J. Schindele, *Observation of Cooper Pair Splitting and Andreev Bound States in Carbon Nanotubes*. Ph.D. thesis, University of Basel (2014)
- [113] L. Hofstetter, S. Csonka, A. Baumgartner, G. Fülöp, S. d'Hollosy, J. Nygård and C. Schönenberger, *Phys. Rev. Lett.* **107**, 136801 (2011)
- [114] D. Feinberg, *Eur. Phys. J. B* **36**, 419 (2003)
- [115] M. Leijnse and K. Flensberg, *Phys. Rev. Lett.* **111**, 060501 (2013)
- [116] P. Recher, D. Saraga and D. Loss, Creation and detection of mobile and non-local spin-entangled electrons (2004)
- [117] J. Kjelstrup-Hansen, S. Dohn, D. N. Madsen, K. MÅlhav and P. BÅggild, *Journal of Nanoscience and Nanotechnology* **6**, 1995 (2006-07-01T00:00:00)
- [118] T. K. S. Wong and S. G. Ingram, *Journal of Vacuum Science & Technology B* **10**, 2393 (1992)
- [119] B. E. E. Kastenmeier, P. J. Matsuo and G. S. Oehrlein, *Journal of Vacuum Science & Technology A* **17**, 3179 (1999)
- [120] L. Hofstetter, *Hybrid Quantum Dots in InAs Nanowires*. Ph.D. thesis, University of Basel (2011)
- [121] J. Sann, J. Gramich, A. Baumgartner, M. Weiss and C. Schönenberger, *Journal of Applied Physics* **115**, 174309 (2014)
- [122] C. Fasth, A. Fuhrer, M. T. Björk and L. Samuelson, *Nano Letters* **5**, 1487 (2005)
- [123] K. Flohr, M. Liebmann, K. Sladek, H. Y. Gunel, R. Frielinghaus, F. Haas, C. Meyer, H. Hardtdegen, T. Schapers, D. Grutzmacher and M. Morgenstern, *Review of Scientific Instruments* **82**, 113705 (2011)
- [124] C. Enss and S. Hunklinger, *Low-Temperature Physics*. Springer (2005)
- [125] H. Bluhm and K. A. Moler, *Review of Scientific Instruments* **79**, 014703 (2008)
- [126] S. De Franceschi, J. A. van Dam, E. P. A. M. Bakkers, L. F. Feiner, L. Gurevich and L. P. Kouwenhoven, *Applied Physics Letters* **83**, 344 (2003)
- [127] Z. Zhong, Y. Fang, W. Lu and C. M. Lieber, *Nano Letters* **5**, 1143 (2005)

- [128] T. S. Jespersen, M. Aagesen, C. Sørensen, P. E. Lindelof and J. Nygård, *Phys. Rev. B* **74**, 233304 (2006)
- [129] Y. J. Doh, J. A. van Dam, A. L. Roest, E. Bakkers, L. P. Kouwenhoven and S. De Franceschi, *Science* **309**, 272 (2005)
- [130] L. Hofstetter, A. Geresdi, M. Aagesen, J. Nygård, C. Schönenberger and S. Csonka, *Phys. Rev. Lett.* **104**, 246804 (2010)
- [131] S. Gustavsson, I. Shorubalko, R. Leturcq, T. Ihn, K. Ensslin and S. Schön, *Phys. Rev. B* **78**, 035324 (2008)
- [132] S. Gustavsson, I. Shorubalko, R. Leturcq, S. Schon and K. Ensslin, *Appl. Phys. Lett.* **92**, 152101 (2008)
- [133] D. B. Suyatin, C. Thelander, M. T. Bjork, I. Maximov and L. Samuelson, *Nanotechnology* **18**, 5, 9361874 UK IOP Publishing 19 (2007)
- [134] G. Fülöp, *Cooper-pár feltörő nanoáramkör továbbfejlesztése*. Master's thesis, Budapest University of Technology and Economics (2011)
- [135] J. J. Kelly, X. Xia, C. M. A. Ashruf and P. French, *Sensors Journal, IEEE* **1**, 127 (2001)
- [136] R. A. Jalabert, A. D. Stone and Y. Alhassid, *Phys. Rev. Lett.* **68**, 3468 (1992)
- [137] E. E. Narimanov, N. R. Cerruti, H. U. Baranger and S. Tomsovic, *Phys. Rev. Lett.* **83**, 2640 (1999)
- [138] A. M. Chang, H. U. Baranger, L. N. Pfeiffer, K. W. West and T. Y. Chang, *Phys. Rev. Lett.* **76**, 1695 (1996)
- [139] A. Pfund, I. Shorubalko, R. Leturcq and K. Ensslin, *Applied Physics Letters* **89**, 252106 (2006)
- [140] P. Dahl Nissen, T. Sand Jespersen, K. Grove-Rasmussen, A. Márton, S. Upadhyay, M. Hannibal Madsen, S. Csonka and J. Nygård, *Journal of Applied Physics* **112**, 084323 (2012)
- [141] S. d'Hollosy, *Barrier-transparency tuning of superconducting contacts on InAs nanowires*. Master's thesis, University of Basel (2010)
- [142] S. Nadj-Perge, S. M. Frolov, E. P. A. M. Bakkers and L. P. Kouwenhoven, *Nature* **468**, 1084 (2010)
- [143] M. T. Björk, A. Fuhrer, A. E. Hansen, M. W. Larsson, L. E. Fröberg and L. Samuelson, *Phys. Rev. B* **72**, 201307 (2005)
- [144] L. P. Kouwenhoven, D. G. Austing and S. Tarucha, *Reports on Progress in Physics* **64**, 701 (2001)

-
- [145] R. S. Deacon, Y. Kanai, S. Takahashi, A. Oiwa, K. Yoshida, K. Shibata, K. Hirakawa, Y. Tokura and S. Tarucha, *Phys. Rev. B* **84**, 041302 (2011)
- [146] S. Takahashi, R. S. Deacon, A. Oiwa, K. Shibata, K. Hirakawa and S. Tarucha, *Phys. Rev. B* **87**, 161302 (2013)
- [147] B. J. Witek, R. W. Heeres, U. Perinetti, E. P. A. M. Bakkers, L. P. Kouwenhoven and V. Zwiller, *Phys. Rev. B* **84**, 195305 (2011)
- [148] S. d'Hollosy, G. Fàbiàn, A. Baumgartner, J. Nygård and C. Schönenberger, *AIP Conference Proceedings* **1566**, 359 (2013)
- [149] G. A. Intronati, P. I. Tamborenea, D. Weinmann and R. A. Jalabert, *Phys. Rev. B* **88**, 045303 (2013)
- [150] R. Zielke, F. Maier and D. Loss, *Phys. Rev. B* **89**, 115438 (2014)
- [151] T. Sand-Jespersen, J. Paaske, B. M. Andersen, K. Grove-Rasmussen, H. I. Jørgensen, M. Aagesen, C. B. Sørensen, P. E. Lindelof, K. Flensberg and J. Nygård, *Phys. Rev. Lett.* **99**, 126603 (2007)
- [152] A. Eichler, M. Weiss, S. Oberholzer, C. Schönenberger, A. Levy Yeyati, J. C. Cuevas and A. Martín-Rodero, *Phys. Rev. Lett.* **99**, 126602 (2007)
- [153] S. Takahashi, R. S. Deacon, K. Yoshida, A. Oiwa, K. Shibata, K. Hirakawa, Y. Tokura and S. Tarucha, *Phys. Rev. Lett.* **104**, 246801 (2010)
- [154] J. R. Petta and D. C. Ralph, *Phys. Rev. Lett.* **89**, 156802 (2002)
- [155] J. E. Moore and X.-G. Wen, *Phys. Rev. Lett.* **85**, 1722 (2000)
- [156] A. Kogan, S. Amasha, D. Goldhaber-Gordon, G. Granger, M. A. Kastner and H. Shtrikman, *Phys. Rev. Lett.* **93**, 166602 (2004)
- [157] J.-D. Pillet, C. H. L. Quay, P. Morfin, C. Bena, A. L. Yeyati and P. Joyez, *Nat Phys* **6**, 965 (2010)
- [158] J. Schindele, A. Baumgartner, R. Maurand, M. Weiss and C. Schönenberger, *Phys. Rev. B* **89**, 045422 (2014)
- [159] V. Novotny and P. Meincke, *J. Low Temp. Phys.* **18**, 147 (1975)
- [160] T. D. Stanescu and S. Das Sarma, *Phys. Rev. B* **87**, 180504 (2013)
- [161] A. L. Yeyati, F. S. Bergeret, A. Martin-Rodero and T. M. Klapwijk, *Nat Phys* **3**, 455 (2007)
- [162] A. Kleine, A. Baumgartner, J. Trbovic and C. Schönenberger, *EPL (Europhysics Letters)* **87**, 27011 (2009)

- [163] P. Burset, W. J. Herrera and A. L. Yeyati, *Phys. Rev. B* **84**, 115448 (2011)
- [164] G. Fülöp, S. d'Hollosy, B. A., P. Makk, V. Guzenko, H. Madsen, J. Nygard, C. Schönenberger and S. Csonka *in preparation*
- [165] N. L. B. Ziino, P. Krogstrup, M. H. Madsen, E. Johnson, J. B. Wagner, C. M. Marcus, J. Nygård and J. T. S., *Pre-print* ArXiv:1309.4569 [cond-mat.mtrl-sci]
- [166] W. Knoben, S. H. Brongersma and M. Crego-Calama, *The Journal of Physical Chemistry C* **113**, 18331 (2009)
- [167] M. H. Sun, H. J. Joyce, Q. Gao, H. H. Tan, C. Jagadish and C. Z. Ning, *Nano Letters* **12**, 3378 (2012)
- [168] G. Burkard, *Journal of Physics: Condensed Matter* **19**, 233202 (2007)
- [169] M. Wimmer, A. R. Akhmerov, J. P. Dahlhaus and C. W. J. Beenakker, *New Journal of Physics* **13**, 053016 (2011)
- [170] J. Nilsson, A. R. Akhmerov and C. W. J. Beenakker, *Phys. Rev. Lett.* **101**, 120403 (2008)
- [171] B. Zocher and B. Rosenow, *Phys. Rev. Lett.* **111**, 036802 (2013)

A. Fabrication recipes

A.1. Wafer characteristics

- *Substrate material* Si
- *Dopant* p, boron
- *Resistivity* 0.003 - 0.005 Ωm
- *Capping layer* 400 nm silicon oxide

A.2. Wafer cleaning

1. Sonicate in acetone for 10 min, rinse and blow dry
2. Sonicate in deionized water for 10 min, rinse and blow dry
3. Sonicate in IPA, rinse and blow dry
4. UV/ozone treatment for 30 min (Model 42-220, Jelight Company, USA)

If dirt persisted we used more harsh methods which are highly oxidizing and included an O_2 plasma exposure for 1 min (recipe see below) or immersing the wafer for 5 min in mild Piranha (3 ml H_2O 5 ml H_2SO_4 2.5 M, 2 ml H_2O_2 30%), rinsing it with deionized water and blowing dry. Even then some particles sometimes remained which are likely to be Si debris from the wafer cutting. Therefore care should be taken when the wafers are scratched and cut that the little debris is generated or it is taken up in liquid. The aqueous sonication steps tends to remove them, though.

A.3. EBL process for PMMA

- *Resist* PMMA 950K dissolved in Chlorobenzene
- *Spin coating* 4000 rpm yielding a thickness of 350 nm
- *Hardening* 5 min on the hotplate at 180°C
- *Exposure parameters* 220 $\mu\text{C}/\text{cm}^2$ at 20 kV and 17 mm wd
- *Developer* 3:1 Isopropyl alcohol (IPA) / Methylisobutyl ketone (MIBK) for 80 s
- *Lift-off* warm acetone

A.4. EBL process for bottom gates

- *Resist* ZEP 520K (ZEON chemicals) dissolved
- *Spin coating* 4000 rpm yielding a thickness of 60 nm
- *Hardening* 5 min on the hotplate at 180°C

- *Exposure parameters* check $\mu\text{C}/\text{cm}^2$
- *Developer* pure Pentylacetate for 60 s rinse with Isopropyl alcohol (IPA)
- *Lift-off* warm N-methylpyrrolidone (NMP) rinse with acetone and IPA

A.5. O₂ plasma cleaning

- *Base pressure* 5×10^{-5} mbar
- *O₂ flow* 16%
- *Process pressure* 250 mTorr
- *RF Power* 30 W
- *Exposure time* 20 - 40 s for resist removal up to 2 min for general cleaning

A.6. Reactive ion etching (RIE) of SiN_x

- *Base pressure* 5×10^{-5} mbar
- *O₂ flow* 4%
- *CHF₃ flow* 50%
- *Process pressure* 50 mTorr
- *RF Power* 50 W
- *Exposure time* 105 s (etches 25 - 30 nm)

A.7. Argon ion beam milling

The Ar ion could be done in different evaporation systems in-situ

For the Balzers system:

- *Base pressure* 2×10^{-6} mbar
- *Ar flow* 3.2 sccm
- *Process background pressure* 1×10^{-4} mbar
- *Ar Plasma* Recipe 2
- *Ar Beam Current* 20 mA
- *Ar Beam Voltage* 500 V
- *Exposure time* 10 - 20 s

For the Bestec system:

- *Base pressure* 7×10^{-6} mbar
- *Ar flow* Needle valve adjusted to give steady process pressure
- *Process pressure* 5×10^{-5} mbar
- *Plasma Power (Magnetron)* Adjust voltage that output current is at 20 mA
- *Extraction voltage* 0.6 kV
- *Anode Voltage* 1 kV
- *Exposure time* 60 s

B. Electrostatic discharges

Electrostatic discharges (ESD) are one of the main causes for the low fabrication yield and the nanowire devices seemed to be very sensitive to them. ESDs can happen at various points during fabrication and measurement. We mainly speculate about three main types and there consequences.

Classical In the scanning electron micrograph in fig. B.1a the nanowire is probably melted by an ESD driving a significant current through the device what is inferred from two rounded off ends between to the contacts. Most of these classical blows occur during bonding or building in the cryostat. The yield improved when we started to used ESD safe sample boxes and a high resistive grounding scheme at the wire bonder. Some nanowires show only some corrugation and larger grooves. The cause for that are unclear and can be manyfold however we generally favour electrical reasons occurring after fabrication, too.

Gate leak Fig. B.1b shows a specific example of a nanowire blown inside a cryostat during leak testing the bottom gates. We realized too late that actually the gate just below the residual blob was leaking and a larger current could flow.

Plasma induced More recently issues happened for sure during Ar sputtering done for oxide removal. Images of the failed devices can be found in figs. B.1c and B.1d. Because the Ar treatment is in-situ with the metal evaporation, the destroyed areas (arbitrary shaped areas most whitish in all images) are covered with additional material. Nevertheless residual blobs can be seen indicating that a electric discharge melt resist and metal leads. Strikingly, these errors appear always in proximity to the nanowire and extend towards the prefabricated bottom gate contact if there. Also, they happen in both our evaporation machines (Balzers & Bestec), what supports the thesis that this is not a random effect caused by malfunction of the equipment but inherent to the nanowire or the wafer.

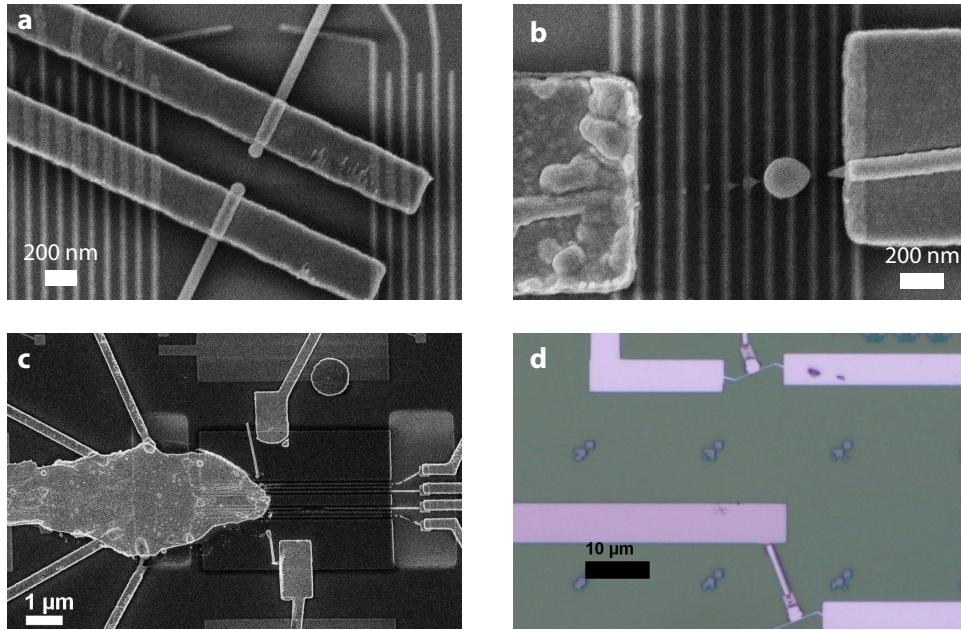


Figure B.1.: Different images (a-c: SEM, d: optical microscope) of nanowires destroyed by electrostatic discharges (ESD). **a** | Typical device burned through by an ESD during handling or bonding. **b** | A leaking bottom gate caused a large current and melted the nanowire. A residual blob stayed above leaking gate. **c** | Destroyed device during Ar sputtering. Additional metal is evaporated after the discharge and lift-off performed. **d** | Same fabrication error as in (c) but on devices without bottom gates.

C. Appendix to chapter 7

C.1. Gate voltages to form the QDs

Table C.1 lists the voltages applied on the local gates to form the experiments presented in Figs. 1-4. The voltages defining the barriers of QD1 are given in blue, the ones defining the barriers of QD2 in red. Gates below S are colored in green. The backgate was set to zero potential in all experiments. The QDs in the last experiments were defined by only two gates near S, while the gates near N1 and N2 were set to large positive voltages to increase the coupling to the normal contacts. Gate voltages varied during the experiments are labeled '(t)'

V_{gi} (V)	Fig. 7.1 and 7.2	Fig. 7.3	Fig. 7.4
V_{g1}	-3.5	-3.475	+4
V_{g2}	-0.8 (t)	-1.47 (t)	0
V_{g3}	-6.5	-6.5	0
V_{g4}	0	0	-4.13
V_{g5}	0	0	-4.3
V_{g6}	0	0	(t)
V_{g7}	0	0	(t)
V_{g8}	-4.5	-4.5	-4.33 (t)
V_{g9}	-0.38 (t)	-0.9 (t)	-4.53
V_{g10}	-4.7	-4.7	+4

Table C.1.: Gate configurations in the different experiments.

D. Additional data to chapter 8

D.1. Gate characterization and doping effects

The effects of different interface properties can be observed in our investigated devices. Figure D.1 shows the differential conductance as function of gate voltage in the linear regime at 4 K for different gates fg1-fg9 below a single nanowire. Above the gates fg1, fg5 and fg9 a metallic electrode was put in electrical contact with the InAs nanowire. The width of the gates and the electrode placement can be seen in the central inset which shows a SEM image of the device. 2-terminal resistance between one outer and the central electrode exhibit different threshold voltages, decreasing towards the central lead which consist of a Ti/Al bilayer compared with the outer electrodes being a Ti/Pd bilayer. We suspect that the Ti adhesion layer¹ is incomplete allowing the top metal to get into contact with the nanowire. This could give rise to a inhomogeneous doping profile in the nanowire and therefore different threshold voltages.

In fig. D.1 the conductance curves in blue being the down sweep are different from the up sweep direction in green. The observed shift is attributed to relaxing trap states either in the native oxide, at the metal-semiconductor interface or in the gate insulator. Assuming traps in the native oxide the surface scattering can be increased by the pure disorder potential.

¹For fabrication details see chapter 4

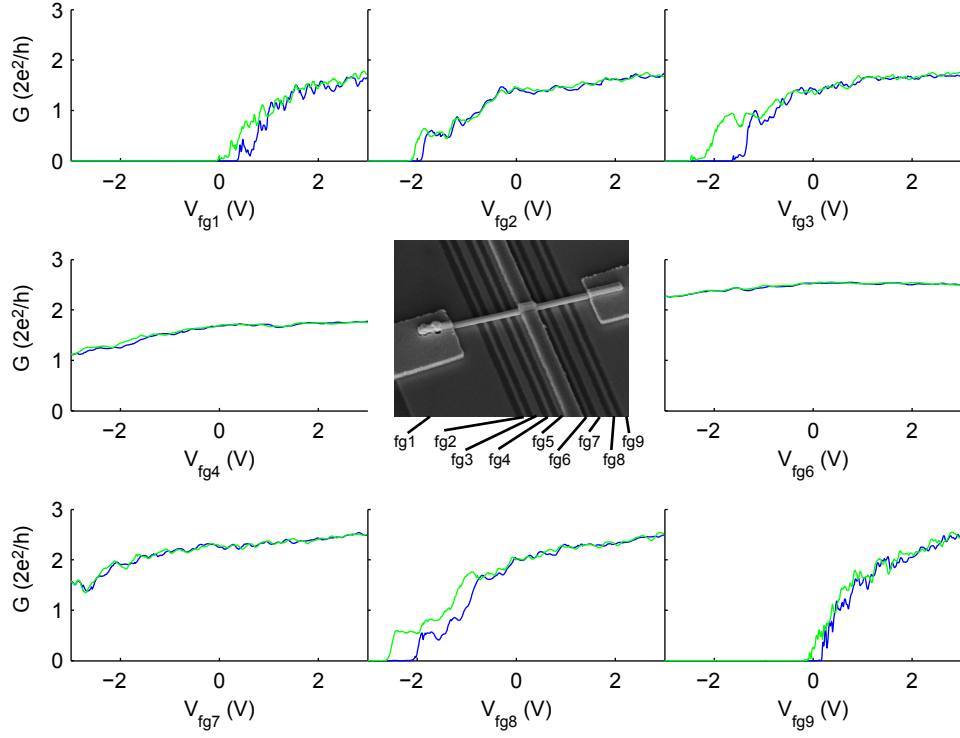


Figure D.1.: Gate voltage characteristics at a temperature of 4K for different gates fg1-fg9 below the nanowire shown in the central inset of the figure. The curves in blue and green are the down and up gate voltage sweeps showing significant hysteresis effects due trap states in the oxides. The gates threshold voltages of the central gates indicate that the central lead made from Ti/Al bilayer has surprisingly different metal contact interface properties than the outer Ti/Pd leads.

Curriculum Vitae

Samuel André d'Hollosy
October 18 1984 born in Zug ZG

Education

1999–2003	Matura, Kantonschule Limmattal (Mathematics and Physics Focus)
2004–2007	Bachelor of Science in Nanosciences at the University of Basel
2008–2010	Master of Science in Nanosciences at the University of Basel Master thesis in the group of Prof. C. Schönenberger, Basel: “Barrier-transparency tuning of superconducting contacts on InAs nanowires”
2010–2014	PhD in experimental physics at the University of Basel Disseration in the group of Prof. C. Schönenberger: “Locally Tunable InAs Nanowire Quantum Dots for Cooper Pair Splitting”

Positions

2007–2008	Internship at CSIRO Australia within the IAESTE exchange program Research work on the topics: - Quantum dot synthesis through precipitation of CdS - Fabrication of Bragg reflectors out of polymer films - Organic synthesis of bipyridines.
2010–2014	Teaching assistant for Physics

Publications

Publications

- *Giant Fluctuations and Gate Control of the g -factor in InAs Nanowire Quantum Dots*, L. Hofstetter, S. Csonka, A. Baumgartner, G. Fülöp, S. d'Hollosy, J. Nygård and C. Schönenberger
Phys. Rev. Lett. **107**, 136801 (2011)
- *g -factor anisotropy in nanowire-based InAs quantum dots*, S. d'Hollosy, G. Fàbiàn, A. Baumgartner, J. Nygård and C. Schönenberger
AIP Conference Proceedings **1566**, 359-360 (2013)
- *Local electrical tuning of the nonlocal signals in a Cooper pair splitter*, G. Fülöp, S. d'Hollosy, A. Baumgartner, P. Makk, V. Guzenko, H.M. Madsen, J. Nygård, C. Schönenberger and S. Csonka
in preparation

Talks

- *g -factors in InAs Nanowires*
Talk at the SE²ND workshop "Spin-orbit Interactions and Entanglement Generation in Solid State Devices", Copenhagen, 2 May 2012

Poster Contributions

- *Quantum transport in carbon nanotube and nanowire hybrid devices* H. Aurich, A. Baumgartner, L. Hofstetter, S. d'Hollosy, S. Nau, J. Samm, J. Schindele, C. Schönenberger, and M. Weiss
Poster at the NCCR QSIT General Meeting, Arosa, 12-14 January 2011
- *Cooper pair splitting and electron transport in superconductor hybrid nanostructures in few-layer graphene ribbons*, J. Schindele, S. d'Hollosy, S. Nau, G. Fàbiàn, J. Samm, A. Baumgartner, M. Weiss and C. Schönenberger
Poster at the NCCR QSIT General Meeting, Arosa, 1-3 February 2012
- *g -factor anisotropy in nanowire-based InAs quantum dots* S. d'Hollosy, G. Fàbiàn, A. Baumgartner, J. Nygård and C. Schönenberger.
Poster at the 31st International Conference on the Physics of Semiconductors, Zürich, 29 July to 3 August 2012

- *Electrical tunability of InAs nanowire quantum dots and Cooper pair splitting*, S. d'Hollosy, G. Fülöp, A. Baumgartner, S. Csonka, H.M. Madsen, J. Nygård and C. Schönenberger.
Poster at the Frontiers in Quantum Engineered Devices, Obergurgl, 19-24 August, 2013